

Modeling of temperature variations and response in a mining road bridge in Kiruna



**Henrik Ekman &
Mikael Fabricius**

Division of Structural Engineering
Faculty of Engineering, LTH
Lund University, 2016

Master Thesis TVBK - 5255

Avdelningen för Konstruktionsteknik

Lunds Tekniska Högskola

Box 118

221 00 LUND

Division of Structural Engineering

Faculty of Engineering, LTH

P.O. Box 118

S-221 00 LUND

Sweden

Modellering av temperaturvariationer och respons i Gruvvägsbron i Kiruna

Modeling of temperature variations and response in a mining road bridge in
Kiruna

Henrik Ekman och Mikael Fabricius

2016

Rapport TVBK-5255

ISSN 0349-4969

ISRN: LUTVDG/TVBK-16/5255 (87)

Examensarbete

Handledare: Oskar Larsson

Juni 2016

Abstract

This thesis treats a concrete bridge located in Kiruna, in the north of Sweden, which was used for the mining industry. A finite element model has been created with the finite element software Abaqus to find out if it accurately can describe the variation of the temperature and deformation within the bridge over time. The temperature variations and deformations have been studied with respect to climate effects.

The climate is complex and affects the temperature within the bridge in different ways. During daytime the bridge is exposed to radiation from the sun and the air temperature which is relatively high during the studied time period. During the night the bridge will cool down due to outgoing longwave radiation and the absence of the sun. The temperature in the bridge is also affected by convection mainly caused by wind.

The used finite element model has previously been verified for two-dimensional temperature variation in concrete structures without overhangs. In this work the temperature variation will be studied in a cross section of the bridge using a two-dimensional model including overhang and paving layer. The temperature variation was studied for June 2009, August 2010, and a short period during June 2014. The strain was studied in a three dimensional model for June 2009.

The finite element model calculates the temperature variations within a structure based on climate input data. This data consists of hourly values of air temperature, long wave radiation and global radiation. The temperature input data was received from the Swedish Meteorological and Hydrological Institute which have weather stations placed across Sweden.

The temperature variations lead to deformations. An increase in temperature will force the concrete to expand, and a decrease in temperature will force the concrete to contract. The modelled deformations within the structure are also affected by how the supports are modelled and the choice of material properties.

After calculating the temperature variations it is possible to calculate the deformations based on the temperature calculation results. The temperature- and deformation results were compared to measurements from temperature and strain gauges by M.Sc. Niklas Bagge and his co-workers from Luleå Technical University.

The results show that the 2D temperature model captures the temperature variation very well. Further the results show that the 3D strain model captures the strain variation fairly well and the 2D strain model shows unreliable results.

Keywords:

CLIMATE, TEMPERATURE, FINITE ELEMENT, DEFORMATIONS, KIRUNA, SMHI, BRIDGE, STRAINS

Sammanfattning

Den här studien har utförts på en bro i Kiruna, i norra Sverige, som användes till gruvindustrin. En modell av bron skapades med finita elementmetoden i programvaran Abaqus 6.14 för att ta reda på hurvida temperatur- och töjningsvariationerna på bron på grund av klimatets påverkan kan beskrivas.

Klimatets temperaturpåverkan på bron är komplex. Under dagtid påverkas bron av strålning från solen och luftens temperatur som är relativt hög under den tid som bron har studerats. Under natten sker en temperatursänkning i bron på grund av utgående långvågig strålning och den relativt låga lufttemperaturen. Temperaturen i bron påverkas även av konvektion som uppstår då vinden träffar bronns ytor.

Den FE-modell som använts har nyligen validerats för tvådimensionella modeller vad gäller temperaturpåverkan. I detta examensarbete har temperaturvariationer i ett tvärsnitt av bron studerats genom en tvådimensionell modell som inkluderar överhäng och asfaltsbeläggning. Temperaturvariationerna studerades för Juni 2009, Augusti 2010 och en kortare tidsperiod under Juni 2014. Töjningspåverkan av bron har undersökts i en två-dimensionell och en tre-dimensionell modell i Juni 2009.

FE-modellen beräknar temperaturvariationer inuti konstruktionen baserat på tillgänglig klimatdata, lufttemperatur, långvågig strålning och global strålning för en gång i timmen. Den klimatdata som använts har hämtats från Svenska Meteorologiska och Hydrologiska Institutet, SMHI, som är en institution med väderstationer över hela Sverige.

Temperaturens påverkan på bron leder med tiden till deformationer. Vid ökning av temperaturen tvingas betongen att expandera och en sänkning av temperaturen ger en motsatt effekt, det vill säga att betongen drar ihop sig. Deformationerna i konstruktionen påverkas även av hur stödförhållandena modelleras samt av materialegenskaperna.

Efter beräkning av temperaturvariationerna är det möjligt att beräkna deformationerna baserat på resultaten från temperaturberäkningen. Temperatur- och deformationsresultaten jämförs sedan med mätningar som utförts med hjälp av temperaturmätare och töjningsmätare av M.Sc. Niklas Bagge och hans medarbetare vid Luleås tekniska universitet.

Resultaten visar att 2D-temperaturmodellen beräknar temperaturvariationer som stämmer väldigt bra ihop med de verkliga temperaturvariationerna. Resultaten från 3D-töjningsmodellen visar att töjningsvariationerna kan fångas relativt bra medan resultaten från 2D-töjningsmodellen stämmer mindre bra överens med den verkliga variationen.

Nyckelord:

KLIMAT, TEMPERATUR, FINITA ELEMENT, DEFORMATIONER, KIRUNA, SMHI, BRO, TÖJNINGAR

Acknowledgements

This master thesis work has been performed at the division of Structural Engineering at the Faculty of Engineering at Lund University during the period of January 2016 to June 2016.

In particular, we would like to thank our supervisor Ph.D. Oskar Larsson who helped us with this study by support and supervision. We would also like to thank our examiner Professor Miklos Molnar. Further we would like to thank Niklas Bagge, who obtained the measuring data and Kent Persson who gave valuable input about Abaqus 6.14. Finally we would like to thank our opponent Dino Sehic.

Lund, June 2016

Henrik Ekman, Mikael Fabricius

Contents

1	Introduction.....	1
1.1	Background	1
1.2	Purpose	2
1.3	Methods	2
2	Theory	3
2.1	Solar radiation	3
2.2	Solar radiation instruments	7
2.3	Long-wave heat radiation	9
2.4	Convection	11
2.5	Heat transfer	12
2.6	Concrete	15
2.6.1	Material components	15
2.6.2	Specific heat capacity	16
2.6.3	Density	16
2.6.4	Conductivity	17
2.6.5	Young's Modulus	17
2.6.6	Thermal expansion coefficient	17
2.7	Asphalt	17
2.8	Coefficient of determination	18
3	Model.....	19
3.1	Limitations and Assumptions	19
3.2	Choice of material properties	21
3.3	Input data	22
3.4	Geometry	23
3.4.1	Bridge geometry for two dimensions	23
3.4.2	Bridge geometry for three dimensions	24
3.5	Measuring gauges locations	25
3.5.1	Temperature gauges	25
3.5.2	Strain gauges	26
4	Temperature simulation in two dimensions	27

4.1	Finite Element	27
4.2	Loads and interactions in Abaqus	28
4.2.1	Use of loads and interactions	28
4.2.2	Horizontal Global Radiation	28
4.2.3	Vertical Global Radiation	29
4.2.4	Convection	29
4.2.5	Long wave heat radiation	30
4.3	Mesh for calculating the temperature	31
4.4	Temperature results for 2009	32
4.4.1	Measuring point TSÖ	32
4.4.2	Measuring point TMÖ	33
4.4.3	Measuring point TNÖ	34
4.5	Temperature results for 2010	35
4.5.1	Measuring point TSÖ	35
4.5.2	Measuring point TMÖ	36
4.5.3	Measuring point TNÖ	37
4.6	Temperature results for 2014	38
4.7	Coefficient of determination	41
4.8	Temperature variation further into the structure	41
4.8.1	Results	43
5	Strain simulation in two dimensions	45
5.1	Boundary conditions for two dimensions	45
5.2	Results	45
5.2.1	Measuring point St12Sb1	45
5.2.2	Measuring point St12Nb	47
6	Strain simulation in three dimensions	51
6.1	Boundary conditions for three dimensions	52
6.2	Results	53
6.2.1	Measuring point 1 - southern girder	55
6.2.2	Measuring point 2 - southern girder	56
6.2.3	Measuring point 3 - southern girder	57
6.2.4	Measuring point 4 - southern girder	58
6.2.5	Measuring point 5 - mid girder	59

6.2.6	Measuring point 6 - mid girder	60
6.2.7	Measuring point 7 - northern girder	61
6.2.8	Measuring point 8 - northern girder	62
7	Discussion	63
8	Conclusion	65
9	References	67
10	Appendix.....	69
10.1	Temperature results for 2014	69
10.2	Temperature variation in relation to depth.....	75
10.2.1	Temperature variation for June, 2009	75
10.2.2	Temperature variation for August, 2010.....	81
10.3	Temperature distribution in 2D model	87

Notations

T	Temperature	[°C]
G	Global solar radiation	[W/m ²]
I_b	Direct radiation	[W/m ²]
I_d	Diffuse light	[W/m ²]
I_g	Reflected light	[W/m ²]
ρ	Density	[kg/m ³]
c	Specific heat capacity	[J/ (kg· °C)]
k	Thermal conductivity	[W/(m· °C)]
θ	Angle of incidence	[°C]
δ	Declination between equator plane and the suns angle	[°C]
β	Slope between surface and horizontal plane	[°C]
γ	Surface azimuth angle	[°C]
γ_s	Angle between direct solar radiation projected on the horizontal surface and south direction	[°C]
ω	Hour angle	[°C/hour]
a	Absorption coefficient	--
q_s	Absorbed energy	[W/m ²]
E_b	Emissive power given by the Stefan-Boltzmann law	[W/m ²]
σ	Stefan-Boltzmann constant	[W/(m ² · K ⁴)]
T_s	The surface temperature	[°C]
q_r	Difference between received heat radiation and emitted heat radiation.	[W/m ²]

T_{sur}	The temperature of the surroundings.	[°C]
E_{sur}	The irradiation from the surroundings.	[W/m ²]
ε	Emissivity	--
E_s	Emitted heat radiation	[W/m ²]
T_{sky}	Temperature of the sky as a surface	[°C]
q_{sky}	Long-wave radiation from the sky	
ε_{sky}	Emissivity of the sky	--
q_c	Convective heat flux	[W/m ²]
T_{air}	The air temperature	[°C]
h_c	The convection heat transfer coefficient	[W/(m ² · °C)]

1 Introduction

1.1 Background

Concrete structures are affected by the climate by air temperature, solar radiation, convection and long wave radiation. The variations of these climate factors will give rise to temperature variations in the structure, causing deformations and tension due to expansions and contractions of the concrete material. Tensions that occur from thermal loads cannot be neglected because they can exceed the effects from other design loads in some cases.

(Larsson, 2012)

In Kiruna, an underground iron mine has been in use since the early 20th century. The iron was created approximately two billion years ago and it exceeds an area of 700 square meters. The transport of the iron from the mine has been made passing a bridge, which is the subject studied in this master thesis. During the year 2014 the bridge was demolished.

Substantial climate data has been used valid for Kiruna. This data include hourly values of air temperature, wind speed, outgoing long wave radiation, diffuse radiation and direct radiation. All this data will serve as input to finite element models, using Abaqus 6.14.

Before the bridge was demolished, temperature and deformation data was collected by Niklas Bagge and his co-workers at LTU. The data collected, by temperature- and strain gauges, will be used to validate if the finite element models are reliable.

The finite element model used has been developed by Ph.D. Oskar Larsson, Lund University, and has already proven to be reliable for slabs and a hollow concrete box cross section (Larsson, 2012). What is unique about this model is that it uses hourly values of the input data and therefore displays results for every hour of the period examined. Normally the temperature variations are calculated with a standard procedure, using for example Eurocode. This model is more accurate because of the use of hourly values.

1.2 Purpose

The purpose of this study is to find out if a two dimensional finite element model is able to capture the temperature variation with precision in a concrete bridge located in Kiruna. An approximative method to calculate the long wave radiation has been used during June, 2009 and August, 2010. It is of interest to see if good results can be achieved with this method.

A further purpose is to find out if the deformations that appear as a result of temperature variation can be captured. This will be done using both a two dimensional and a three dimensional model. The results from the temperature model can be used as input data for estimating the magnitude and variation of the short term deformations.

1.3 Methods

A finite element model created by Oskar Larsson has been used as a basis in this master thesis. All temperature and strain simulations have been made with the finite element software Abaqus 6.14.

MATLAB has been used to calculate the angle of incidence, which in turn is used to calculate the direct solar radiation.

Microsoft Excel has been used to calculate the global solar radiation and long wave heat radiation. The global solar radiation includes direct solar radiation, diffuse solar radiation and reflected solar radiation.

At first an analysis is made of the two dimensional model, created in Abaqus 6.14, for the period of June 2009, August 2010 and June 2014. The input data used is global solar radiation, long wave heat radiation, wind speed and temperature collected from SMHI. The output data is used to analyze how well the model corresponds to the gathered temperature data with the help of the coefficient of determination.

Secondly an analysis is made with two- and three dimensional models to evaluate how stresses and strains occur due to temperature loads. The same input data for the temperature loads is used for the two dimensional simulation as the three dimensional simulation.

2 Theory

A structure is affected by the surrounding climate which causes temperature variations. In the model, the following climate factors have been considered:

- Solar radiation
- Long wave radiation
- Wind
- Temperature

2.1 Solar radiation

The solar radiation reaching an object on earth is called global radiation and is commonly denoted with “G”. The solar radiation reaching a surface is divided into three different kinds of radiation, direct solar radiation, indirect solar radiation and reflected radiation. The intensity of the global radiation depends on a couple of factors with one important factor being the cloudiness of the sky. When it is cloudy the total amount of radiation reaching the earth will likely be lower compared to a sunny day (Larsson, 2012).

Another important factor is the angle of incidence, θ , which is the angle between the normal to the plane and the light striking the surface. If the sunlight falls in, perpendicular to a surface, it is more intense than light that has an inclination to the normal. During the day the sun changes position on the sky which results in a variation of the angle of incidence throughout the day (Larsson, 2012).

The angle of incidence is dependent on the following:

- Time of year
- Altitude and latitude
- The declination between the equator plane and the sun's angle, δ .
- The slope between the surface and the horizontal plane, β .
- Surface azimuth angle, the rotation angle from south for the surface where east is negative and west is positive, γ .
- The angle between direct solar radiation projected on the horizontal surface and south, γ_s .

- Hour angle, ω , which is set to be $15^\circ/\text{hour}$.

Explanations of each coefficient was found in Duffie & Beckmann, (2006).

When the earth rotates around the sun, the sunrays that hit the earth's surface at the local meridian differ from hour to hour with an angle known as the "hour angle". The hour angle is the angle between the sunray and the local meridian.

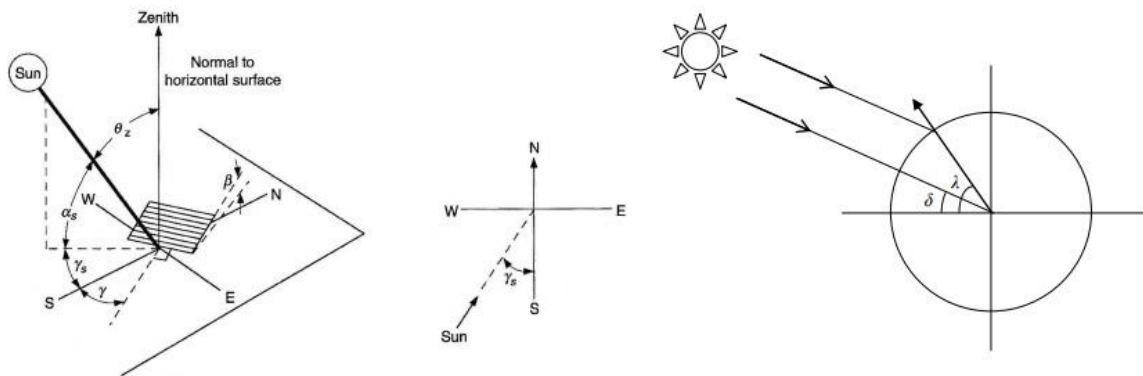


Figure 1. Left figure: Describes the angle of incident. Middle figure: Describes the angle between the sun and the south. Right figure: Describes the declination between the equator plane and the sun's angle, δ , and the angle, λ , between δ and the latitude. (Duffie & Beckman, 2006)

The global solar radiation consists of, as mentioned above, three parts:

- Direct light, I_b [W/m^2]
- Diffuse light, I_d [W/m^2]
- Reflected light, I_g [W/m^2]

Direct light is the light that goes straight from the source, which is the sun, to the object. No indirect light is included in this term. It depends on the direct radiation on a surface perpendicular to the sun $I_{b,n}$ and the angle of incidence, θ . The equation for direct light is:

$$I_b = I_{b,n} \cdot \cos(\theta) \quad [W/m^2]$$

Where

θ The angle of incident

$I_{b,n}$ The direct radiation on a surface perpendicular to the sun

I_b Direct solar radiation

The angle of incidence can be calculated as

$$\theta = \sin(\delta) \sin(\lambda) \cos(\beta) - \sin(\delta) \cos(\lambda) \sin(\beta) \cos(\gamma) + \cos(\delta) \cos(\lambda) \cos(\beta) \cos(\omega) + \cos(\delta) \sin(\lambda) \sin(\beta) \cos(\gamma) \cos(\omega) + \cos(\delta) \sin(\beta) \sin(\gamma) \sin(\omega)$$

Diffuse light will appear when it is cloudy and includes all light that is not direct. When the sunlight hits the atmosphere it is scattered and becomes what is known as diffuse light. The diffuse light can be calculated according to the equation below (Perez & Seals, 1987). This is a simple version of the Perez irradiance model and can be used to estimate hourly irradiance on planes that are tilted. It is based on the diffuse light striking a horizontal surface, $I_{d,h}$, and the parameter β that is the angle between the surface plane and a horizontal plane.

$$I_d = I_{d,h} \left(\frac{1 + \cos(\beta)}{2} \right) \quad [W/m^2]$$

Reflected light first hits the surrounding surfaces and “bounces” before reaching the surface in question. Only tilted surfaces will be subjected to reflected light. The equation used is based on the global radiation on a horizontal surface, I_h . The total reflected light from the ground is expressed as follows:

$$I_g = I_h \cdot \rho_g \left(\frac{1 - \cos(\beta)}{2} \right) \quad [W/m^2]$$

The global radiation can be expressed as a sum of the direct light, diffuse light and reflected light according to this expression:

$$G = I_b + I_d + I_g \quad [W/m^2]$$

Not all radiation hitting an object will be absorbed. The ability of a surface to absorb light is related to its color and texture. A darker surface absorbs solar radiation more efficiently than a lighter surface. An example of a darker surface is the asphalt layer that often is on top of a bridge structure.

To take absorption into account the global radiation is multiplied with an absorption coefficient, a , where a high value means that a majority of the light is absorbed. Thus the energy absorbed is calculated according to (Duffie & Beckman, 2006):

$$q_s = a \cdot G \quad [W/m^2]$$

The chosen value of the solar absorption coefficient is 0.5 for concrete and 0.9 for asphalt. These values are reasonable according to Emerson, (1973). The reason for this choice is that this model is based on the research of Ph.D. Oskar Larsson who used the same values in his FE-models.

Further assumptions for calculation of the global solar radiation are:

- For the south side of the bridge:

Solar azimuth angle, γ_s , is assumed to be 180 degrees.

The angle between the surface and the horizontal plane, β , is assumed to be 90 degrees. It depends on the longitudinal girder which is only affected by the sunlight at its vertical side.

- For the north side of the bridge:

Solar azimuth angle, γ_s , is assumed to be 180 degrees.

The angle between the surface and the horizontal plane, β , is assumed to be 90 degrees. This is because of the longitudinal beam which is only affected by the sunlight at its vertical side.

- For the horizontal part of the bridge:

Solar azimuth angle, γ_s , is assumed to be 0 degrees.

The angle between the surface and the horizontal plane, β , is assumed to be 0 degrees. In reality there is a mild slope of 2.5% and 5.0% between the surface of the bridge and the horizontal plane, in the transversal and longitudinal direction. Though, these slopes are both so small that the results won't be affected, therefore β is set to be zero during calculations of the angle of incident. (Larsson, 2012).

2.2 Solar radiation instruments

There are several different devices to measure solar radiation. Global and diffuse solar radiation can be measured with a pyranometer, in Figure 2 a typical modern pyranometer is shown. Its design allows a 360 degrees view, which enables it to measure global solar radiation. To measure diffuse solar radiation a shadow band can be placed around the pyranometer, see the right side of Figure 2. The shadow band will block the direct sunlight during the day, this way only the diffuse sunlight will be measured. Direct solar radiation can be measured with a pyr heliometer as seen in Figure 3. Unlike the pyranometer it has a restricted view of the sky and is therefore suitable for measuring direct radiation. (Goswami, et al., 1999)

The top of the pyranometer consists of double hemispherical high-transmission glass domes. The reason for having double glasses is to minimize errors that may occur if thermal detectors are used. The pyr heliometer consists of a long tube, which has a detector at the bottom of it. If it is angled towards the sun only about 5 degrees of the sky is visible for the detector. This means that neither reflected light nor diffuse light will get measured, only direct light. (Goswami, et al., 1999)



Figure 2. The image to the left shows a typical pyranometer, which is used for measuring global solar radiation and diffuse solar radiation. The image to the right shows a shadow band placed around a pyranometer in order to exclude the direct sunlight from the measurement.



Figure 3. The picture shows a pyrheliometer, which is used for measuring direct solar radiation. During the measurements the instrument is directed towards the sun (Goswami, et al., 1999)

A BF3 sunshine sensor can be used to measure total solar radiation and diffuse radiation. The direct solar radiation can be calculated by subtracting the diffuse radiation from the total solar radiation. (Wood & Potter, 2002)



Figure 4. The figure shows a BF3 sunshine sensor which is able to measure total solar radiation and diffuse radiation.

2.3 Long-wave heat radiation

Long-wave heat radiation is radiation that is emitted from every material with a temperature above absolute zero. The long-wave radiation can be measured as energy per unit area and is called the emissive power E . If the body would be a perfect emitter the radiation from it is called black-body radiation and is given by the Stefan-Boltzmann law:

$$E_b = \sigma T_s^4 \quad [W/m^2]$$

Where

E_b The emissive power given by the Stefan-Boltzmann law

σ The Stefan-Boltzmann constant equal to $5.67 \cdot 10^{-8} W/(m^2 \cdot K^4)$

T_s The absolute temperature of the body's surface measured in Kelvin, K

To describe the heat flux, the black-body radiation must be reduced by multiplying the emissive power with the emissivity, ε .

$$E_b = \varepsilon \sigma T_s^4 \quad [W/m^2]$$

All surroundings of a structure will affect its body temperature with long wave heat radiation. The surroundings includes everything from buildings, bridges to the ambient air and clouds. The difference between the received heat radiation and the emitted heat radiation on a surface can be calculated as

$$q_r = E_s - E_{sur} = \varepsilon \sigma (T_s^4 - T_{sur}^4) \quad [W/m^2]$$

Where

T_{sur} The temperature of the surroundings

E_{sur} Irradiation from the surroundings

ε Emissivity of the surface

The result of the equation above is the net amount of energy.

Depending on whether a horizontal surface, a vertical surface or a surface facing the ground is analysed, the temperature for each part will be affected in different ways.

For a horizontal surface on for example. the top of the bridge, the surrounding temperature can be assumed to hold the same temperature as the sky, T_{sky} , if the sky is assumed as a fictitious horizontal surface. The definition of T_{sky} is calculated as

$$T_{sky} = \sqrt{\frac{q_{sky}}{\sigma \varepsilon_{sky}}}$$

Where

q_{sky} Long-wave radiation from the sky obtained by measurements

ε_{sky} The sky's emissivity

This results in a radiation heat transfer defined as

$$q_r = \varepsilon \sigma (T_s^4 - T_{sky}^4)$$

Alternatively, the sky temperature can be calculated with the use of different approximations. One such approximation is the following formula by McClellan & Pedersen, (1997):

$$T_{sky,approximate} = T_{air} - 6$$

Usually the emissivity varies between 0.85 and 0.95 for a concrete surface. The mean value of 0.9 is used in the model of this master thesis. The sky emissivity and the concrete emissivity is assumed to have the same value (Threlkeld 1970).

The vertical surface on the outer side of the north or south side of the bridge is influenced by both the temperature of the ground and the sky. Therefore a fictitious equivalent temperature is calculated combining the ground and the sky temperature defined as

$$T_{eq} = \frac{T_{sky} + T_{air}}{2}$$

The surface facing the ground will only be affected by the ground in terms of long-wave radiation. The ground temperature is assumed to be equal to the air temperature and the long wave heat radiation can therefore be calculated as:

$$q_r = \varepsilon \sigma (T_s^4 - T_{air}^4)$$

2.4 Convection

Convection can be described as the transferring of energy between a boundary layer and fluid in motion, where the boundary layer is a surface. It consists of diffusion which is the random movement of fluid molecules and the bulk fluid motion known as advection (Incropera, et al., 2007). Convection can be divided into forced convection and natural convection. Forced convection is when wind forces the air above a surface to move. Natural convection is when buoyancy forces act upon the air for example when the air temperature differs. Diffusion and advection are dependent on the velocity of the air.

Particles that lie close to the surface, so that contact occurs, are assumed to have a zero velocity. This is where diffusion is the dominant part. The further away the particles are from the surface, the more the velocity increases in the fluid thus the advection increases and the diffusion acting on the surface decreases.

Convective heat flux can be calculated as

$$q_c = h_c(T_s - T_{air})$$

T_s The surface temperature [$^{\circ}C$]

T_{air} The air temperature [$^{\circ}C$]

h_c The convection heat transfer coefficient $W/(m^2 \cdot ^{\circ}C)$ which is depending on the roughness of the surface and nature of the fluid motion

According to Nevander & Elmarsson, (2001) there are two different expressions for the heat transfer coefficient. They state that for lower wind speeds the natural convection is dominating and following equation is used in this case:

$$h_c = 6 + 4V \qquad \qquad \qquad \text{if } V \leq 5m/s$$

and for higher wind speeds the concrete will be affected by forced convection:

$$h_c = 7.4V^{0.78} \qquad \qquad \qquad \text{if } V > 5m/s$$

The total amount of convection that can affect the concrete during a day can be calculated if there is enough temperature data.

2.5 Heat transfer

When two bodies come in contact heat transfer will occur between the bodies. The total rate of heat conduction between them is a function depending on temperature difference.

Conduction occur in all matter, independent of whether the material is gas, solid or liquid.

For example, a steel bar heated in one end will eventually warm the other end. This is because the molecules in the warmer part of the steel bar will vibrate more when heated than the molecules in the cooler part of the steel bar, hence an energy exchange will occur between the molecules. Due to the vibrations between the molecules, kinetic energy will also exchange between the molecules. (M. Jiji, 2009)

Analysis of heat transfer can be described with Fourier's law. Heat transfer can be described with what is known as *heat flux*, which is defined as the heat flow rate per unit surface area normal to the direction (W/m^2). It is written as:

$$q_n'' = -k_n \frac{\partial T}{\partial n}$$

The equation above, q_n , is the heat transfer perpendicular to the direction of heat flow.

Thermal conductivity, k_n , ($W/(m \cdot ^\circ C)$) is the temperature gradient in the n -direction. This means for the x -, y - and z -direction that heat flux is written as follows:

$$q_x'' = -k_x \frac{\partial T}{\partial x}$$

$$q_y'' = -k_y \frac{\partial T}{\partial y}$$

$$q_z'' = -k_z \frac{\partial T}{\partial z}$$

Thermal conductivity is dependent on the material's structure. For example, a material can be isotropic, anisotropic or orthotropic. Material properties differs in the number of planes of symmetry. For an isotropic material, the number of symmetry planes are infinite which means that it has the same properties in all directions. For example, if a body is exposed to stress at a specific point, it will spread through the material, in all directions, with the same spreading rate. Steel is an example of an isotropic material.

Anisotropic material properties are distinguished from isotropic material properties by being directionally dependent. This means that it will have different properties in different directions.

Orthotropic material is a sort of anisotropic material. The material properties for an orthotropic material are different along three unique axes compared to anisotropic material which only has one symmetry plane (Barbero, 2008). Wood, for example, has different properties in three mutually perpendicular directions. The radial direction, the circumferential direction and the axial direction. This results in different behavior of the material when exposed to different kinds of loading. Concrete can be treated as an isotropic material when it comes to heat flow, even though it is not an isotropic material in reality.

$\frac{\partial T}{\partial n}$ is the temperature gradient in the n -direction meaning that the temperature will spread in one-, two- or three dimensions, depending on whether the material is isotropic, anisotropic or orthotropic. For a three-dimensional case, $\frac{\partial T}{\partial n}$ can be written as

$$\frac{\partial T}{\partial n} = \left(\frac{\partial T}{\partial x} + \frac{\partial T}{\partial y} + \frac{\partial T}{\partial z} \right)$$

The general heat conduction is written

$$\rho c \frac{\partial T}{\partial t} = k \left(\frac{\partial^2 T}{\partial x^2} + \frac{\partial^2 T}{\partial y^2} + \frac{\partial^2 T}{\partial z^2} \right) + q_v$$

Where

ρ Density [kg/m^3]

c Specific heat capacity [$J/(kg \cdot ^\circ C)$]

k Thermal conductivity [$W/(m \cdot ^\circ C)$]

$\frac{\partial T}{\partial t}$ Temperature change over time

$\frac{\partial^2 T}{\partial x^2}, \frac{\partial^2 T}{\partial y^2}, \frac{\partial^2 T}{\partial z^2}$ The second spatial derivatives of temperature in the x-, y- and z-direction

q_v The heat that will be generated because of hydration in the concrete

The bridge was built in the 1950's hence an assumption is made that there is no more heat generated in the concrete by hydration, therefore $q_v = 0$.

2.6 Concrete

Concrete is often used as a building material in multistorey buildings, arenas, malls and other complex and large structures. It possesses great material properties when it comes to handling large forces hence it is a popular building material.

Concrete structures can take great compressive stresses but the material possesses an inability to handle tensile stresses. Therefore concrete structures are usually built with steel reinforcement which in possesses great capacity to handle tensile stresses.

In this master thesis, the reinforcement is not considered during the modelling due to the low amount of steel in comparison with the amount of concrete. The stress levels from temperature loads are low and therefore the concrete can be assumed to behave linearly (Neville, 1995).

2.6.1 Material components

Concrete is a composite material consisting of cement, aggregates, water and sometimes adden admixtures, divided in a certain way.

Cement is the most important part of the concrete, with the ability to bind and harden all the components in the concrete mixture. The most common type of cement is the Portland cement which is not a brand name but a mix of specific components. In combination with water, the cement becomes a paste that binds with the aggregates and hardens the mixture to become the final concrete (Burström, 2007).

The aggregates are classified as fine aggregates and coarse aggregates where the fine aggregates usually are various sands and the coarse aggregates are gravel or crushed stone. If the interrelation between the different aggregates are as desired, the cavity which occur between the bigger aggregates will be filled out by the finer aggregates and therefore the material dense will increase. This results in higher density of the material and higher strength (Wilby, 1983/1991).

Water is added to start the hardening process between the water and cement to create the concrete by hydration of the cement. The total amount of water in relation to the amount of cement is known as the water-cement ratio. It is the ratio between the weight of the water in comparison to the weight of the cement. By changing the w/c ratio, different properties can be given to the concrete.

$$w/c - ratio = \frac{W}{C}$$

Where

W The total amount of water in [kg]

C The total amount of cement in [kg]

Admixtures can be e.g. retarders or accelerators with the property of slowing down the hardening part or accelerating it. Retarders can be useful if the mixture should be transported a long way or if the heat needs to be lowered during the hardening part. The hardening part is an exothermic procedure which means that heat is generated and therefore a retarder can be useful to slow down the whole procedure (Burström, 2007).

2.6.2 Specific heat capacity

The specific heat capacity describes the amount of heat needed to raise the temperature of one kilo of mass by one degree Celsius. Alternatively Kelvin can be used instead of Celsius. The unit of specific heat capacity is $J/(kg \cdot K)$. If there is a body with a certain mass, and it is of interest to calculate the amount of heat needed to increase its temperature a certain amount of degrees, the following formula can be used where the specific heat capacity is included (Larsson, 2012).

$$Q = c \cdot m \cdot \Delta T \quad [J]$$

Specific heat capacity varies in general between 800 and 1000 $J/(kg \cdot ^\circ C)$ according to (Ljungskrantz, et al., 1994).

2.6.3 Density

The density is the mass per unit volume. Density of concrete varies depending on the mixture of the components. Described with a formula the following expression for density applies:

$$\rho = \frac{m}{V} \quad [kg/m^3]$$

According to table 2.2 in (Larsson, 2012) the density used in several authors research varies between 2350 and 2500 kg/m^3 .

2.6.4 Conductivity

Thermal conductivity is the materials capacity of conducting heat. It is dependent on the materials composition, density, moisture content in the material and the conductivity of the included components (Larsson, 2012). The thermal conductivity for concrete is in general varying between 1.4 and 3.6 $W/(kg \cdot ^\circ C)$ according to (Neville, 1995).

2.6.5 Young's Modulus

Young's modulus describes the relationship between stress and strain in a material. It is also known as the elastic modulus. If a load is applied to a body which deforms at first but goes back to its original shape after the load is removed, the bodies material is elastic. The stiffer a material is, the higher young's modulus is.

2.6.6 Thermal expansion coefficient

Thermal expansion is how a material tends to change in shape due to temperature change. Thermal expansion depends on, for concrete, several factors. It is dependent on the moisture content, the thermal expansion of the aggregate and the cement paste. (Ljungskrantz, et al., 1994)

According to Eurocode (1991-1-5, 2003) the expansion coefficient for concrete is $\alpha = 10 \cdot 10^{-6} \text{ m}/(\text{m} \cdot ^\circ\text{C})$.

2.7 Asphalt

Asphalt concrete is a composite material and, depending on what it is supposed to be used to, the components might be different. It is a composition of mineral aggregates, bitumen (asphalt) and binders. Normally it is used in road construction but since asphalt is waterproof it can also be used at the rooftops of buildings. Asphalt has the same typ of material properties as concrete when it comes to thermal conductivity, although the conductivity of asphalt differs somewhat from the conductivity of concrete in magnitude.

2.8 Coefficient of determination

In a case when two different kinds of data, for example data from measurements and data from calculations are to be compared and interpreted, the coefficient of determination can be used. The coefficient of determination is a number which indicates how well data and a statistical model fits. It is dimensionless, making it a tool that can be used in different areas. The range of values of R^2 should correspond to a perfect fit or a complete lack of fit. These values should be in the range of $0 \leq R^2 \leq 1$ where 0 corresponds to a complete lack of fit and 1 corresponds to a perfect fit. In general, a very good fit is equal to or greater than 0.8 (Menard, 2000). The equation can be written as:

$$R^2 = 1 - \frac{SS_{res}}{SS_{tot}}$$

Where

$$SS_{res} = \sum_i (y_i - \hat{y})^2$$

$$SS_{tot} = \sum_i (y_i - \bar{y})^2$$

$$\bar{y} = \frac{1}{n} \sum_{i=1}^n y_i$$

y_i	The modelled data
\hat{y}	The measured data
\bar{y}	The mean value of the observed data
n	The number of measurements

3 Model

A two-dimensional model has been made to calculate the temperature variation and strain variation in a bridge cross section. This model has been given an approximate geometry based on drawings of the Kiruna bridge. In the model the positions of the temperature gauges and the strain gauges have been marked. Further, an extended model has been made to calculate the strain variation in the bridge in three dimensions. The geometry is for the western part of the bridge, that is the first 18 meters of the bridge. A more detailed description of the geometries follows in Chapter 3.4.

Table 1. This is an overview of what the two dimensional model and the three dimensional model are used for. As seen most of the examinations have been made using the two dimensional model.

<i>Model</i>	<i>Studied</i>	<i>Description</i>	<i>Start time(s)</i>	<i>Stop time(s)</i>
2D	Temperature	Temperature variation is studied.	2009-06-01	2009-06-30
		The temperature is calculated for every hour.	2010-08-01	2010-08-30
			2014-06-14	2014-06-15
	Strain	Strain variation is studied. The strain is calculated for every hour.	2009-06-01	2009-06-30
	Temperature	Temperature variations further into the structure. Change in amplitude.	2009-06-01	2009-06-30
3D	Strain	Strain variation is studied. The strain is calculated for every hour. Temperature from 2D used in 3D.	2009-06-01	2009-06-30

3.1 Limitations and Assumptions

Necessary limitations and assumptions were made for the bridge regarding its geometry and its material properties. Below follows a list of the model simplifications.

- The concrete is considered linear because the strain levels are low.
- In reality there are bending- and crack reinforcement in the bridge. Due to the small amount of reinforcement in relation to the total amount of concrete follows that the

reinforcement has not been accounted for in the model. The calculations only include concrete and asphalt as materials.

- The three dimensional model is modelled between the abutment at the west side and the first columns at span one. At the eastern part the bridge is assumed to be supported in a way which allows the whole cross section to move in the x- and y-direction and to rotate around the z-axis in the model, see Figur 30 .
- The bridge surface has inclinations in the longitudinal and the transversal directions of 5.0% and 2.5%. The inclination in the longitudinal direction is not included in the three dimensional model.
- The longitudinal girders in the bridge increase in width from 410mm to 650mm, 4.0 meters from the intermediate supports. This was not included in the model were the girders instead had a constant width of 410mm.
- The bridge is slightly curved in the horizontal plane. Between the abutments to the first column, at span 1, there is a small curvature of the bridge. The curvature was expected not to influence the results in particular, especially the temperature results.
- No consideration has been taken to temperature effects from hydration of the concrete but instead only temperature effects from the environment.
- The ground temperature is assumed to have the same temperature as the bottom sides of the bridge, hence there is no heat exchange in form of outgoing long-wave radiation.

3.2 Choice of material properties

The temperature distribution of the cross section is affected by the choice of material properties. It is therefore important to choose reasonable values, or else the model will not be accurate. The material properties that are relevant for the models are specific heat capacity, density, conductivity, Young's Modulus, Poisson's Ratio, thermal expansion coefficient and the absorption coefficient

The main part of the bridge cross section consists of concrete. On top of the bridge lies a concrete layer and at the very top lies an asphalt pavement. The asphalt pavement covers the entire top surface of the bridge and will be exposed to the sun during the day.

The chosen values for specific heat capacity, density and conductivity are listed in the table below. The concrete layer is assumed to have the same properties as the rest of the concrete. A comparison between concrete and asphalt shows that the specific heat capacity and density are roughly the same for these materials. The conductivity on the other hand is much lower for asphalt than for concrete. In this master thesis, 2.5 W/(kg · C) has been used as thermal conductivity for the concrete and 1.5 W/(kg · C) for the asphalt. All values were chosen from literature Larsson (2012) and not from actual measurements of the material properties.

Table 2. The material properties for the concrete, the concrete layer and the asphalt are shown in this table. The concrete and the concrete layer have been given identical properties.

	<i>Specific Heat Capacity</i> [J/(kg·C)]	<i>Density</i> [kg/m ³]	<i>Conductivity</i> [W/(kg·C)]	<i>Young's Modulus</i> [GPa]	<i>Poisson's Ratio</i>	<i>Expansion coefficient</i> alpha	<i>Solar absorption coefficient</i>
<i>Concrete</i>	900	2400	2.5	30	0.2	10·10 ⁻⁶	0.5
<i>Concrete layer</i>	900	2400	2.5	30	0.2	10·10 ⁻⁶	0.5
<i>Asphalt layer</i>	900	2400	1.5	30	0.2	10·10 ⁻⁶	0.9

3.3 Input data

The wind speed was used to calculate the convection. It was received from the Swedish Meteorological and Hydrological Institute. The wind is used to calculate the convection in Abaqus. The air temperature is used for calculating the coefficient of convection and for calculating the sky temperature as if it were a surface. The direct radiation data and the diffuse radiation data was received from earlier measurements made on site. The direct radiation and the diffuse radiation are used to calculate the global radiation. The diffuse radiation was received from earlier measurements made on site.

The solar radiation data was retrieved from STRÅNG data base for the year of 2009 and 2010. The data was produced by the Swedish Environmental Agency and the Swedish Radiation Protection Authority. During the year of 2014, the solar radiation (direct and diffuse radiation) was retrieved from measurements made on site in Kiruna by Complab.

3.4 Geometry

The bridge has a geometry according to Figure 5. It is the western side of the bridge that has been studied.

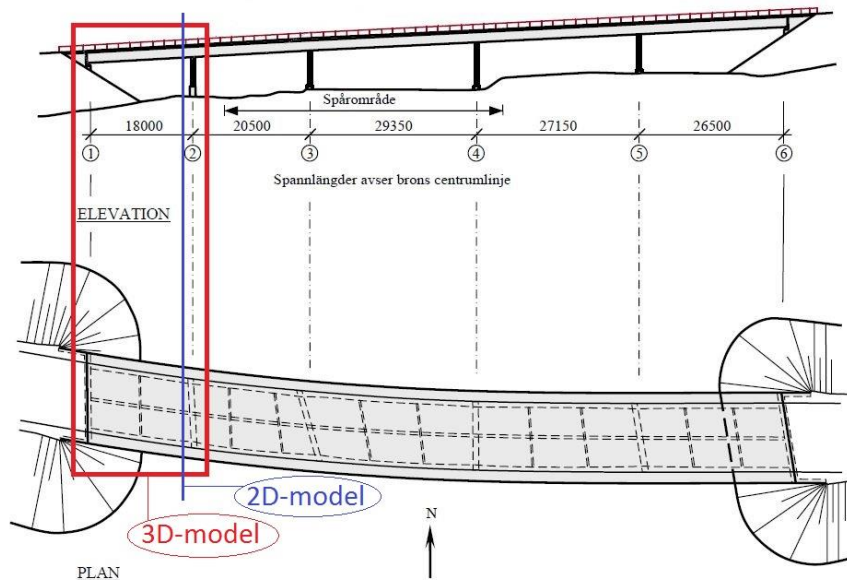


Figure 5. In the figure the three dimensional part of the bridge that has been modelled is marked within a red rectangle with the label “3D-model”. The two dimensional cross section which has been modelled is marked with a blue line with the label “2D-model”. The pictures were taken from the technical report (Elfgren, et al., 2011).

3.4.1 Bridge geometry for two dimensions

To be able to accurately compare the calculated values with the measured values it is of great importance that the geometry of the concrete section is as correct as possible. The geometry below is considered to be accurate and has been used in all finite element calculations. The cross section that has been used in the two dimensional model is located 0.3 meter from the columns in span one.

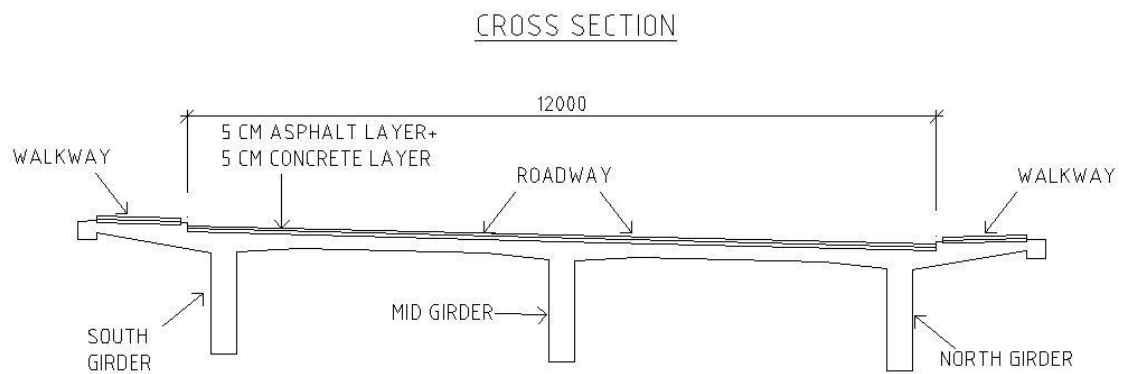


Figure 6. Cross section of the bridge "Gruvvägsbron" in Kiruna. It is built of concrete. There is an asphalt layer on the roadway and the walkway.

3.4.2 Bridge geometry for three dimensions

The western part of the bridge has been used in the subsequent strain analysis. It is the first 18 meters of the bridge that is of interest. That is the part from land, the western abutment, to the first sets of columns. The figure below shows this part in three dimensions.

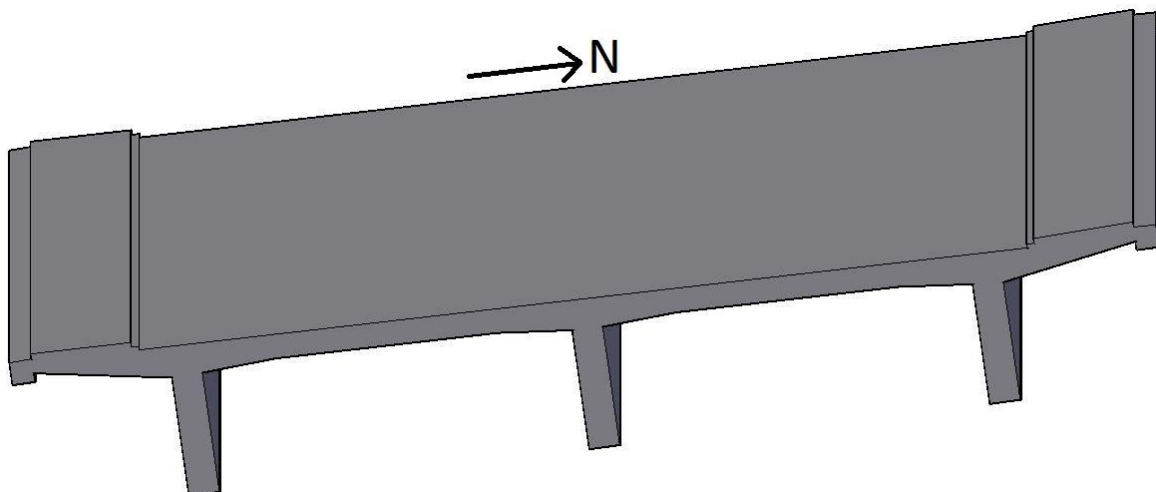


Figure 7. The geometry of the three dimensional model. The direction towards the north is indicated in the figure.

3.5 Measuring gauges locations

Data from temperature gauges were used to validate the calculated temperature from the temperature model. In the same way, data from strain gauges were used to validate the strain calculated with the strain models. The locations of the temperature gauges and strain gauges are shown below.

3.5.1 Temperature gauges

For the year of 2009 and 2010 the gauges were placed as in figure 8. The number of temperature gauges used during these periods were three. The gauges were positioned on the longitudinal reinforcement for crack 890 millimeters from the bottom (Elfgren, et al., 2011). It was estimated that all gauges were located 40 millimeters into the beam.

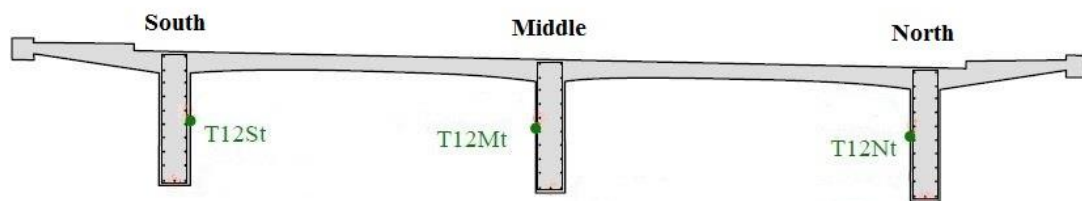


Figure 8. Locations of the temperature gauges from the measurements of 2009. As seen there is one gauge placed on each girder. All gauges are placed 890 millimeters from the bottom of the girders. This picture is taken from a report from Luleå University (Elfgren, et al., 2011)

For the year of 2014 the gauges were located as in the figure 9, in total there are eight gauges. The measuring equipment consists of temperature wires and were inserted into holes to 30 mm for measuring gauge 1, 3 and 6; 60 mm for measuring gauge 2 and 7; 50 mm for measuring gauge 4 and 8; 80 mm for measuring gauge 5 (Elfgren, et al., 2015). These placements are also compiled in the table below. Further, the gauges for the year of 2014 were placed at different locations along the bridge in span two and three.

Table 3. The depth of the temperature gauges range from 30 millimeter to 80 millimeters. The gauge depth is the distance from the surface to the gauge location in the concrete.

Gauge number	1	2	3	4	5	6	7	8
Depth [mm]	30	60	30	50	80	30	60	50

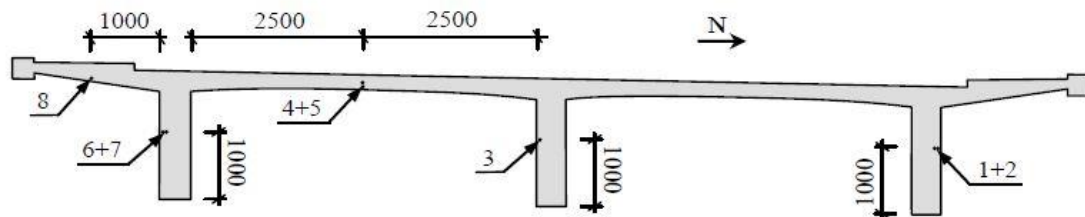


Figure 9. Locations of the temperature gauges from the measurements of 2014. The gauges numbered 1-3 and 6-7 are located on the beams 1000 millimeters from the bottom according to the picture. The gauges numbered 4-5 and 8 are located on the underside of the horizontal slabs as seen. The picture is taken from a previous report about this bridge (Elfgren, et al., 2015).

3.5.2 Strain gauges

For the strain measurements, performed in 2009 and 2010, the gauges were placed as in the figure below. All the gauges were placed 40mm into the structure, from the surface, and 0.3m from the supports except from St12Sb2-3 which were placed at a distance of 1.0m and 1.7 m from the supports. St12St, St12Mt and St12Nt are all placed at the height of 1095mm from the bottom of each girder. St12St1-3, St12Mb and St12Nb are placed in the middle of each girder.

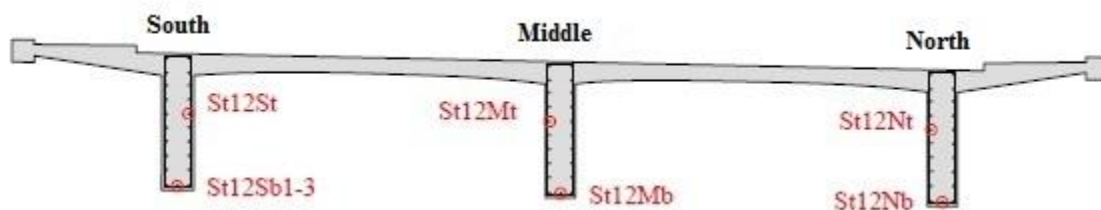


Figure 10. Locations of the strain gauges for the measurements of 2009 and 2010. All strain gauges were placed with a distance of 40mm into the structure. St12Sb1-3, St12Mb and St12Nb are placed in the middle of each girder. St12St, St12Mt and St12Nt are placed at a height of 1095mm from the bottom of the girders. All the strain gauges were placed 0.3m from the supports except from St12Sb2-3 which were placed at a distance of 1.0m and 1.7m from the supports (Elfgren, et al., 2011).

4 Temperature simulation in two dimensions

4.1 Finite Element

For calculations of effects from temperature loads on complex structures such as a prestressed concrete bridge, computer programs are often needed. The finite element method is used when a physical phenomenon needs to be modelled, such as for our case with strain and temperature distributions.

An analysis on a region is usually performed with finite element analysis. The whole region is divided into small elements and the approximation is made on every element instead of the whole region. Together, the elements form a collection known as a mesh. For a more accurate approximation, smaller element-size can be used (Ottosen & Petersson, 1992).

The elements are formed as either quadrilaterals or triangles. Note that the quadrilaterals and triangles could take the form of squares, rhomboids, rectangles, hexahedra or tetrahedrals depending on whether the geometry is in two or three dimensions. Every element contains nodes at the boundaries, linking the adjacent elements together. The approximations are made by known functions as polynomial equations of one or higher order. (Pepper & Heinrich, 2006).

At the boundaries of a surface, the so called boundary condition denotes how the surface is allowed to move, hence how the region will behave when a load is applied. For example, analysis is made on a beam which is placed between two columns and fixed in both ends. A point load is applied in the middle of the beam. At the ends where the beam is supposed to be attached to the columns, boundary conditions are created instead of modelling the columns, containing the information on how a fixed beam is allowed to behave when exposed to pressure. If a load is applied to the region, each small finite element will exhibit a behavior depending on the load and the magnitude. The results show how the whole beam will behave.

Although keep in mind that the FE-method will not give the exact answer to the problem but instead an approximation as close to the answer as possible (Ottosen & Petersson, 1992).

4.2 Loads and interactions in Abaqus

4.2.1 Use of loads and interactions

In Abaqus “loads” are applied onto a geometry and an “interaction” is how the geometry interacts with the environment. The loads used in our model include global radiation on a horizontal surface and global radiation on vertical surfaces. The interactions include the sky temperature, the vertical sky temperature and the convection as described in chapter 2.

4.2.2 Horizontal Global Radiation

Horizontal global radiation is the global radiation calculated on a horizontal surface. In this case the horizontal surface is the top of the bridge that is the roadway and the walkway. The majority of the horizontal surface consists of asphalt material. A part of the horizontal surface consists of concrete material. The absorption coefficient is 0.9 for asphalt and 0.5 for concrete. (Larsson, 2012)

To take the position of the sun into account, calculation of the horizontal solar radiation has been made according to Chapter 2.1.

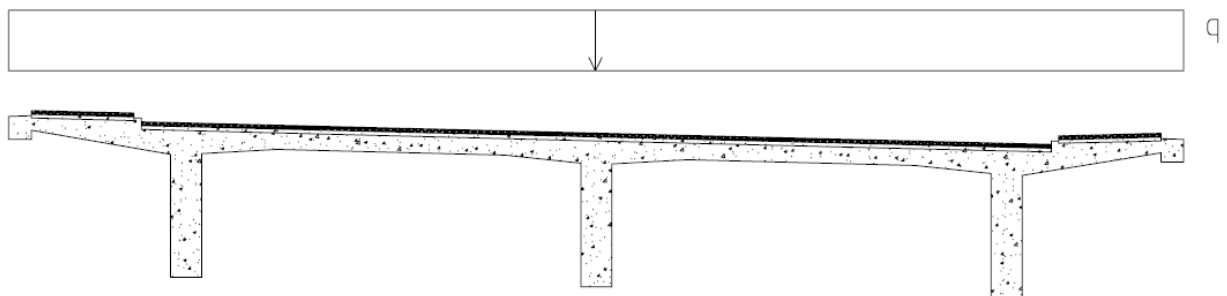


Figure 11. The figure illustrates how the horizontal global solar radiation acts upon the whole upper horizontal surface of the bridge. In reality, the asphalt layer and the concrete layer do not have the exact same material properties hence the thermal actions on the bridge will be distributed differently through it.

4.2.3 Vertical Global Radiation

The vertical global radiation is the global radiation on the vertical surfaces of the bridge, which is the south and the north side of the bridge. To take the position of the sun into account, calculation of the vertical solar radiation has been made according to Chapter 2.1. The overhang at the southern and northern side of the bridge is considered affected by the global solar radiation only at its vertical parts whereas the inclined parts on the bottom part of the overhangs is assumed not to be affected. The magnitude of the direct solar radiation depends on the position of the sun, in other words it depends on whether the surfaces are angled towards the sun and the magnitude of this angle.

Now consider the vertical surfaces of the outer girders pointing outwards. When the sun lies low in the sky all of these vertical surfaces will be exposed to direct solar radiation. But when the sun is higher in the sky, the upper part of the surfaces will get shadowed due to the overhang on each side of the bridge. To take this into consideration each of the vertical surfaces were divided into a lower part and an upper part with different values of the direct solar radiation.



Figure 12. Figure illustrating how the vertical global solar radiation acts at the southern and the northern side of the bridge.

4.2.4 Convection

The model interacts with the surrounding by convection and by outgoing long wave radiation. The whole structure is affected by convection, Figure 13 shows a cross section of the bridge and all the surfaces affected by convection.

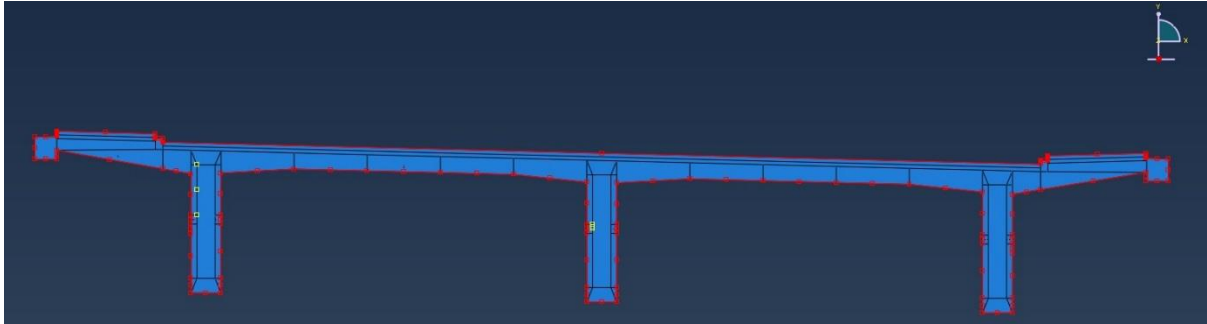


Figure 13. The figure illustrates how the convection layer (the red line) affects the whole outer surfaces of the bridge cross section. Figure is retrieved from the two dimensional cross section model in the software Abaqus 6.14.

4.2.5 Long wave heat radiation

The surfaces facing the sky will be affected by the cold sky. In the finite element model this is simulated by considering the sky as a surface, the sky has the temperature T_{sky} according to Chapter 2.3. The vertical surfaces on the southern and northern side of the bridge will also be affected by the cold sky. These surfaces are not angled directly towards the sky, therefore an equivalent temperature is used according to Chapter 2.3.

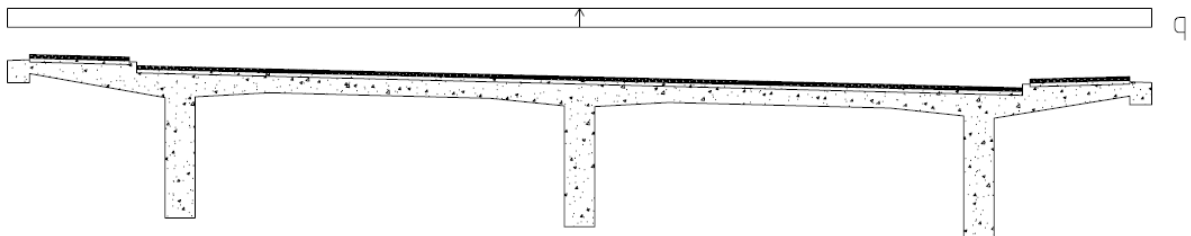


Figure 14. Outgoing horizontal long wave solar radiation. The figure show how the outgoing long wave radiation acts over the whole horizontal surface. The asphalt layer and the concrete does not emitt the same amount of long wave radiation hence the figure just illustrates how the horizontal long wave solar radiation is.

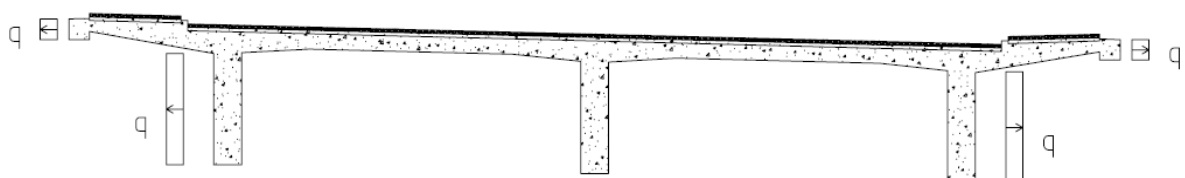


Figure 15. Outgoing vertical long wave solar radiation. The figure illustrates how the outgoing long wave radiation acts on the south and the north side of the bridge. Assumption were made that the tilted surfaces not emitt any long wave radiation.

4.3 Mesh for calculating the temperature

The mesh element used is DC2D4, which is a 4-node linear heat transfer element with four edges. It has been made sure that there are nodes corresponding to the location of the temperature gauges. This way the temperature can easily be extracted from these particular nodes. An element size of 20 millimeters has been used for the simulations during the year of 2009 and the year of 2010. An element size of 30 millimeters have been used for the simulation during June 2014. The reason for the larger element size for the year of 2014 is due to the fact that the mesh became more symmetrical that way and that the measuring points were easier to identify in the model with these mesh variations.

4.4 Temperature results for 2009

The results show that it works well to use the approximate method which was used to calculate the outgoing long wave radiation. The x-axis shows time in days and the y-axis shows the corresponding temperature. The measured data is named “observed” in the graph. The values calculated from the simulation in Abaqus are named “calculated”.

4.4.1 Measuring point TSÖ

The result from the measuring point TSÖ, placed at the southern girder, is shown in figure 16. Values at the x-axis show the days of June, and the corresponding value from the node is shown at the y-axis. The calculated values are fairly close to the observed values. A residual coefficient was calculated to 0.86 for the period of June 5th to June 30th. As seen in the graph, the approximate set up time for the calculated values to adjust to the observed values are two to three days. To make sure the coefficient of determination is calculated fairly, an interval for the first four days were not included. This because it takes a few days for the finite element model to adapt. In general the calculated values are somewhat underestimated compared to the observed values. Also, the variation from day to night is more pronounced for the calculated values.

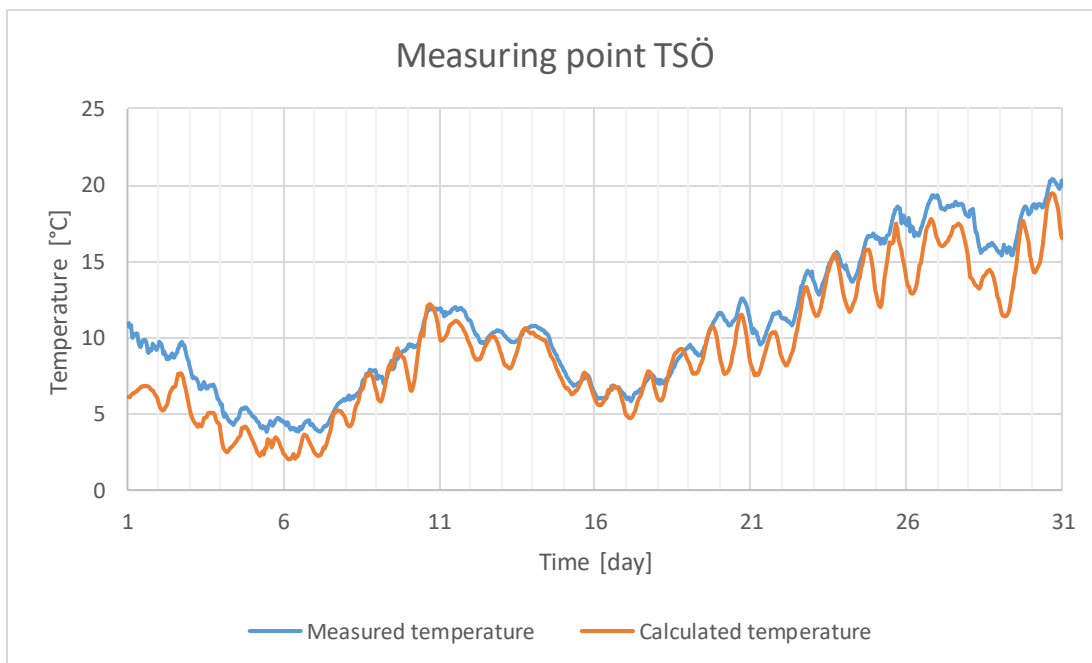


Figure 16. An overview of the temperature variation for measuring point TSÖ during the month of June. The observed data appears during the whole month. The coefficient of determination is calculated from day five to the end of the month because of the need for the calculated temperature to adjust in the beginning of the month.

4.4.2 Measuring point TMÖ

The result in figure 17 is for measuring point TMÖ, located at the mid girder. The coefficient of determination is 0.97 for the measuring point placed at the mid girder during the period of June 5th to June 30th, 2009. The calculated values are very close to the observed values for measuring point TMÖ considering both the coefficient of determination, which is very close to 1, and that the graph shows similarity between the curves.

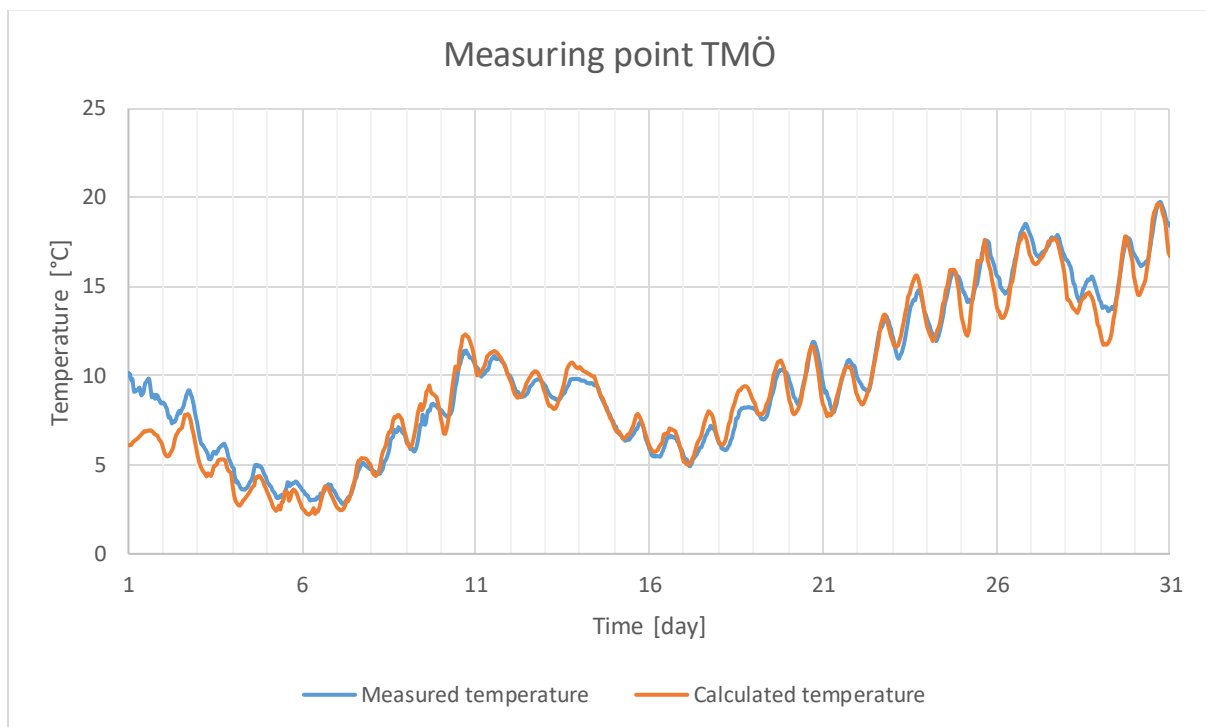


Figure 17. An overview of the temperature variation for measuring point TMÖ during the month of June. The observed data appears during the whole month. The coefficient of determination is calculated from day five to the end of the month because of the need for the calculated temperature to adjust in the beginning of the month.

4.4.3 Measuring point TNÖ

The coefficient of determination is 0.95 for the measuring point placed at the northern girder during the period of June 5th to June 30th. The calculated values are very close to the observed values for measuring point TNÖ. Measuring point TNÖ reveals a close closeness in the graph between the two curves and the coefficient of determination is very close to 1.

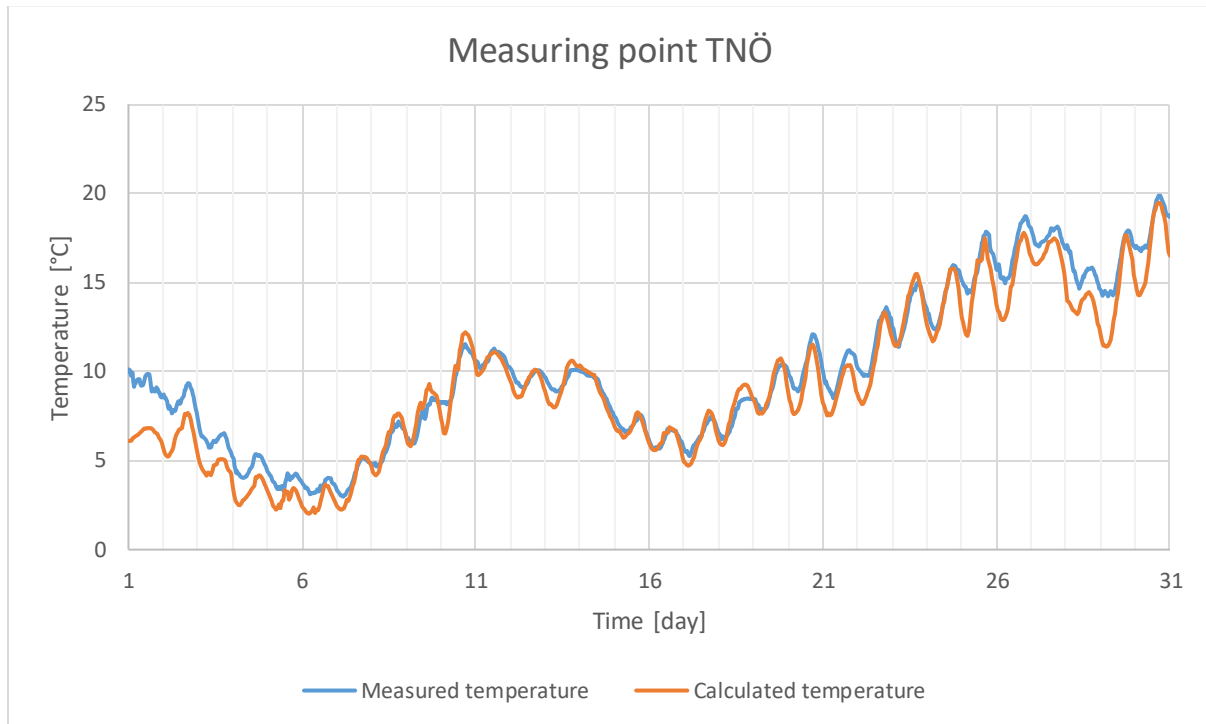


Figure 18. An overview of the temperature variation for measuring point TNO during the month of June. The observed data appears during the whole month. The coefficient of determination is calculated from day five to the end of the month because of the need for the calculated temperature to adjust in the beginning of the month.

4.5 Temperature results for 2010

The result below is for measuring point TMÖ. The temperature results for 2010 also show similarity between the measured data and the calculated data for each measuring point.

However, in general the calculated temperature exhibits larger amplitudes than the measured temperature in all three measuring points.

4.5.1 Measuring point TSÖ

The result from measuring point TSÖ, placed at the southern girder, is shown in figure 19.

The x-axis show the days of August with corresponding temperature value from the node shown at the y-axis. The calculated values show the same temperature variation as the measured value. The temperature variation during the day is however larger for the calculated values and it lies beneath the measured temperature for almost the whole period. A residual coefficient was calculated to 0.837 for the period of August 5th to August 31st. The first four days are not included in the calculation of the coefficient of determination.

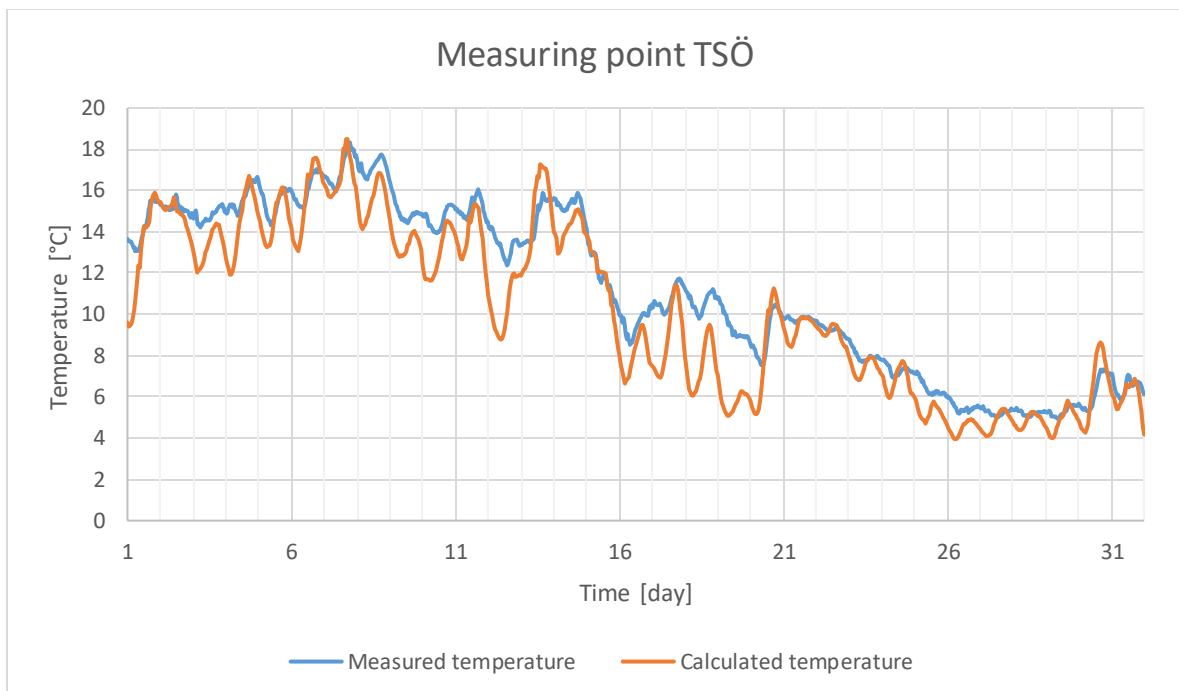


Figure 19. An overview of the temperature variation for measuring point TSÖ during the month of August, 2010. The observed data appears during the whole month. The coefficient of determination is calculated from day five to the end of the month because of the need for the calculated temperature to adjust in the beginning of the month.

4.5.2 Measuring point TMÖ

The coefficient of determination is 0.94 for the measuring point, TMÖ, placed at the mid girder during the period of August 5th to August 31st, 2010. The calculated values follow the observed measurements at measuring point TMÖ but the temperature variation for the calculated temperature is slightly larger for almost every day of the month. Note that the temperature curves follow each other with more certainty during the period of the 5th to approximately the 11th and from the 21st to the 31st. Both the coefficient of determination and the temperature curves show that the model is very accurate.

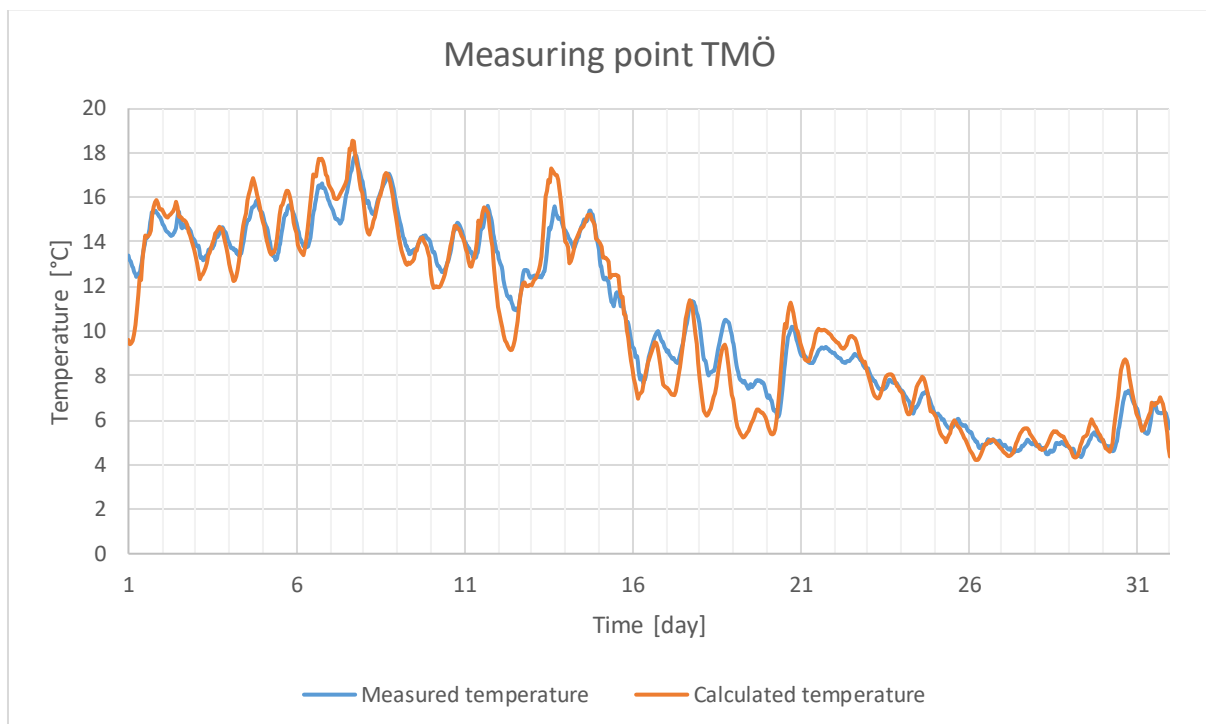


Figure 20. An overview of the temperature variation for measuring point TMÖ during the month of August, 2010. The observed data appears during the whole month. The coefficient of determination is calculated from day five to the end of the month because of the need for the calculated temperature to adjust in the beginning of the month.

4.5.3 Measuring point TNÖ

The coefficient of determination is calculated to 0.912 for the measuring point placed at the northern girder during the period of August 5th to August 31st. The temperature variation between the calculated measurements and measuring point TNÖ reveal a similar behaviour and a closeness according to both the coefficient of determination and the curves in the chart, as can be seen in figure 21. The calculated temperature show larger amplitudes though they are very small in general during the whole period. Between approximately the 11th and the 20th of August, the calculated temperature exhibits larger amplitudes then during the period before the 11th and the period after the 20th in comparison to how much more similar it were to the measured temperature during these two periods of August.

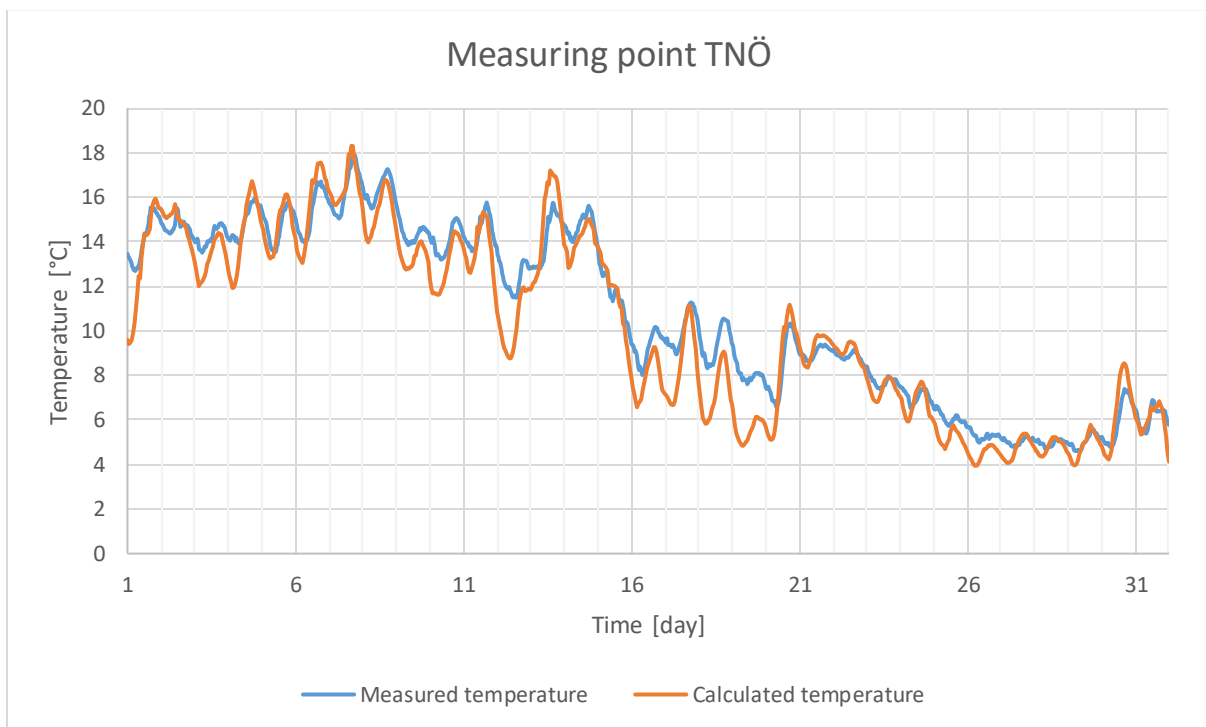


Figure 21. An overview of the temperature variation for measuring point TNO during the month of August, 2010. The observed data appears during the whole month. The coefficient of determination is calculated from day five to the end of the month because of the need for the calculated temperature to adjust in the beginning of the month.

4.6 Temperature results for 2014

The measuring data from June 2014 only covers six hours in total during the middle of June. This measuring period is too short to create a coefficient of determination with a good estimation. Therefore the results are shown by graphs only.

For measuring point 1 the difference between observed and calculated values is about three degrees in magnitude. For measuring point 2 the difference is about one degree. For measuring points 3 and 4 the difference is only about half a degree. The result for measuring point 5 is very good, the difference is approximately half a degree or less.

When it comes to measuring point 6 the accuracy is very good during the three first hours. The remaining three hours are also very good with a difference of 0.4 degree. The approximate difference for measuring point 7 and measuring point 8 are 1.0 and 0.1 degree respectively. For each measuring point there are two graphs. The first one shows an overview of the temperature variation during the month of June. The second shows a more detailed comparison between the observed values and the calculated values. The graphs below show the result for measuring point 1 and measuring point . The remaining six measuring points can be found in appendix 10.1.

Measuring point 1 is located at the northern girder of the bridge cross section.

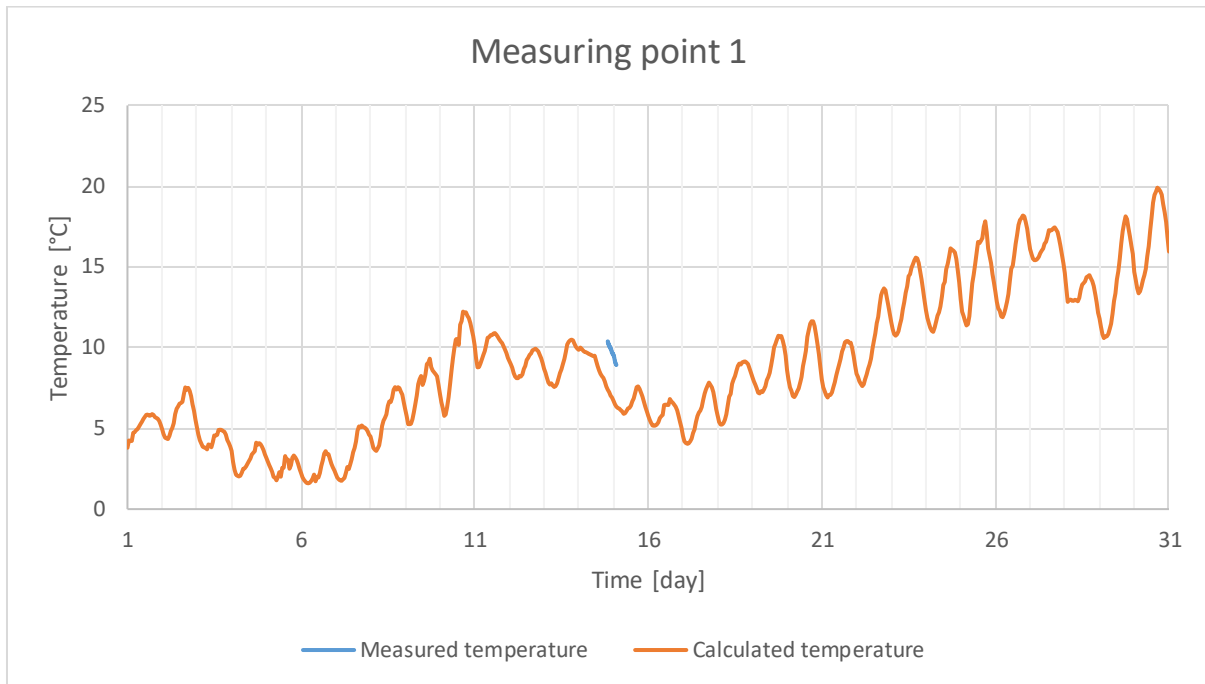


Figure 22. An overview of the temperature variation for measuring point 1 during the month of June. The observed data appears during June, 14th and June 15th.

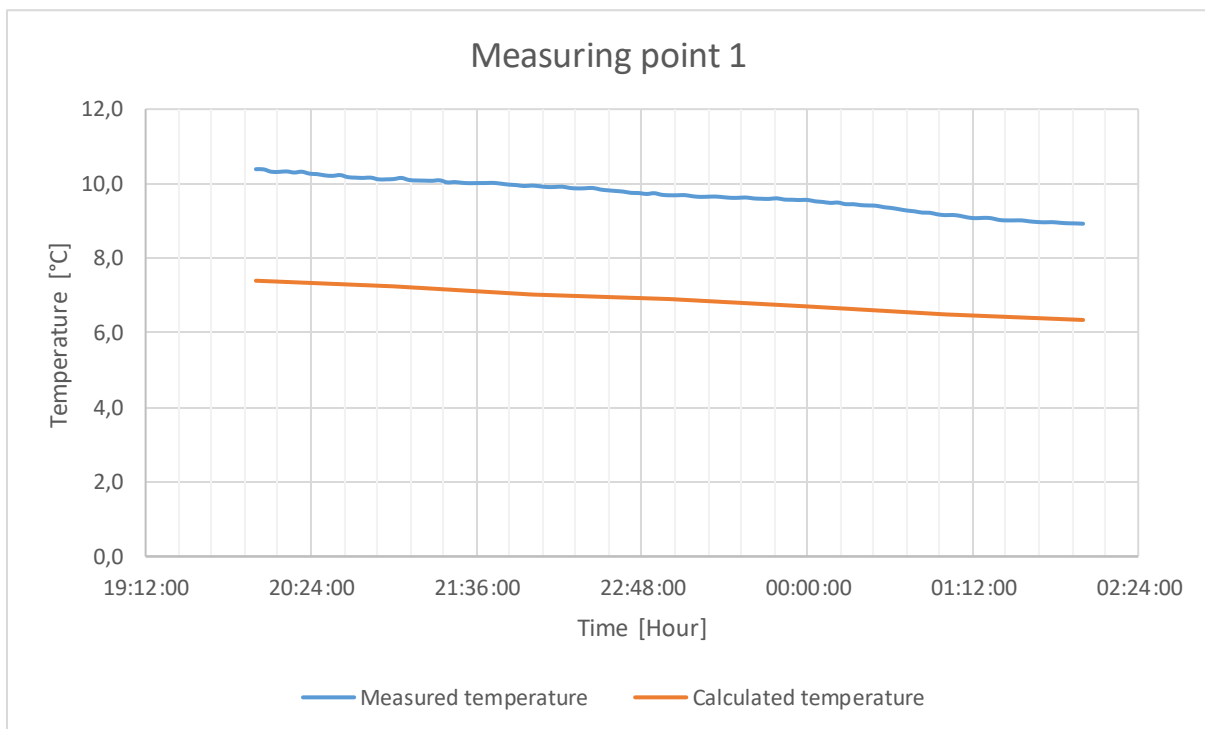


Figure 23. A comparison between the observed temperature and the calculated temperature for measuring point 1. As seen there are only six values to be compared.

Measuring point 8 can be found at the underside surface of the southern part of the bridge cross section.

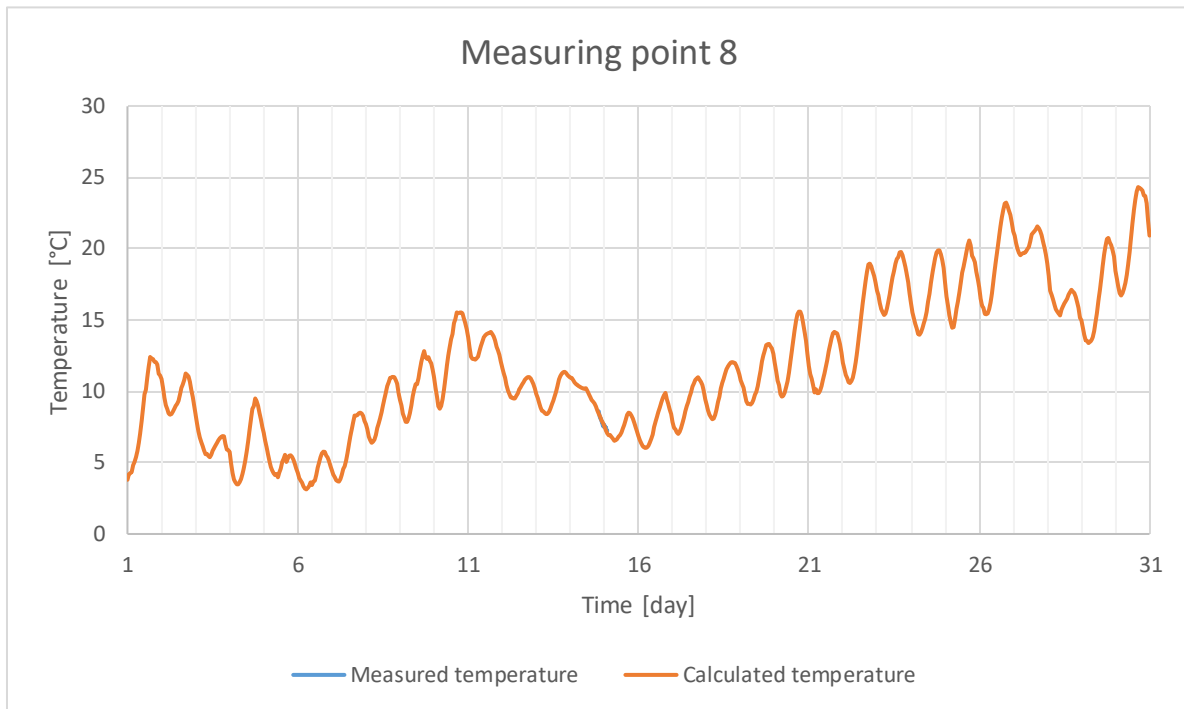


Figure 24. An overview of the temperature variation for measuring point 8 during the month of June. The observed data appears during June, 14th and June 15th.

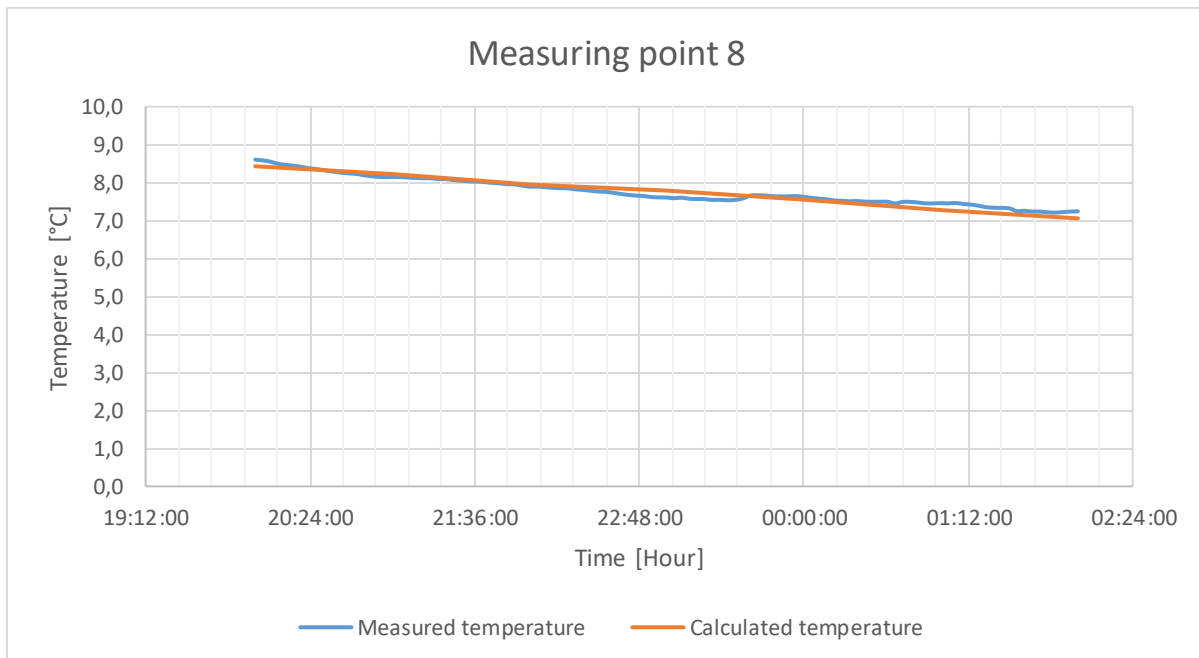


Figure 25. A comparison of the observed temperature and the calculated temperature for measuring point 8. There are only six values to be compared as seen.

4.7 Coefficient of determination

Summation of the residual coefficients for each point which a comparison between observed data and calculated data was made. The results for June, 2009, and August, 2010, are shown in table 4 below. A coefficient of determination for 2014 could not be calculated due to the lack of more measuring values. The similarity between the temperature estimation made with Abaqus 6.14 and the observed data from the monitoring temperature-gauges are shown by the coefficient of determination.

Table 4. Coefficient of determination for the graphs of measuring points TSÖ, TMÖ and TNÖ. The values indicate that the model is very good at describing the temperature variation.

Year	Coefficient of determination, R^2	
	Point	Value
2009	TSÖ	0.860
	TMÖ	0.970
	TNÖ	0.950
2010	TSÖ	0.837
	TMÖ	0.940
	TNÖ	0.912
2014	-	-

Since the coefficient of determination, R^2 , is close to 1 for every measuring point, a close similarity exists between the modeled temperature and the measured temperature.

4.8 Temperature variation further into the structure

During 2009 and 2010 the curves of the calculated temperature have larger amplitudes than the curves of the measured temperature. In other words the daily temperature variation is larger when it is calculated than in reality. An assumption was made that the gauges are located 40 millimeters into the structure, but it is possible that in reality the gauges are placed further into the structure where the amplitudes should be smaller due to the structure's thermal inertia. Therefore it is of interest to see how the calculated amplitudes change further into the structure.

The amplitudes have been analysed at five positions according to the figure below. The first position at 40 millimeters depth from the surface corresponds to measuring point TSÖ at the southern girder. The five positions have a distance of 40mm between them, except from the measuring point in the middle which has a distance of 45 millimeters according to figure 26.

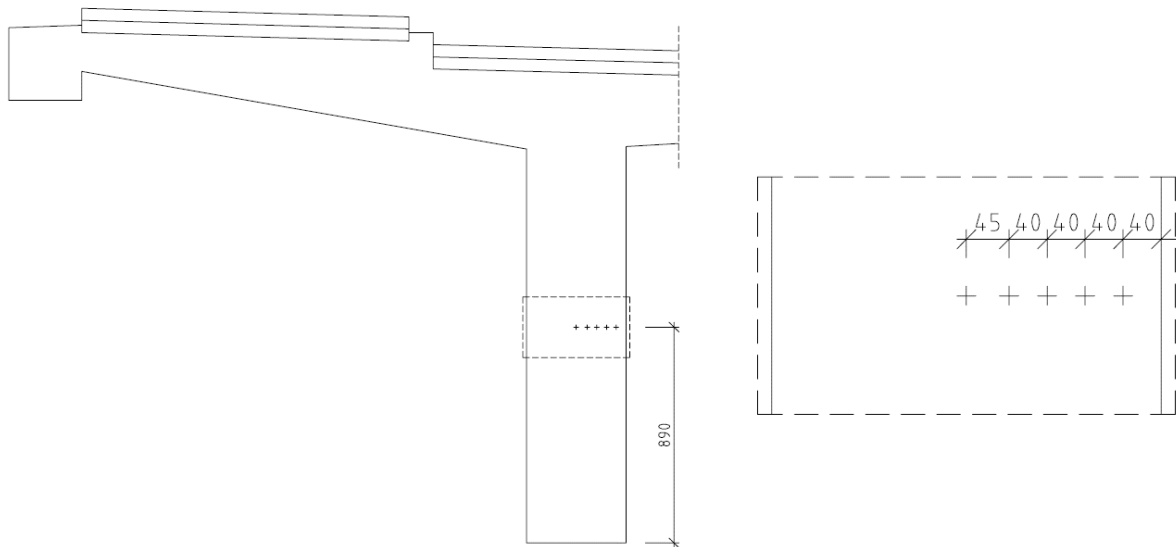


Figure 26. The temperature varies with the depth of the structure. The figure shows five different locations where analysis has been made, placed 890mm from the bottom of the girder. The distance between each point is 40mm except from the point located in the middle of the southern girder which is located with a distance of 45mm from the previous point.

4.8.1 Results

As expected the results for the five measuring points show that the amplitude of the temperature variation varies less than the amplitude of the measuring point closest to the surface. The results for the first five days of June 2009 and August 2010 can be seen in below. The temperature variation for the rest of June 2009 and August 2010 can be found in Appendix 10.2. The results show that the temperature from the model is not that affected by the depth compared to other assumptions concerning material properties.

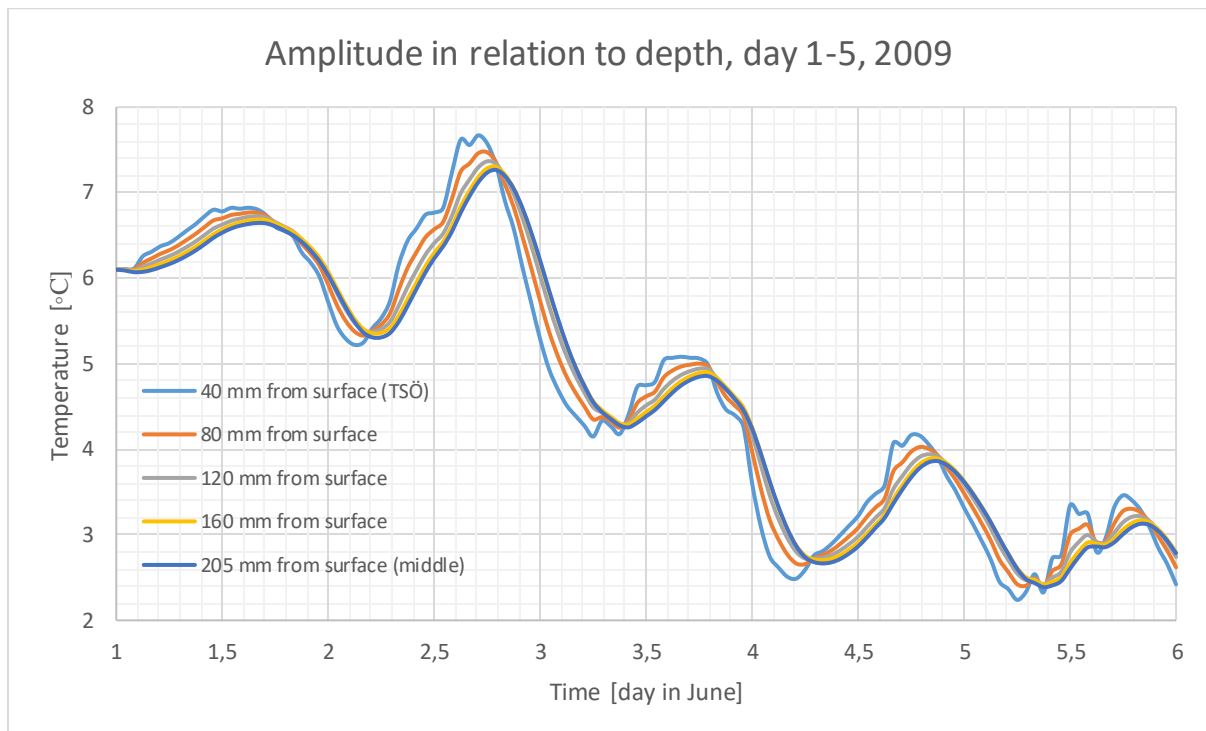


Figure 27. The temperature variation for each point during the time period of the 1st to the 5th of June, 2009.

Charts for the measurements of the whole month is found in Appendix 10.2.

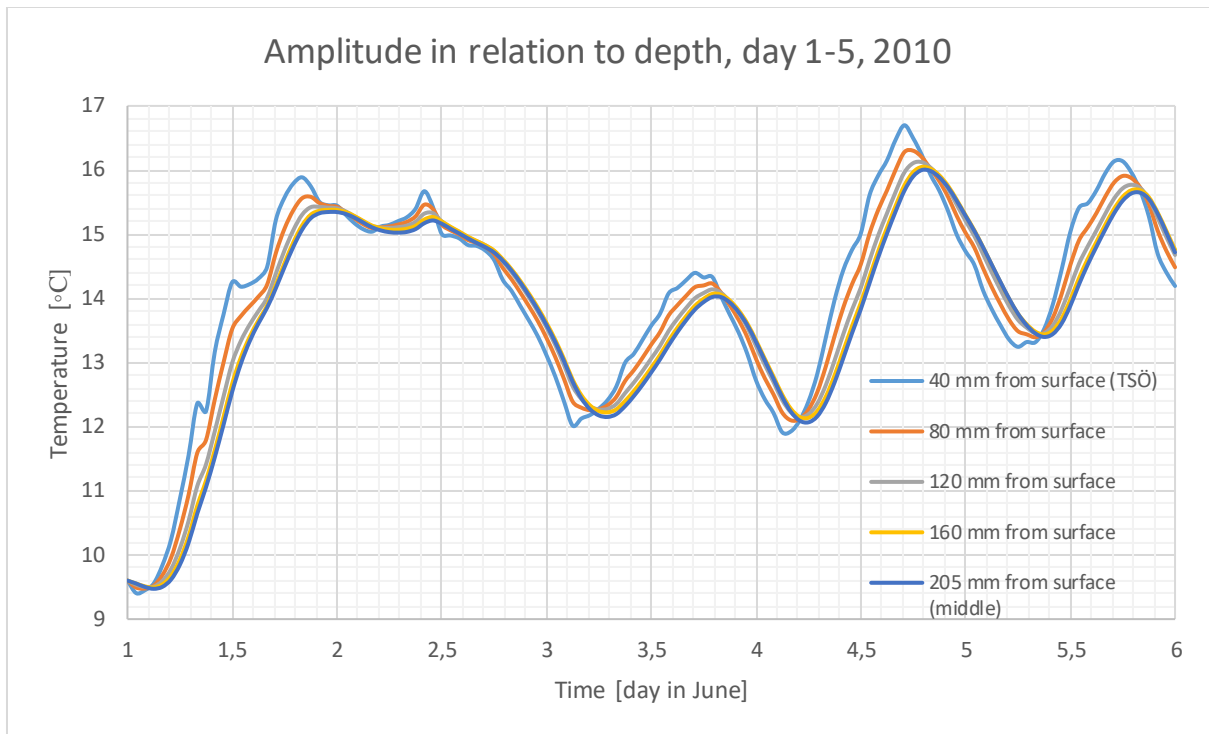


Figure 28. The temperature variation for the five different points during the time period of the 1st to the 5th August, 2010.

Graphs of the measurements of the whole month are found in Appendix 10.2.

5 Strain simulation in two dimensions

For the two dimensional simulation measuring points St12Sb1 and St12Nb have been studied. The measured strain goes in the z-direction which is the longitudinal direction of the bridge. However, this two-dimensional model gives the strain in the x- and y-direction. When calculating the strains using a two-dimensional model the element type CPS4R was used, which is a 4-node bilinear plane stress quadrilateral element. The element size used in this simulation was 20 millimeters.

5.1 Boundary conditions for two dimensions

Boundary conditions were applied when calculating the strain with the two dimensional model and the three dimensional model. The x-, -y- and z-directions used in Abaqus are seen at the right upper corner in figure 29. The north direction is also indicated in the figure, pointing in the same direction as the x-axis. Perpendicular to the x-axis, in the same plane, is the y-axis. For the two-dimensional case the bottom side of the southern girder is prevented from movements in the x- and y-direction. The bottom side of the mid girder and the northern girder are prevented from moving in the y-direction.

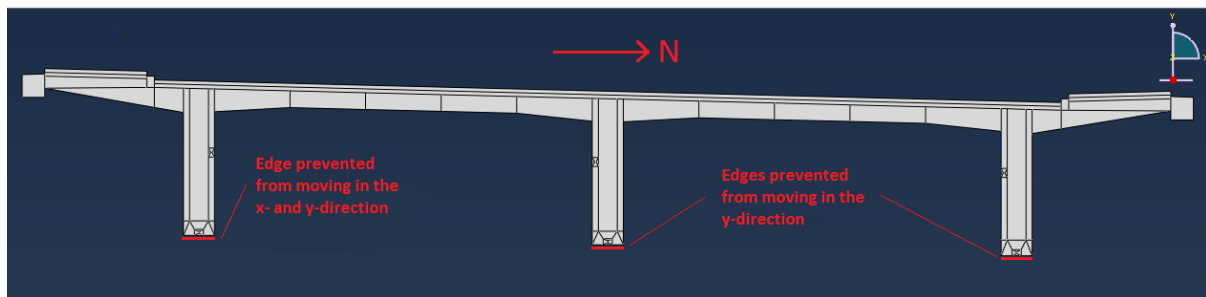


Figure 29. The boundary conditions used in the two dimensional strain model. The figure show an image of the model from Abaqus.

5.2 Results

5.2.1 Measuring point St12Sb1

Figure 30 shows the strain results for the calculated strain in the x-direction at measuring point St12Sb1 compared to the measured strain in the z-direction. The results show a similar behaviour during almost the whole time frame for both strain curves. The fact that the

measuring point lies close to a boundary condition might be a reason for the calculated strain to be restrained. The results show a quite good similarity between the calculated and measured strain curves.

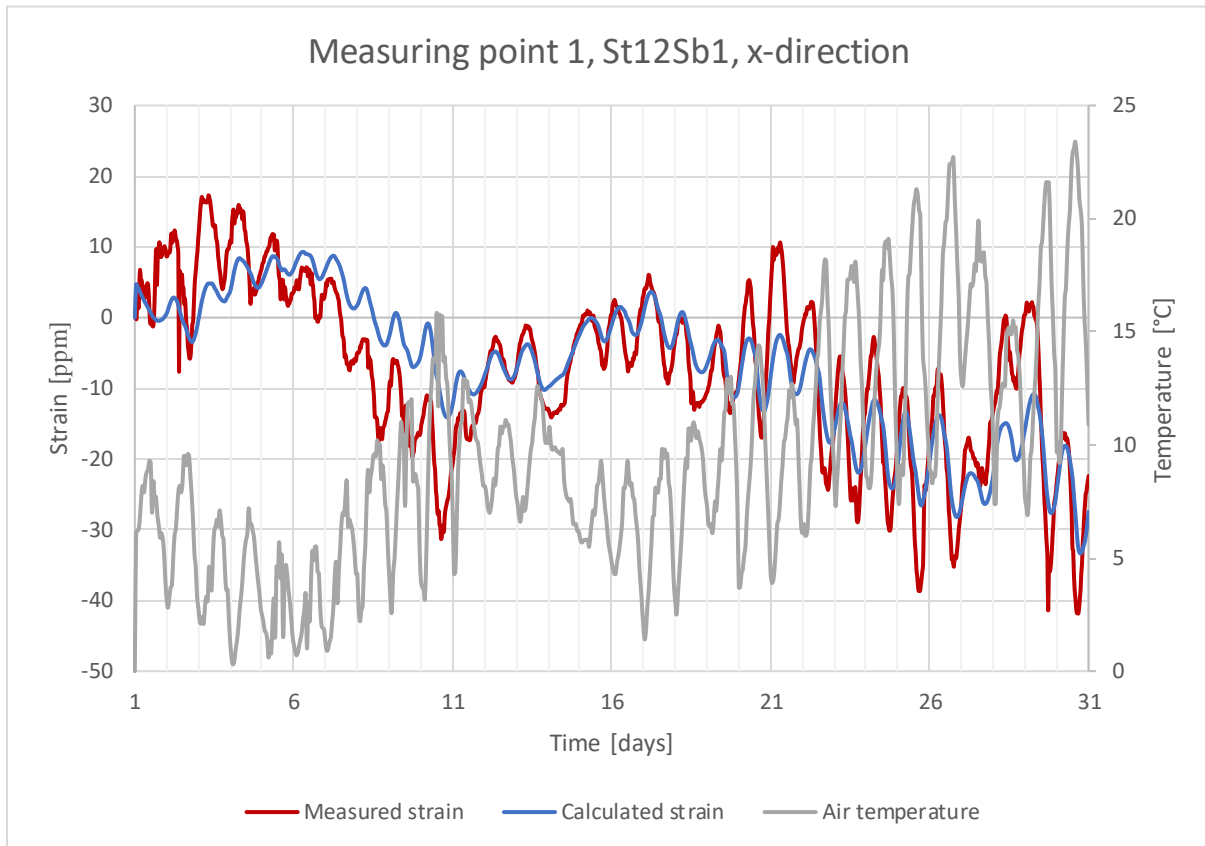


Figure 30. The measured strain in the z-direction is compared to the calculated strain in the x-direction for measuring point St12Sb1.

The amplitudes of the calculated strain curve seem to vary between about 5-20 parts per million while the amplitudes of the measured strain vary between approximately 10-40 parts per million.

Figure 31 shows the strain results for the comparison between the calculated strain in the y-direction and the measured strain in the z-direction. The calculated strain curve and the measured strain curve do not follow each other very well. Also, the amplitudes are much larger for the calculated strain than for the measured strain. Compared to the comparison between the z-direction and the x-direction in figure 30, the results correspond poorly.

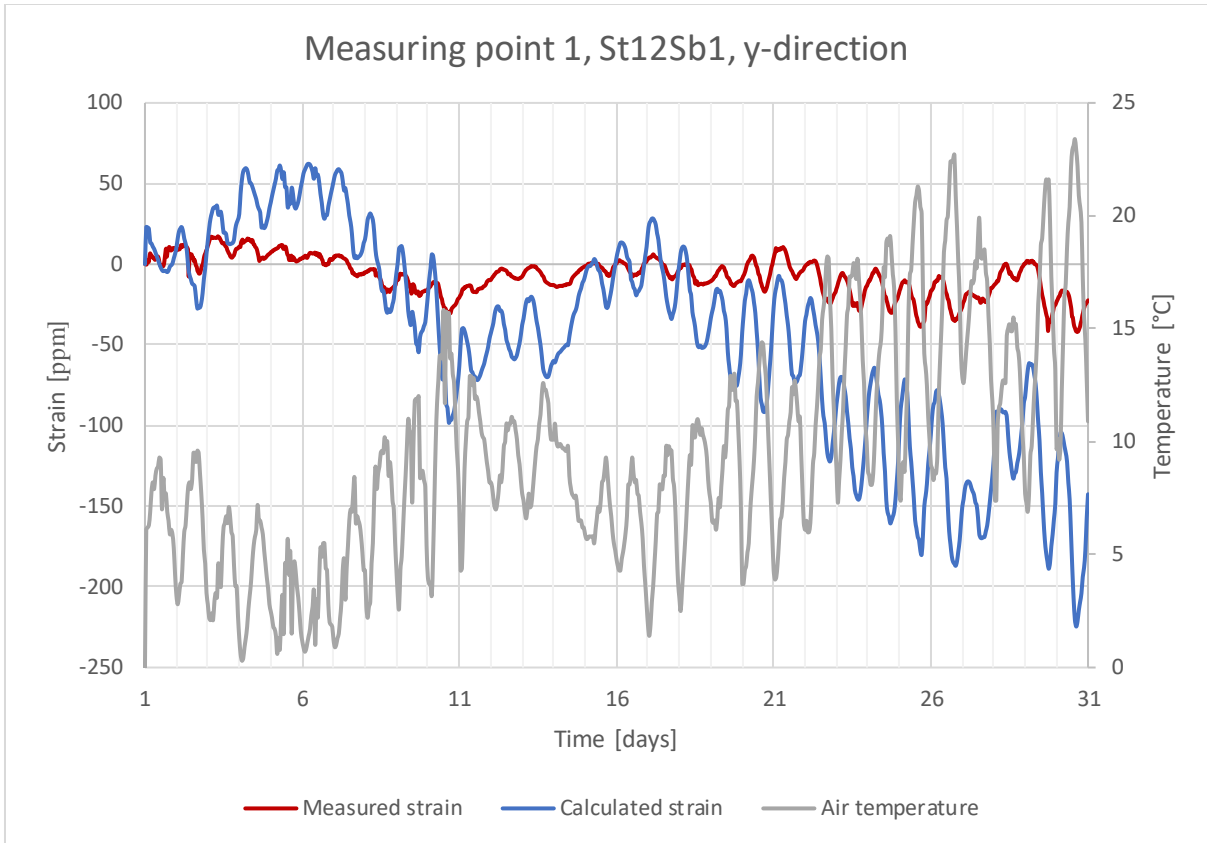


Figure 31. The measured strain in the z-direction is compared to the calculated strain in the y-direction for measuring point St12Sb1.

Amplitudes vary between about 10-40 parts per million for the measured strain and approximately between 20-125 parts per million for the calculated strain.

5.2.2 Measuring point St12Nb

For the measuring point, St12Nb, the calculated strain seems to be delayed in its response to the thermal action affecting the northern girder. The strain curves vary with approximately the same amplitude size during the whole time frame. But the curves do not follow each other very well.

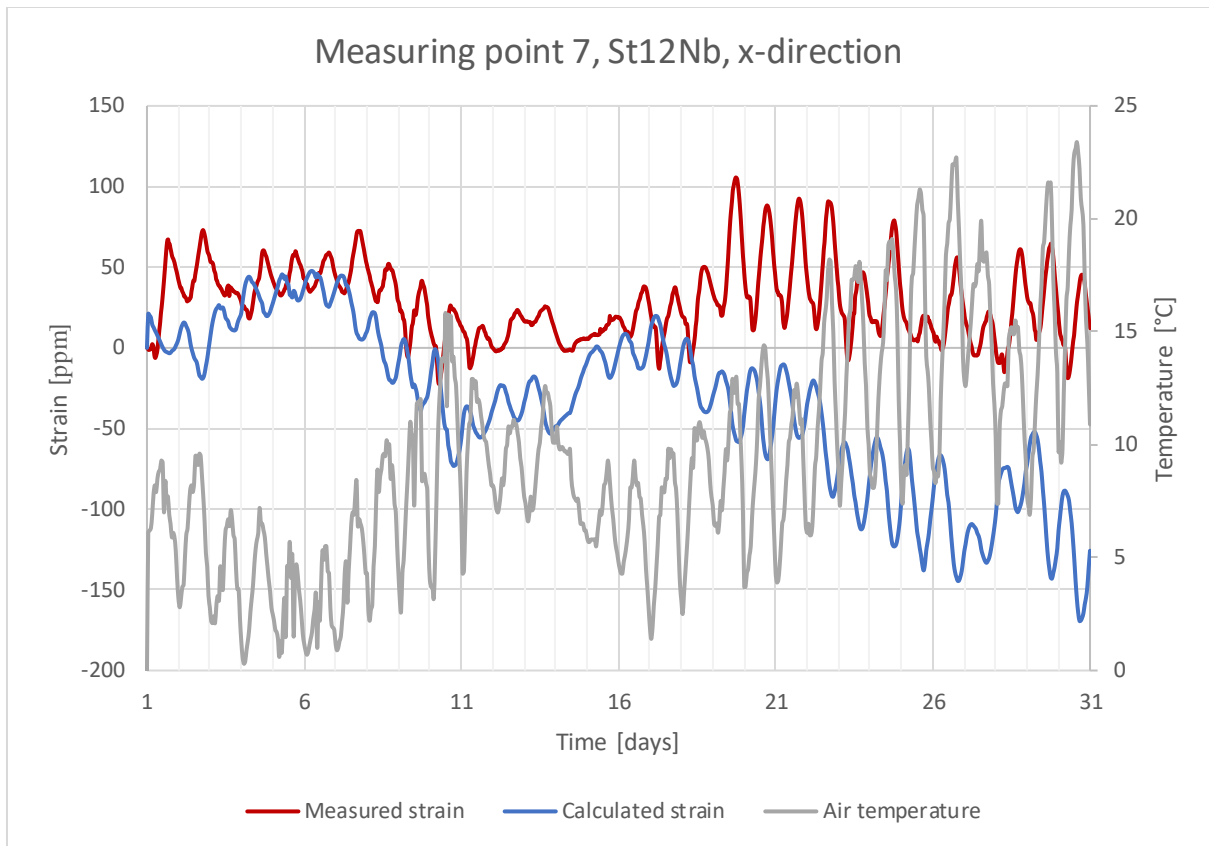


Figure 32. The measured strain in the z-direction is compared to the calculated strain in the x-direction for measuring point St12Nb.

The amplitudes of the calculated strain curve seem to vary between 20-100 parts per million while the amplitudes for the measured strain vary between approximately 0-100 parts per million.

The calculated strain in the y-direction is similar to the calculated strain in the x-direction.

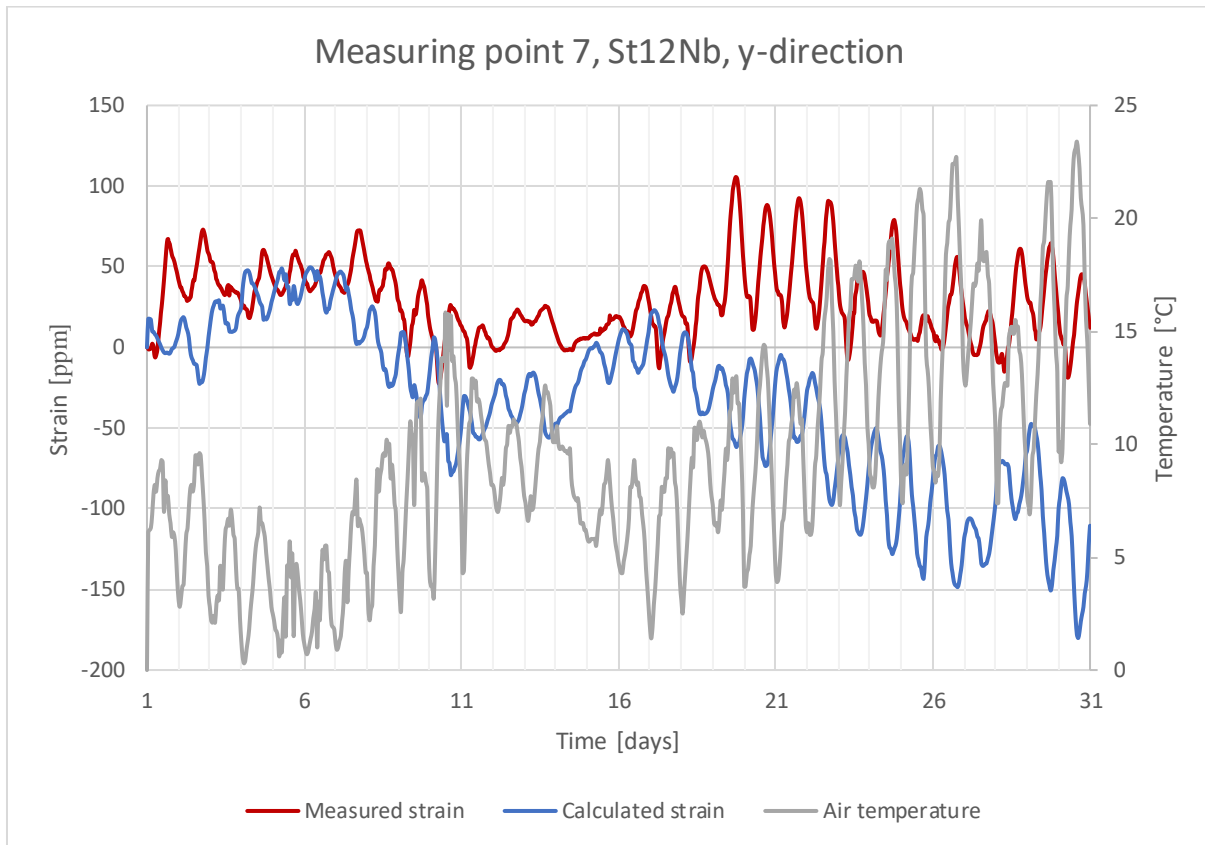


Figure 33. The measured strain in the z-direction is compared to the calculated strain in the y-direction for measuring point St12Nb.

Amplitudes vary between about 0-100 parts per million for the measured strain and approximately between 20-100 parts per million for the calculated strain.

6 Strain simulation in three dimensions

The mesh element used for three dimensional strain simulation is C3D8R, which is an 8-node linear brick element. This element type is suitable for three dimensional strain calculations. The mesh has been performed in a way so that the nodes in the model are placed as close to the real location as possible. This way the strain can easily be extracted from interesting nodes. Below, in figure 34, is an example of a mesh used. The element size is 0.2 meters. Smaller elements could not be used due to computer limitations.

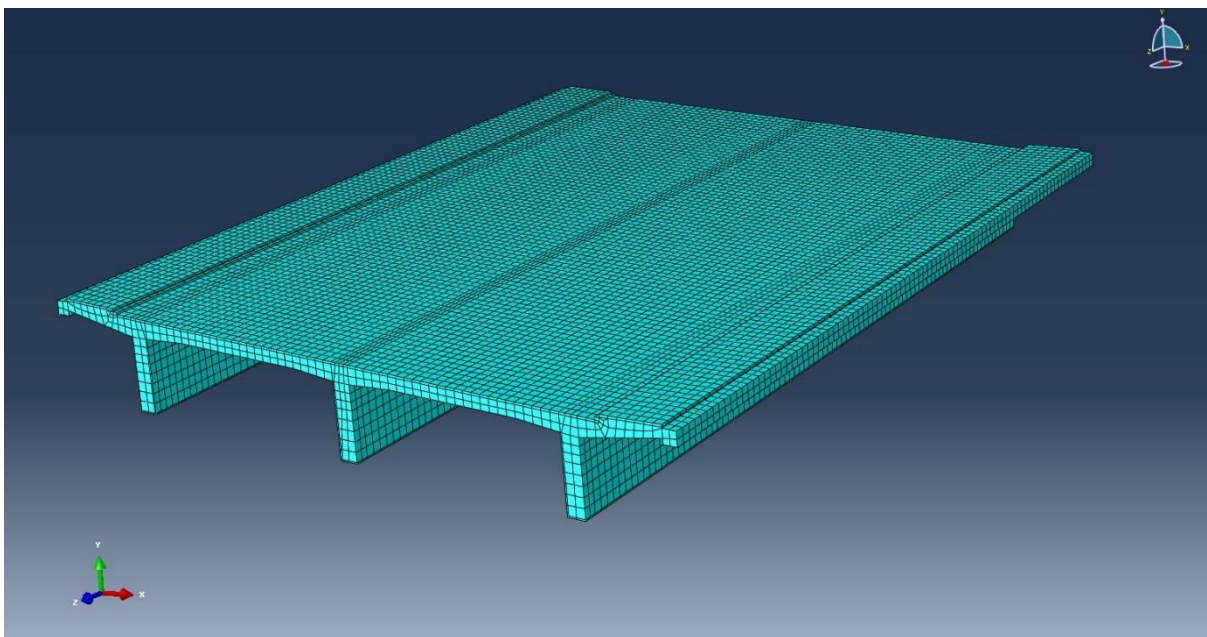


Figure 34. A three dimensional model with heat transfer elements was made to simulate the temperature in the first 18 meters of the bridge seen from the west side.

The temperature results on the three dimensional model were used as input data to simulate the strain.

6.1 Boundary conditions for three dimensions

For the three dimensional case the model is assumed to be unable to move in x -, y - and z -direction along the three longitudinal girder edges at the west side, where the western abutment is. This is meant to simulate the bearings there. At the eastern part of the model, at the three supporting columns, the bridge is cut. The whole cross section is assumed unable to move in the z -direction and also unable to rotate around the x -, and y -axis along the whole cross section surface.

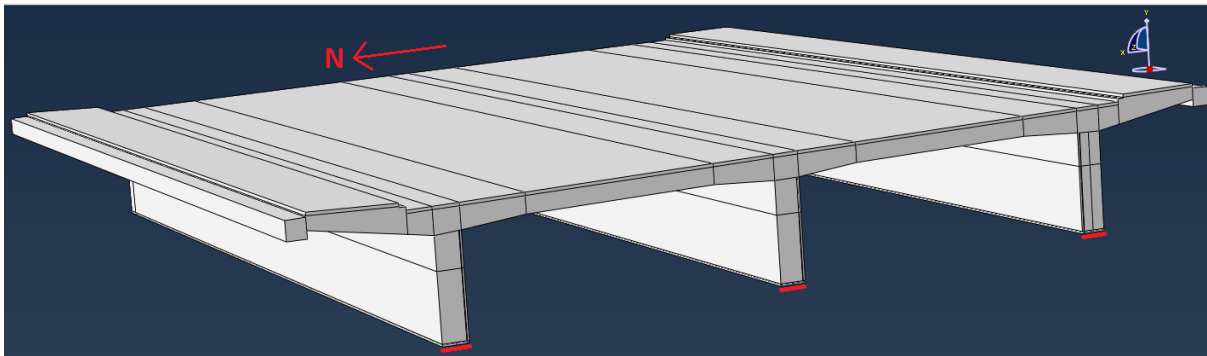


Figure 35. The boundary conditions for the western part of the bridge are marked with red lines at the edges of the longitudinal girders. The lines can't move in the x -, y - and z -direction but can rotate freely.

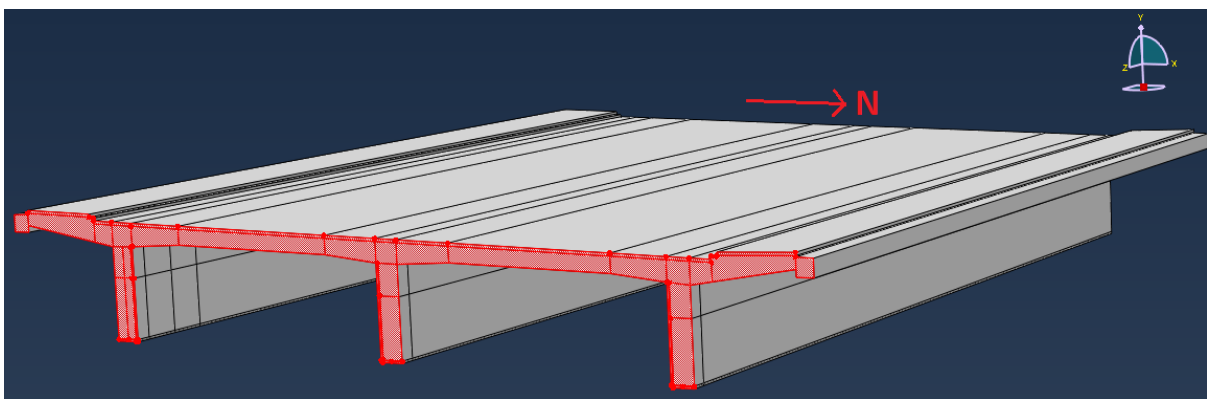


Figure 36. The boundary conditions for the eastern part of the bridge is for the cross section marked red in the figure. The cross section cannot move in the z -direction and cannot rotate around the x - and y -axis.

6.2 Results

The following results are for the eight measuring points with locations described in Chapter 3.5.2. The results from each of these measuring points will be presented in the following subchapters. The results are for the month of June the year of 2009.

There are 721 values for each measuring point, which corresponds to the number of hours in the month of June with a start value included. To make it easy to overview, the results are only presented graphically in the form of diagrams. The diagrams include the measured strain, the strain calculated with Abaqus, and the air temperature. The reason for including the air temperature is to get a picture of how the strain is related to the air temperature.

An example of what the strain distribution due to temperature can look like is illustrated in the two figures below. Each of the colors describe a strain interval. The blue color describes the most largest negative strain and the red color describes the largest positive strain.

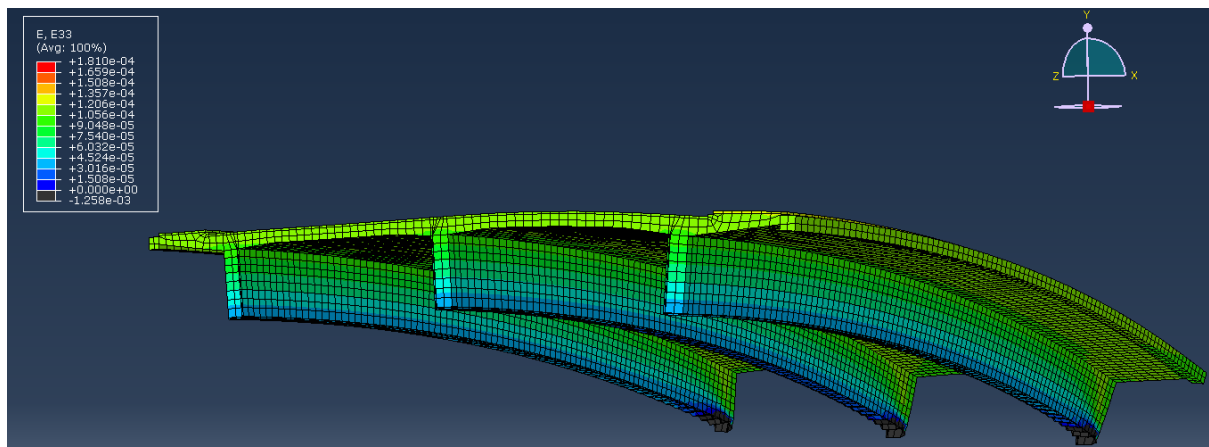


Figure 37. The three-dimensional strain distribution seen from the northeast in the finite element model. The red area shows the largest positive strain and the black area shows where the strain is negative. The strains are highly overscaled in this figure.

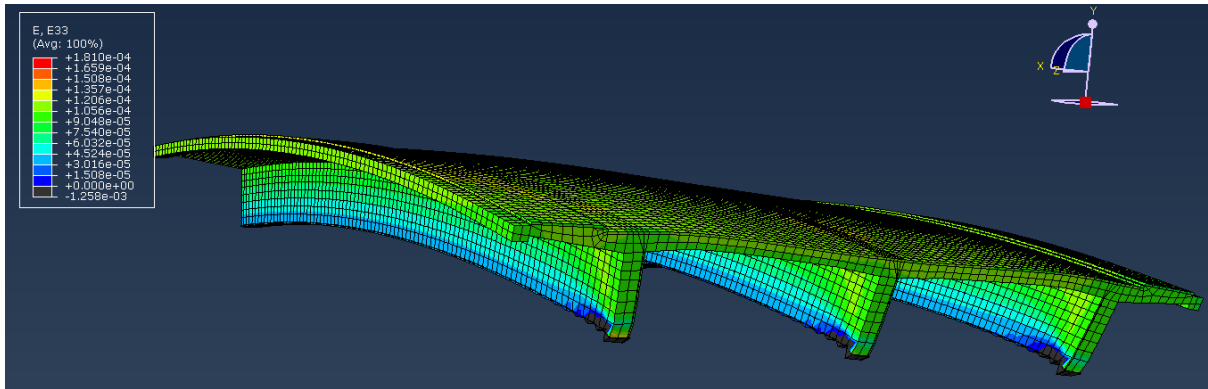


Figure 38. The three-dimensional strain distribution shown from the northwest in the finite element model. As in the previous figure the red area shows the largest positive strain and the black area shows where the strain is negative.

The measured strain contains contributions from both the traffic and temperature loads and the calculated strain contains only the strain from temperature loads. Even so, the calculated strain is mostly larger than the measured strain. This result is not logical. Thus it is hard to capture the size of the strain variations. This said, the model still captures the strain variations well.

6.2.1 Measuring point 1 - southern girder

The results for measuring point 1, located at the bottom of the southern girder, show that the calculated strain curve overall lies beneath the measured strain curve. The calculated strain goes from 0 parts per million in the start of June to about -40 parts per million in the end of June. The measured strain goes from 0 parts per million at the start of June to approximately -35 parts per million at the end of June.

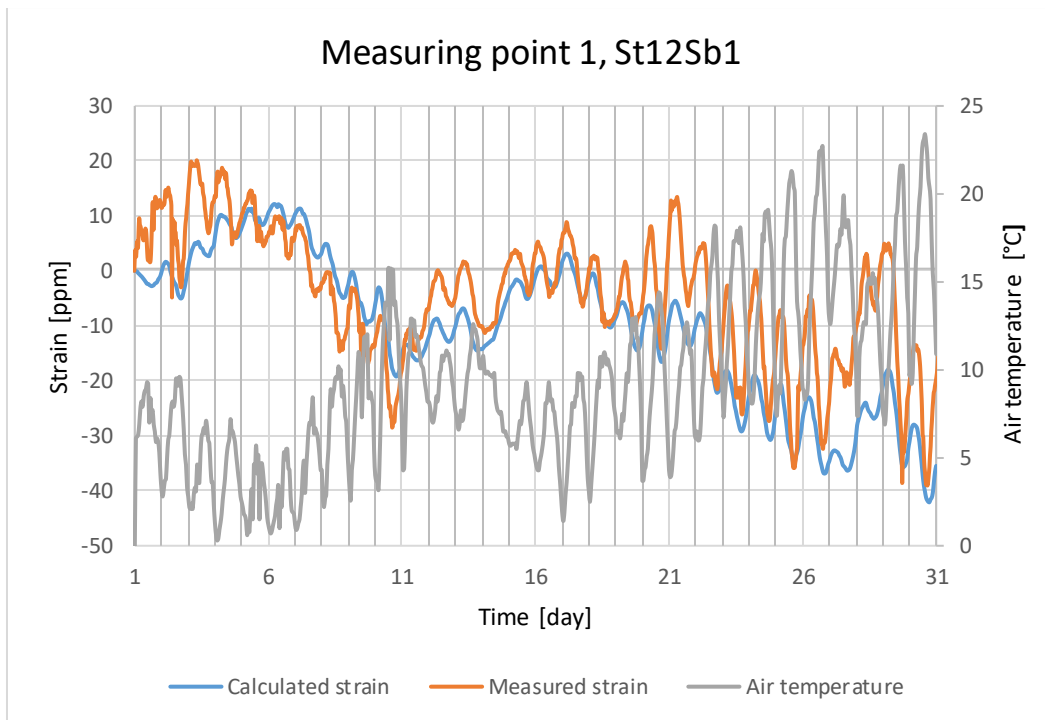


Figure 39. The results for measuring point 1. The diagram shows the strain calculated with Abaqus, the measured strain and the air temperature.

The appearance of the calculated strain curve and the measured strain curve are similar to each other. But there is a difference in the daily variation. The amplitude of the calculated strain curve is about 5-10 parts per million while it is 10-30 parts per million for the measured strain.

6.2.2 Measuring point 2 - southern girder

Measuring point 2 is located at the bottom of the southern girder. The results show that the calculated strain curve varies a little bit less than the measured strain curve and also lies somewhat lower than the measured strain curve. The calculated strain starts at 0 parts per million at the beginning of June and ends at approximately -35 parts per million. The measured strain starts at 0 parts per million in the beginning of June and ends at about -35 parts per million at the end of June.

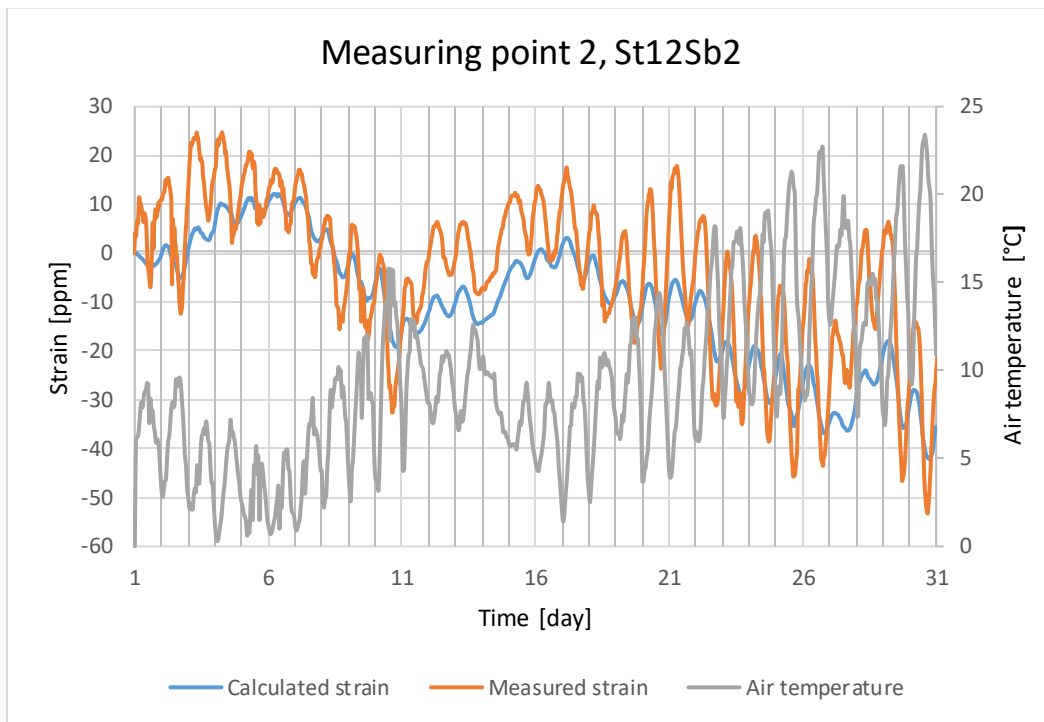


Figure 40. The results for measuring point 2. The diagram shows the strain calculated with Abaqus, the measured strain and the air temperature.

The calculated strain and the measured strain for measuring point 2, St12Sb2, is similar in behavior. At the beginning of June, the temperature is much lower than at the end of June. This should result in tensile elongation that increase during the period. As seen in the graph the air temperature, the calculated strain and the measured strain correspond to this theory but since the measured strain include both thermal actions and traffic, the measured strain should be equal to or less than the calculated strain. The amplitude of the calculated strain curve varies between approximately 5-10 parts per million and the amplitude of the measured strain curve varies between approximately 10-50 parts per million.

6.2.3 Measuring point 3 - southern girder

The results for measuring point 3, located at the bottom of the southern girder, show that the calculated strain curve varies a little bit less than the measured strain curve but also follows the measured strain curve during the whole month. In general, measuring point 2 and 3 are similar for both the measured strain and the calculated strain. Like measuring point 2, measuring point 3 starts and ends at the same strain values both for the measured strain and for the calculated strain.

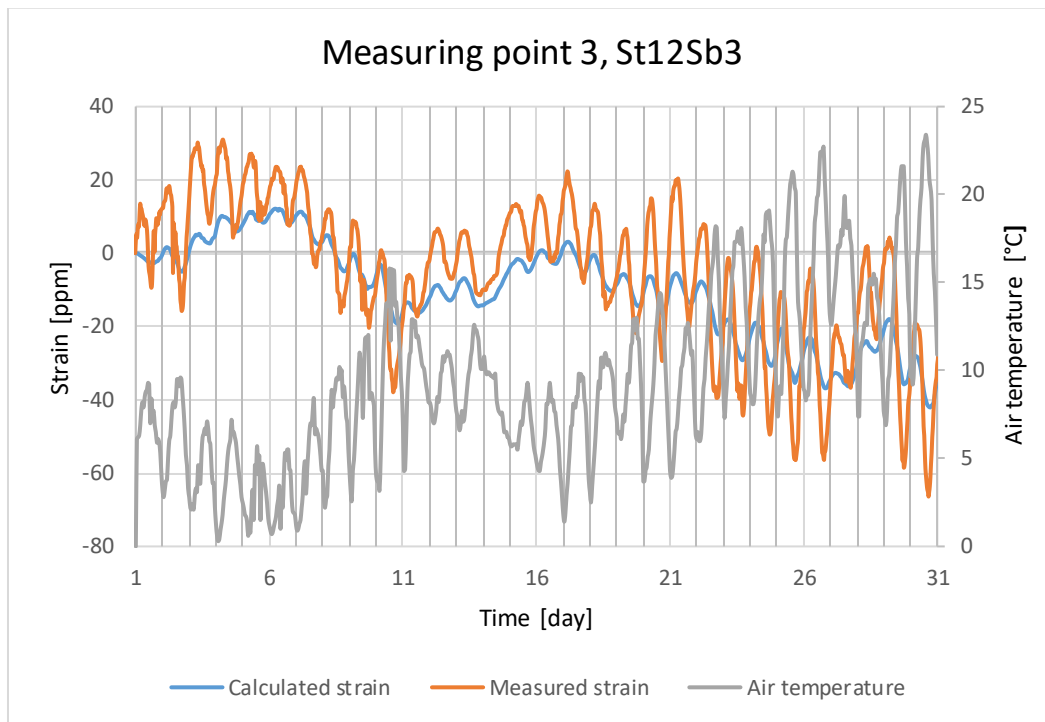


Figure 41. The results for measuring point 3. The diagram shows the strain calculated with Abaqus, the measured strain and the air temperature.

The amplitude of the calculated strain curve varies between approximately 0-10 parts per million and the amplitude of the measured strain curve varies between approximately 0-50 parts per million. The behavior is the same as for measuring point 2. Thus, the measured strain curve should give a tensile elongation which is equal to or less than the measured curve but instead the results show that the calculated strain curve gives greater tensile elongation than the measured strain curve.

6.2.4 Measuring point 4 - southern girder

Measuring point 4 is located at the upper part of the southern girder. The calculated strain curve lies at about the same level as the measured strain curve the first 8 days. The rest of the month the calculated strain curve lies, in general, beneath the measured strain curve. The calculated strain goes from 0 parts per million at the start of June to about -90 parts per million at the end of June. The measured strain on the other hand is pendling up and down around 0 parts per million. The largest amplitude, approximately 60-70 parts per million, occurs between the 19th and the 30th of June.

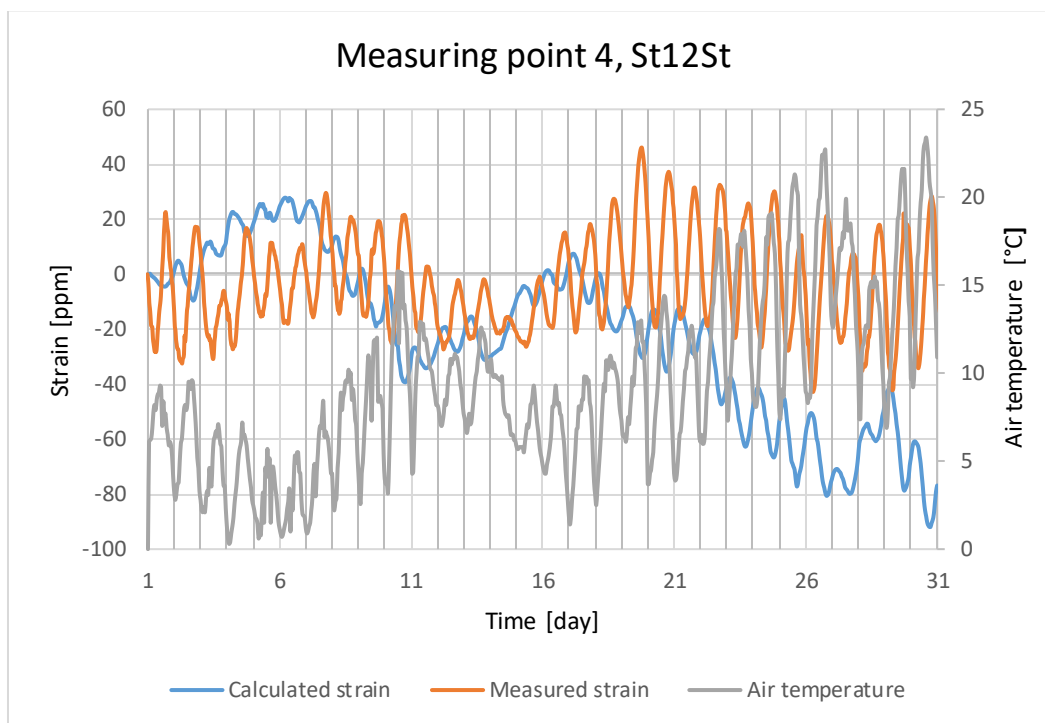


Figure 42. The results for measuring point 4. The diagram shows the strain calculated with Abaqus, the measured strain and the air temperature.

The calculated strain curve and the measured strain curve are not very similar in behaviour. The amplitude of the calculated strain curve is about 10-30 parts per million. The amplitude of the measured strain curve is about 20-70 parts per million which is considerably bigger.

6.2.5 Measuring point 5 - mid girder

The results for measuring point 5, located at the bottom of the mid girder, show that the calculated strain curve lies beneath the measured strain curve the first seven days of the month. In the middle of the month, between the 7th and the 15th of June, the the calculated strain lies above the measured strain. At the last part of the month, during June 15th and June 30th the calculated strain curve lies beneath the measured strain curve in general.

The calculated strain goes from 0 parts per million at the start of June to about 15 parts per million at the end of June. The measured strain goes from 0 parts per million at the beginning of June to about 20 parts of million in the end of June.

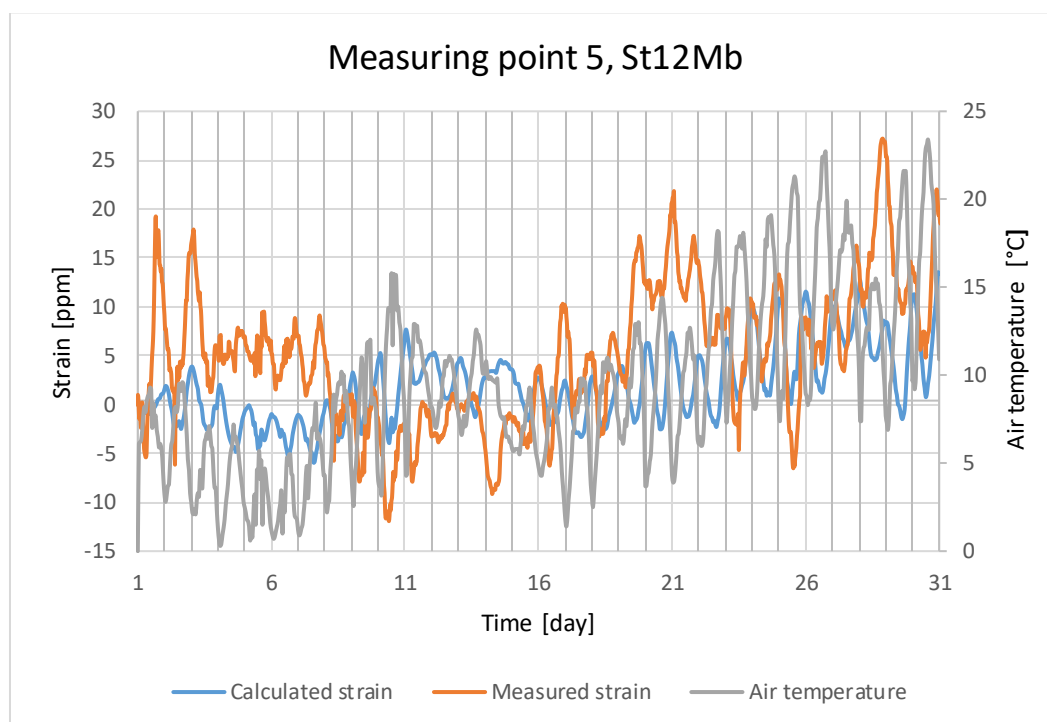


Figure 43. The results for measuring point 5. The diagram shows the strain calculated with Abaqus, the measured strain and the air temperature.

The amplitude of the calculated strain curve is about 5-15 parts per million. The amplitude of the measured strain curve is about 5-25 parts per million which is slightly larger.

Like for the previous measuring point it appears that the curves go in opposite directions during the whole time period. While the calculated strain curve is falling, the measured strain curve is rising and vice versa. The calculated strain curve might be delayed in its response to the temperature variation.

6.2.6 Measuring point 6 - mid girder

Measuring point 6 is located at the upper part of the mid girder. The calculated strain curve lies in general beneath the measured strain curve except between the 3rd and the 7th of June. The calculated strain varies according to the air temperature variation over the month. A rising temperature results in larger tensile elongation which can be seen in the graph. For the measured strain, the closeness to the air temperature seems to be a little bit smaller.

The calculated strain curve and the the measured strain curve follow each other fairly well. The calculated strain goes from 0 to -90 parts per million from the start to the the end of June while the measured strain goes from 0 to -20 parts per million during the same period.

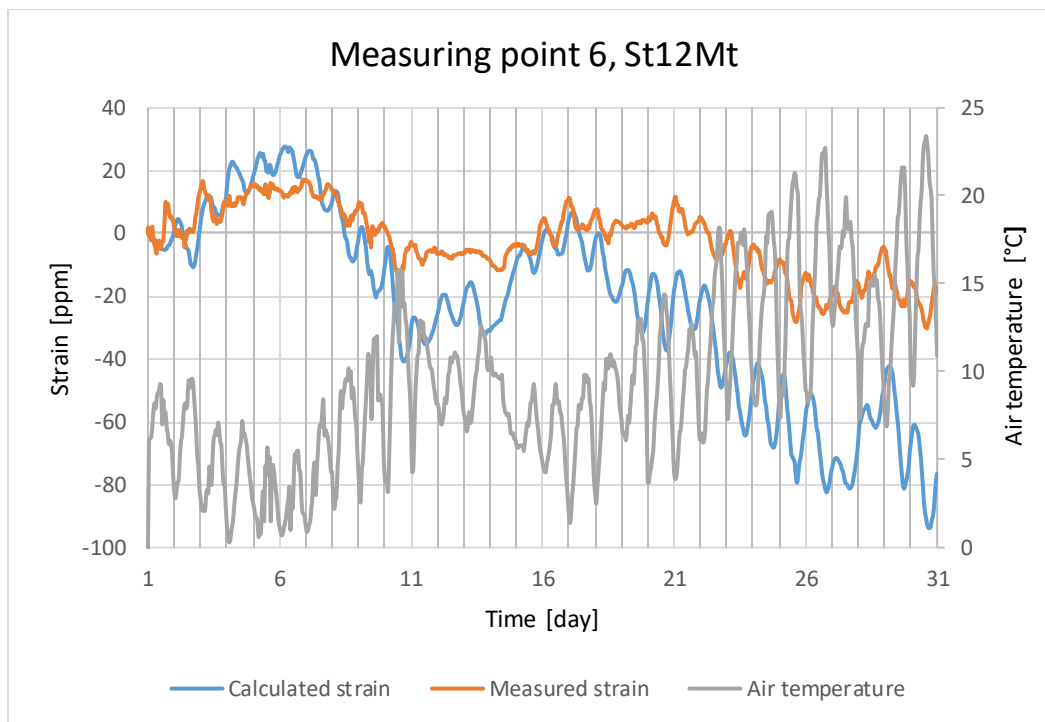


Figure 44. The results for measuring point 6. The diagram shows the strain calculated with Abaqus, the measured strain and the air temperature.

The amplitude of the calculated strain curve is about 5-25 parts per million. The amplitude of the measured strain curve is about 0-10 parts per million.

6.2.7 Measuring point 7 - northern girder

At the bottom of the northern girder, measuring point 7 can be found. The results for measuring point 7 show that the calculated strain curve lies beneath the measured strain curve for almost the entire month of June. The measured strain is pendling up and down around the value of 30 parts per million, revealing great change between tensile and compression strains. The calculated strain starts at 0 parts per million at the beginning of June and ends at about -20 parts per million at the end of June.

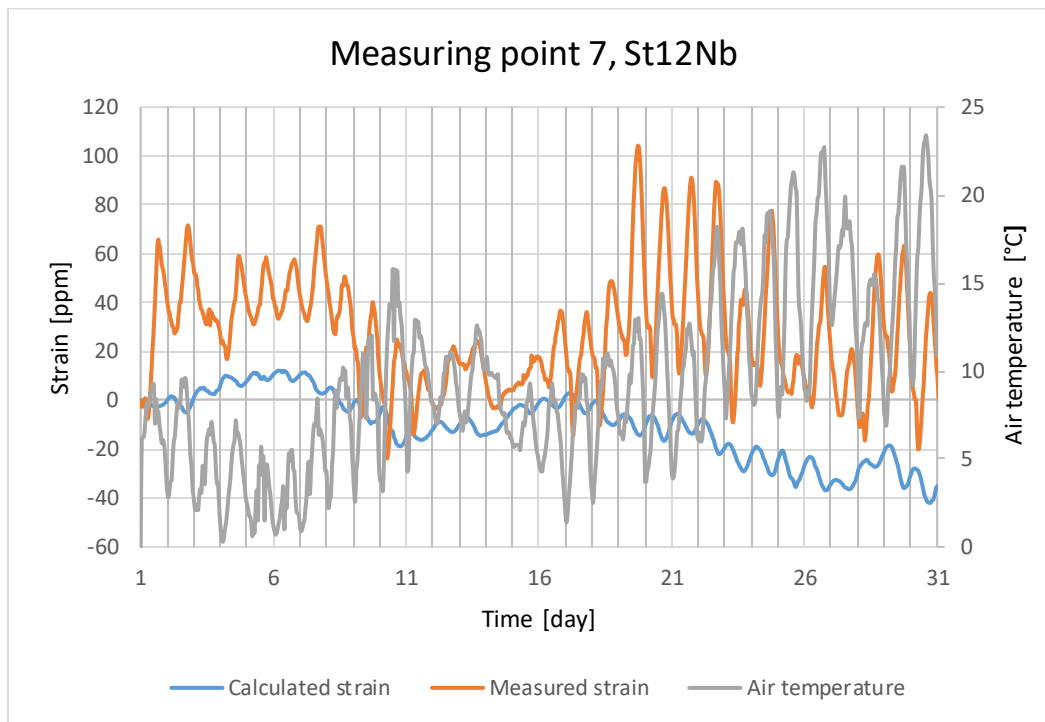


Figure 45. The results for measuring point 7. The diagram shows the strain calculated with Abaqus, the measured strain and the air temperature.

The calculated strain curve varies in the opposite direction to the measured strain curve. Questionable is if the calculated strain is delayed in its response to the thermal impact, if the model is wrong or if the measured data is wrong. If the calculated strain just would be delayed, the larger amplitudes of the measured strain might be explained by traffic.

The calculated strain curve has amplitudes of about 5-10 parts per million while the measured strain curve has amplitudes about 20-80 parts per million, thus being about 4-8 times bigger.

6.2.8 Measuring point 8 - northern girder

Measuring point 8 is located at the upper part of the northern girder. The measured strain curve has a falling tendency and goes from the value of 0 parts per million to -20 parts per million during June. The calculated strain declines from the value of 0 parts per million to -90 parts per million.

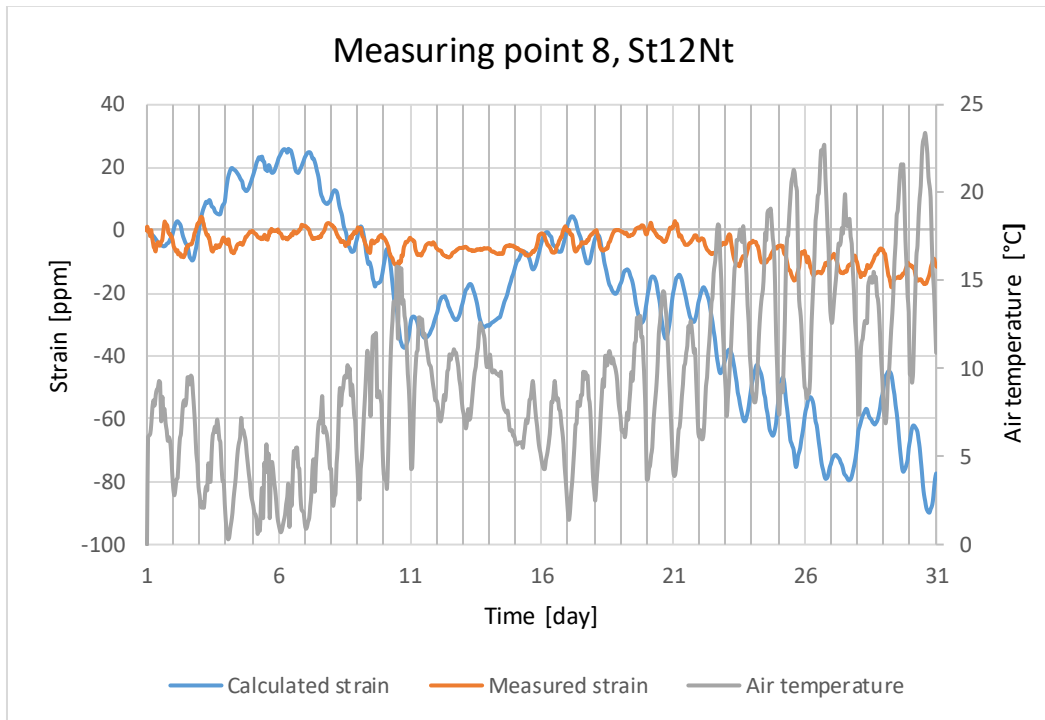


Figure 46. The results for measuring point 8. The diagram shows the strain calculated with Abaqus, the measured strain and the air temperature.

The calculated strain curve does not resemble the measured strain curve over all. The amplitudes of the calculated strain curve are roughly 10-20 parts per million while the amplitudes for the measured strain curve are about 5-10 parts per million.

7 Discussion

The results from the temperature simulations serve as a verification of the model created by Ph.D Oskar Larsson. The results from the strain simulations imply that it is somewhat difficult to create an accurate FE-model which is able to describe the strain variation and strain distribution.

A lot of factors might have influenced the results. For the three dimensional model several assumptions were made about the geometry. The three longitudinal girders have, in reality, another geometry than the one used in the model. The height is in fact smaller in the middle, between the supports.

The results are also dependent on the choice of material properties in the finite element models. Parameters such as modulus of elasticity, poisson's ratio, specific heat capacity, density and conductivity may affect the results.

Another factor of great importance is the choice of boundary conditions, especially in the area close to the supports where the measuring points were located. It is possible that the chosen boundary conditions neither are sufficient nor reliable.

Regarding the temperature model, it is fair to say that it is able to describe the temperature variation very well, not only in the nodes but probably in the entire cross section. This statement is based on the fact that the temperature has been controlled in totally 11 nodes in different parts of the bridge. All these nodes gave accurate results, therefore there is no reason to assume that the model would not be accurate between measuring points or around measuring points.

The results are highly affected by the climate input data. Should the input data be inaccurate the results would be inaccurate. The input data from the Swedish Meteorological and Hydrological Institute used in this study are considered reliable. Although, some of the input data can be received from existing databases such as wind speed and air temperature and some measurements must be made locally. In this case the direct radiation and the diffuse radiation were measured on site in Kiruna by Complab for the year of 2014. For the year of 2009 and 2010 the solar radiation data was obtained from the STRÅNG database, produced with support from the Swedish Radiation Protection Authority and the Swedish Environmental Agency.

The usefulness of the model thus depends on both the accuracy of the climate input data and of how easy it is to obtain this data. The results of the two dimensional temperature model mean that the model can be used further by other researchers to examine temperature variations in other concrete structures.

8 Conclusion

The two-dimensional temperature model is very accurate for the year of 2009 and 2010. The results from three measuring points in the bridge prove this. The use of an approximative method to calculate the outgoing long wave radiation seems to work well since the temperature results are very accurate. The model is also accurate for the year of 2014, according to the results from eight measuring points in the bridge. However, the measurements for 2014 only extend over a couple of hours which means that no conclusion can be drawn from the results of 2014 regarding the accuracy of the model.

The analysis of the temperature variation further into the structure shows that the temperature variation is almost the same in the middle of the southern girder as in measuring point TSÖ, 40 millimeters from the edge. Therefore it can be concluded that the larger amplitude of the calculated strain is caused by the model rather than an incorrect assumption of the location of measuring points.

The calculated strain from the two dimensional model does not seem to follow the measured strain at the northern girder in any direction. For the southern girder the calculated strain is very close to the measured strain in the x-direction. However, the reason for this is the boundary condition in the x-direction at the bottom of the southern girder.

For the three dimensional case, the strain curves vary about the same way for most of the measuring points. However the daily variation is much larger for most of the measured values compared to the calculated values. It seems that the strain model overestimates the strain, but underestimates the daily strain variation. Different boundary conditions have to be tested to see if there is any change, this was however out of scope for this thesis.

The conclusion is that this model works very well to simulate the temperature distribution, although an approximative method to calculate the outgoing long wave radiation was used. It seems though that the model is not able to describe the strain variations accurately.

9 References

- 1991-1-5, S.-E., 2003. *Eurocode 1: Actions on structures - Part 1-5: General actions - Thermal actions*. Stockholm: s.n.
- Barbero, E. J., 2008. *Finite Element Analysis of Composite Materials*. Boca Raton: Taylor & Francis Group.
- Burström, P.-G., 2007. *Byggnadsmaterial - Uppbyggnad, tillverkning och egenskaper*. 2nd ed. Lund: Specialtrykkeriet A/S.
- Cope, R. & Clark, L., 1984. *Concrete slabs - Analysis and design*. 1st ed. New York: ELSEVIER SCIENCE PUBLISHING CO., INC..
- Duffie, J. A. & Beckman, W. A., 2006. *Solar Engineering of Thermal Processes*. 3rd ed. Hoboken, New Jersey: John Wiley & Sons.
- Elfgren, L. et al., 2015. *Brottbelastning av en 55 år gammal spännbetongbro i Kiruna - Kalibrering av modeller för tillståndsbedömning*, s.l.: s.n.
- Elfgren, L., Emborg, M., Enochsson, O. & Sabourova, N., 2011. *Gruvvägsbron i Kiruna Deformationskapacitet*, s.l.: s.n.
- Emerson, M., 1973. *The Calculation of the Distribution of Temperature in Bridges*. 1st ed. Crowthorne: s.n.
- Goswami, D. Y., Kreith, F. & Kreider, J. F., 1999. *Principles of Solar Engineering*. 2 ed. Philadelphia: George H. Buchanan Co..
- Incropera, F. P., Dewitt, D. P., Bergman, T. L. & Lavine, A. S., 2007. *Fundamentals of Heat and Mass Transfer*. 6th ed. s.l.:s.n.
- Larsson, O., 2012. *Climate Related Thermal Actions for Reliable Design of Concrete Structures*, s.l.: s.n.
- Ljungskrantz, C., Möller, G. & Petersons, N., 1994. *Betonghandbok*. 2nd ed. Stockholm: Solna: AB Svensk Byggtjänst.
- M. Jiji, L., 2009. *Heat Conduction*. Third Edition ed. Chennai: Springer-Verlag Berlin Heidelberg.
- Mary, E., 1973. *The Calculation of the Distribution of Temperature in Bridges*. 1st ed. Crowthorne: s.n.
- McClellan, T. & Pedersen, C., 1997. *Investigation of Outside Heat Balance Models for Use in a Heat Balance Cooling Load Calculation*. Vol. 103, Part 2, pp. 469-484 ed. s.l.:ASHRAE Transactions.
- Menard, S., 2000. Coefficient of Determination for Multiple Logistic Regression Analysis. *The American Statistician*, Volume 54.
- Nevander, L. & Elmarsson, B., 2001. *Fukthandbok*. Stockholm: s.n.

- Neville, A., 1995. *Properties of Concrete*. 4th ed. Harlow, United Kingdom: Longman.
- Ottosen, N. S. & Petersson, H., 1992. *Introduction to the Finite Element Method*. Harlow: Prentice Hall.
- Pepper, D. W. & Heinrich, J. C., 2006. *The Finite Element Method - Basic Concepts and Applications*. 2nd ed. Boca Raton: Taylor & Francis Groups.
- Perez, R. & Seals, R., 1987. *A NEW SIMPLIFIED VERSION OF THE PEREZ DIFFUSE IRRADIANCE MODEL FOR TILTED SURFACES*, s.l.: Pergamon Journals Ltd..
- Wilby, C., 1983/1991. *Concrete Materials and Structures*. 1st ed. Cambridge: Cambridge University Press.
- Wood, J. & Potter, E., 2002. *Sunshine Sensor, type BF3*. s.l.:s.n.

10 Appendix

10.1 Temperature results for 2014

Measuring point 2 can be found at the girder on the northern side of the bridge cross section.

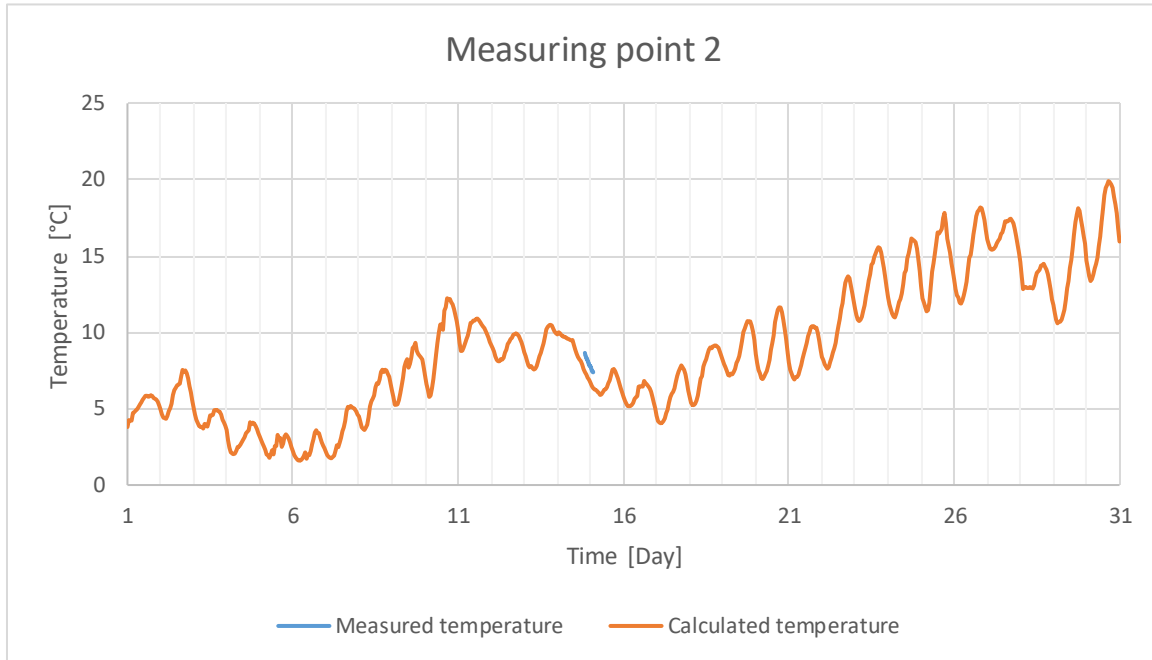


Figure 47. An overview of the temperature variation for measuring point 2 during the month of June. The observed data appears during June, 14th and June 15th.

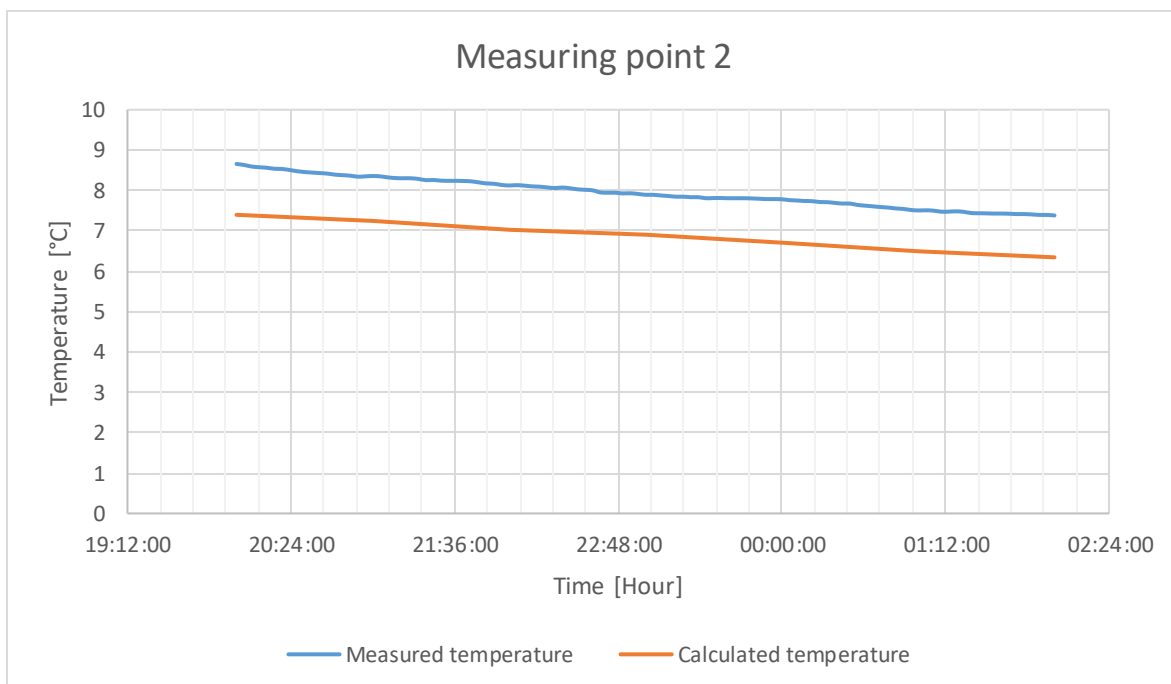


Figure 48. A comparison of the observed temperature and the calculated temperature for measuring point 2. There are only six values to be compared as seen.

Measuring point 3 can be found at the girder located in the middle of the bridge cross section.

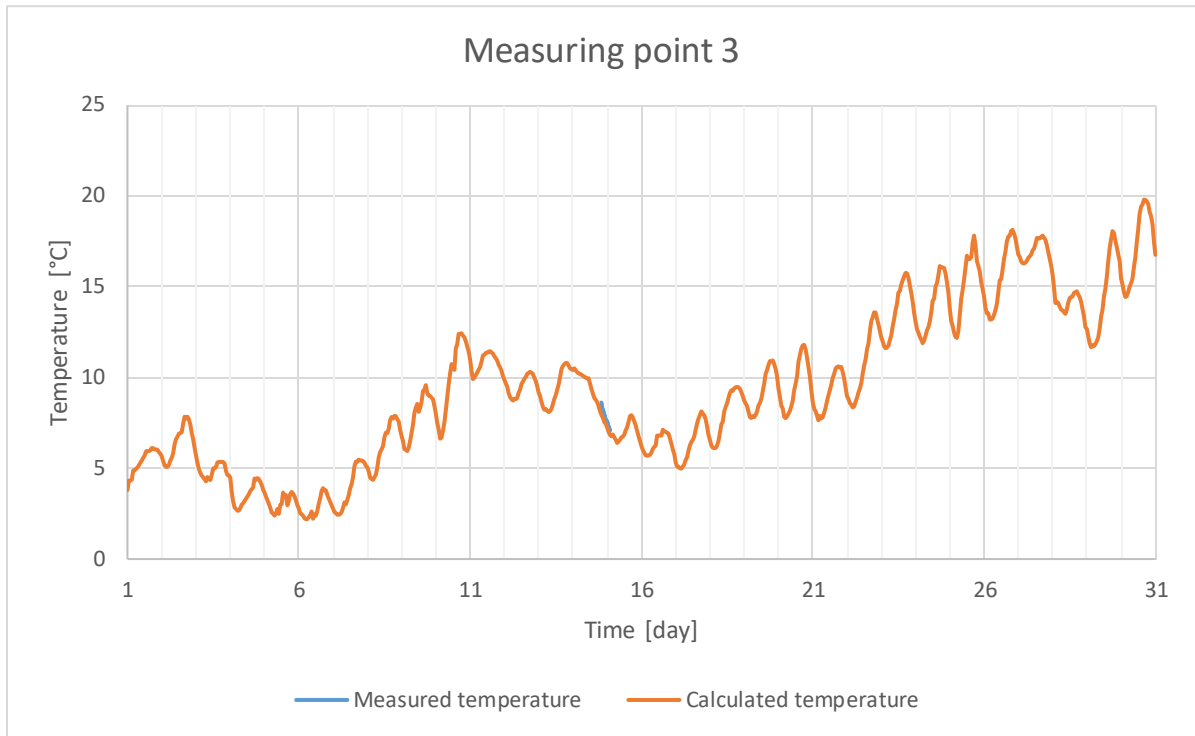


Figure 49. An overview of the temperature variation for measuring point 3 during the month of June. The observed data appears during June, 14th and June 15th.

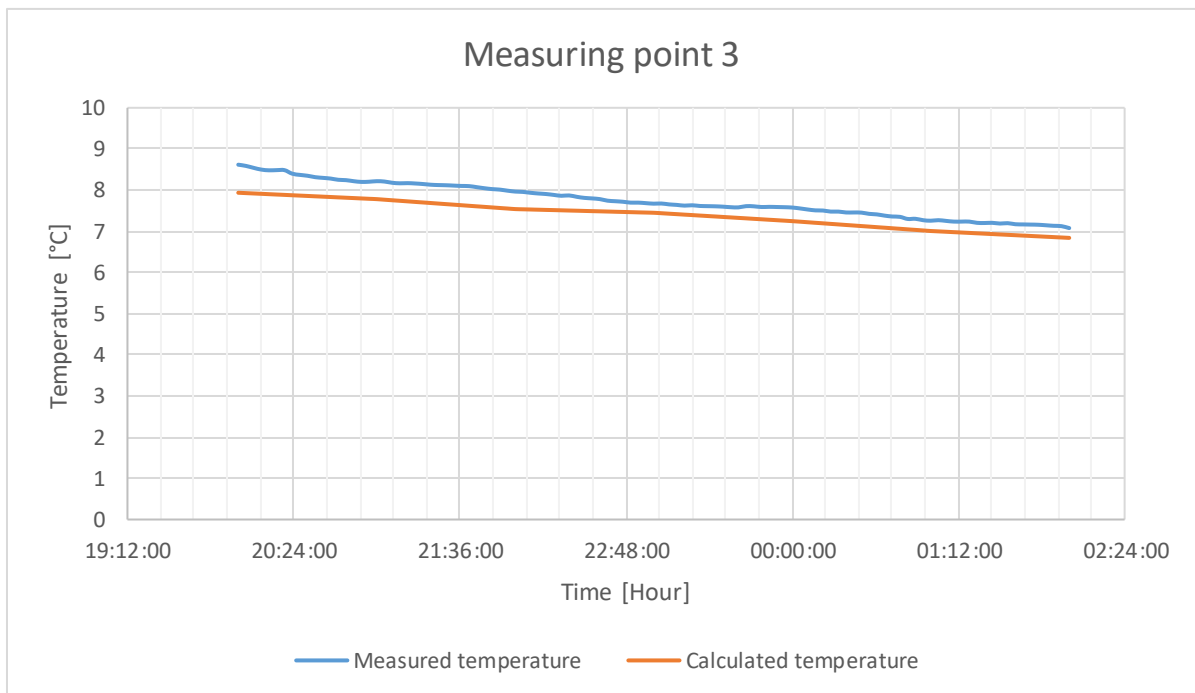


Figure 50. A comparison of the observed temperature and the calculated temperature for measuring point 3. There are only six values to be compared as seen.

Measuring point 4 can be found at the underside surface of the bridge cross section, between the southern girder and the mid girder.

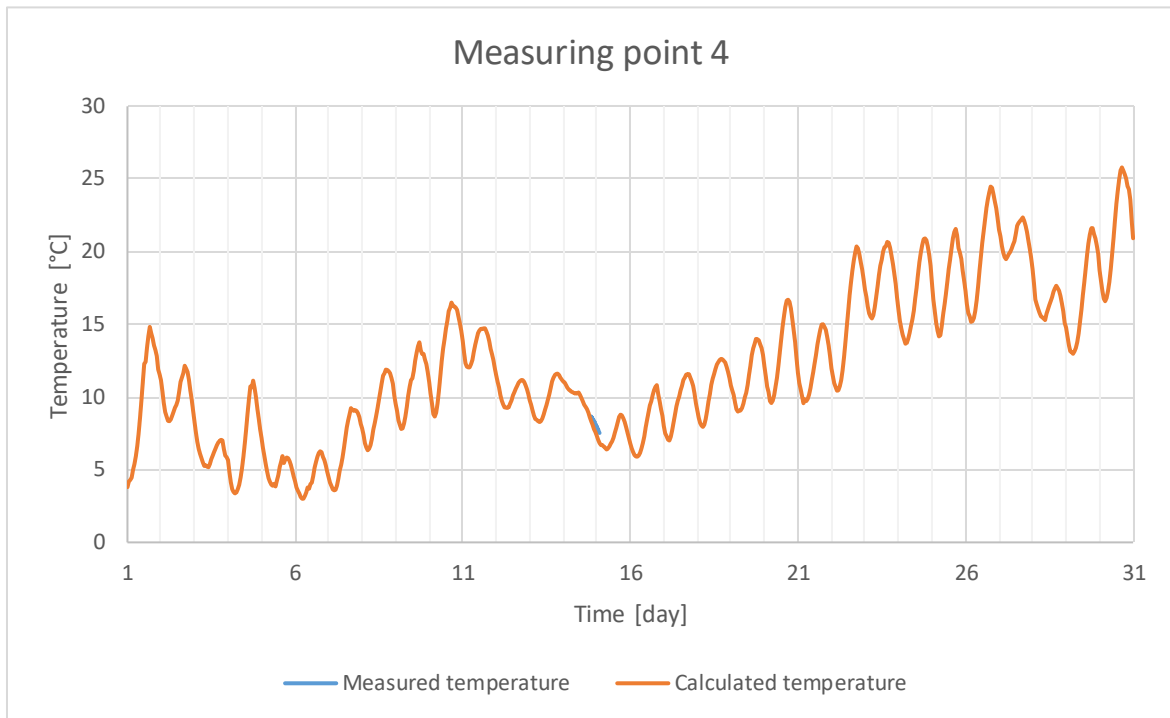


Figure 51. An overview of the temperature variation for measuring point 4 during the month of June. The observed data appears during June, 14th and June 15th.

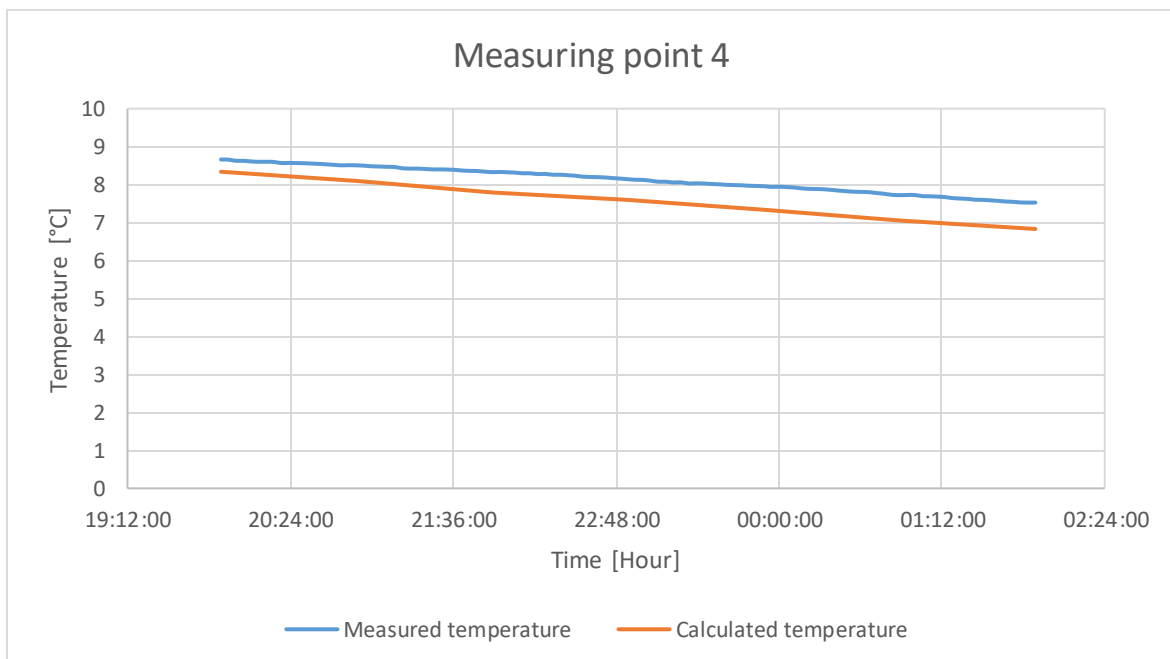


Figure 52. A comparison of the observed temperature and the calculated temperature for measuring point 4. There are only six values to be compared as seen.

Measuring point 5 can be found at the underside surface of the bridge between the south girder and the mid girder cross section.

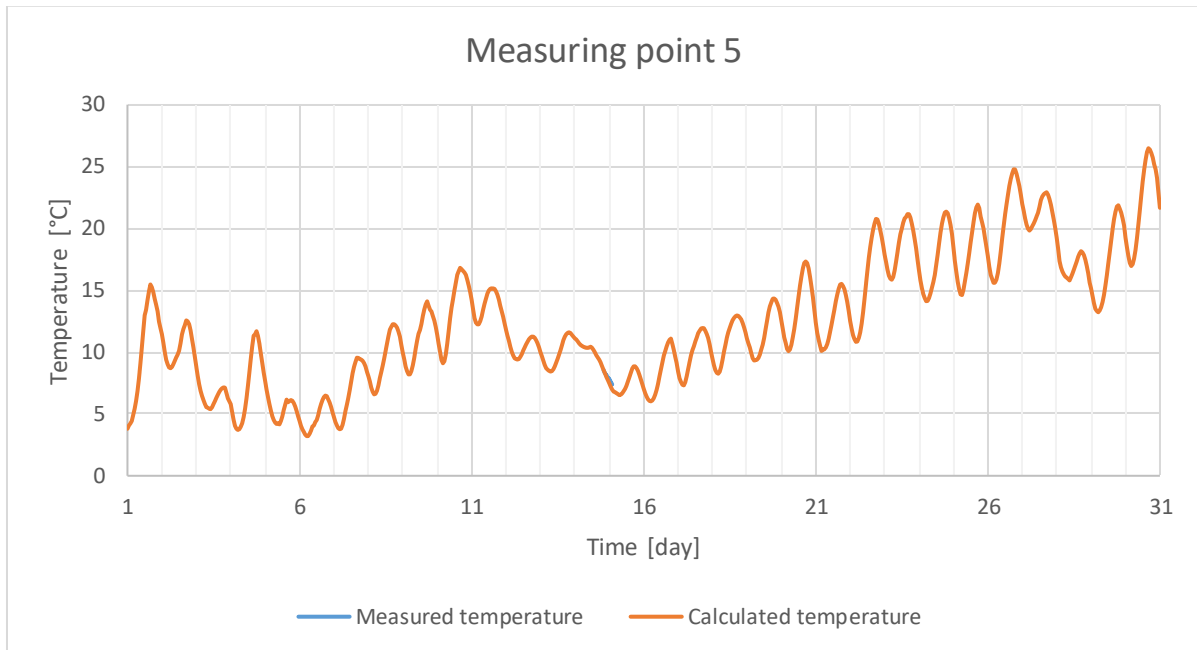


Figure 53. An overview of the temperature variation for measuring point 5 during the month of June. The observed data appears during June, 14th and June 15th.

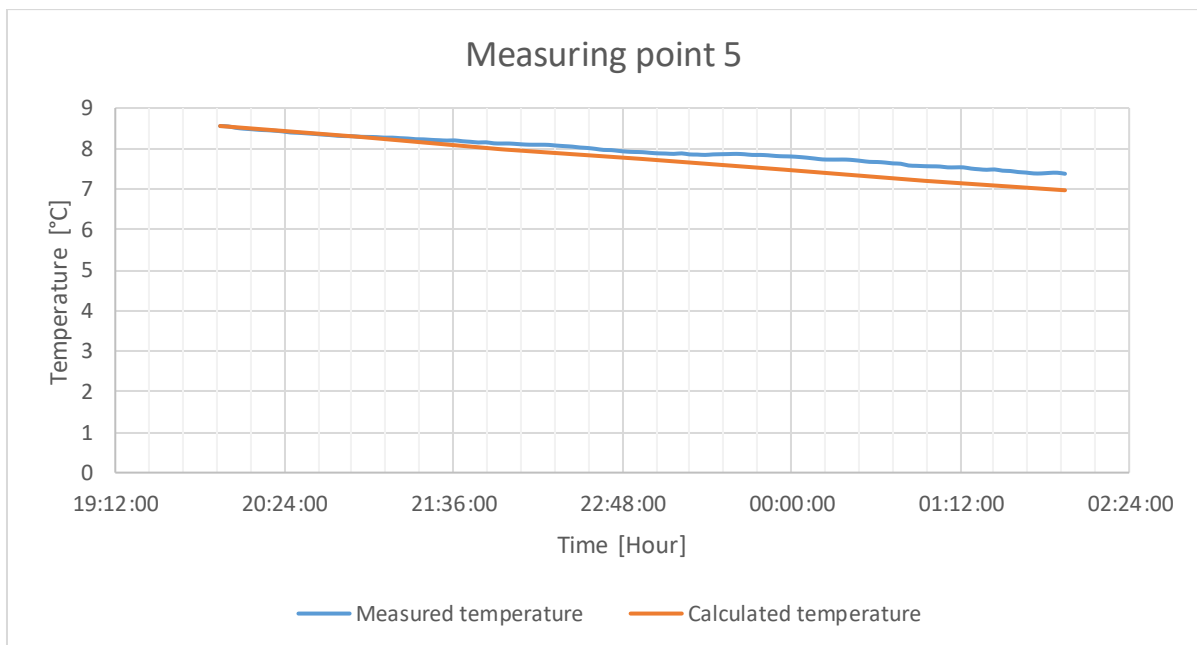


Figure 54. A comparison of the observed temperature and the calculated temperature for measuring point 5. There are only six values to be compared as seen.

Measuring point 6 can be found at the girder on the southern side of the bridge cross section.

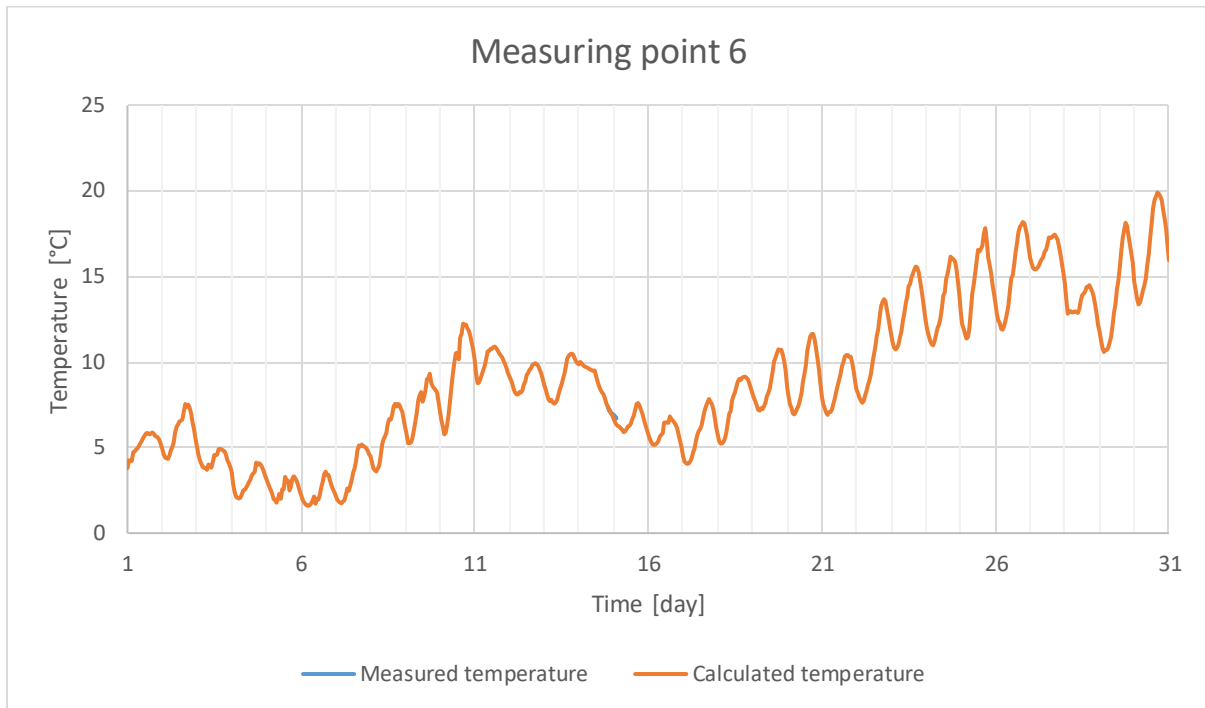


Figure 55. An overview of the temperature variation for measuring point 6 during the month of June. The observed data appears during June, 14th and June 15th.

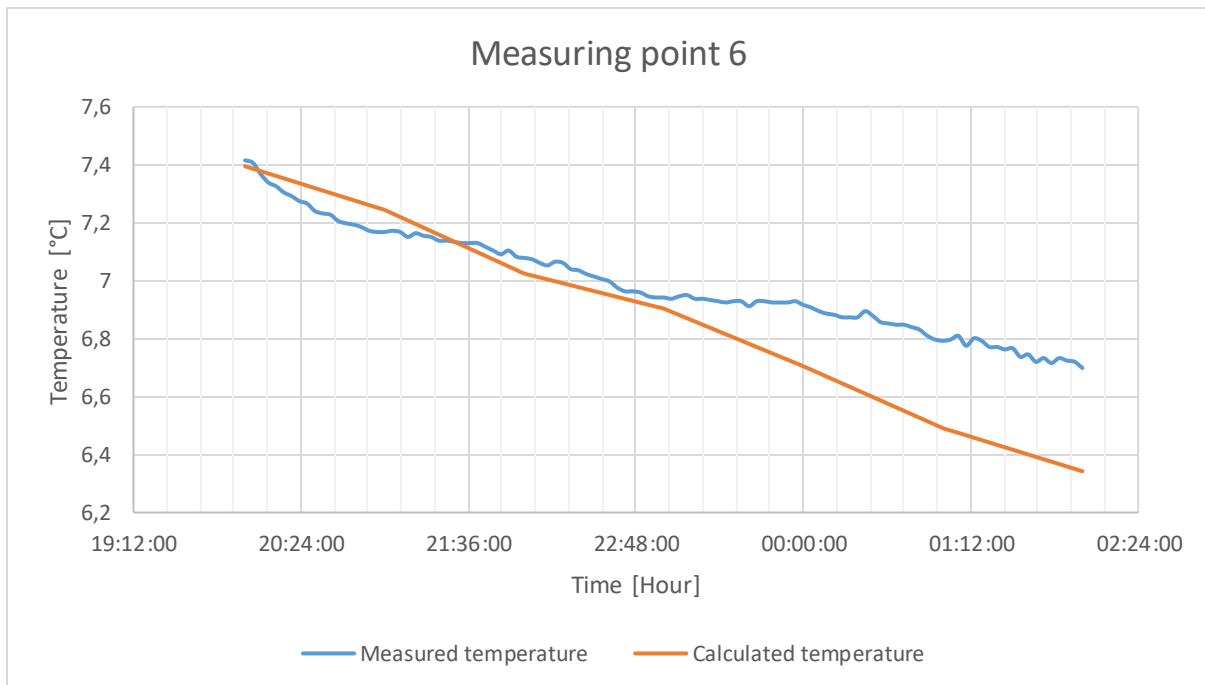


Figure 56. A comparison of the observed temperature and the calculated temperature for measuring point 6. There are only six values to be compared as seen.

Measuring point 7 can be found at the girder on the southern side of the bridge cross section.

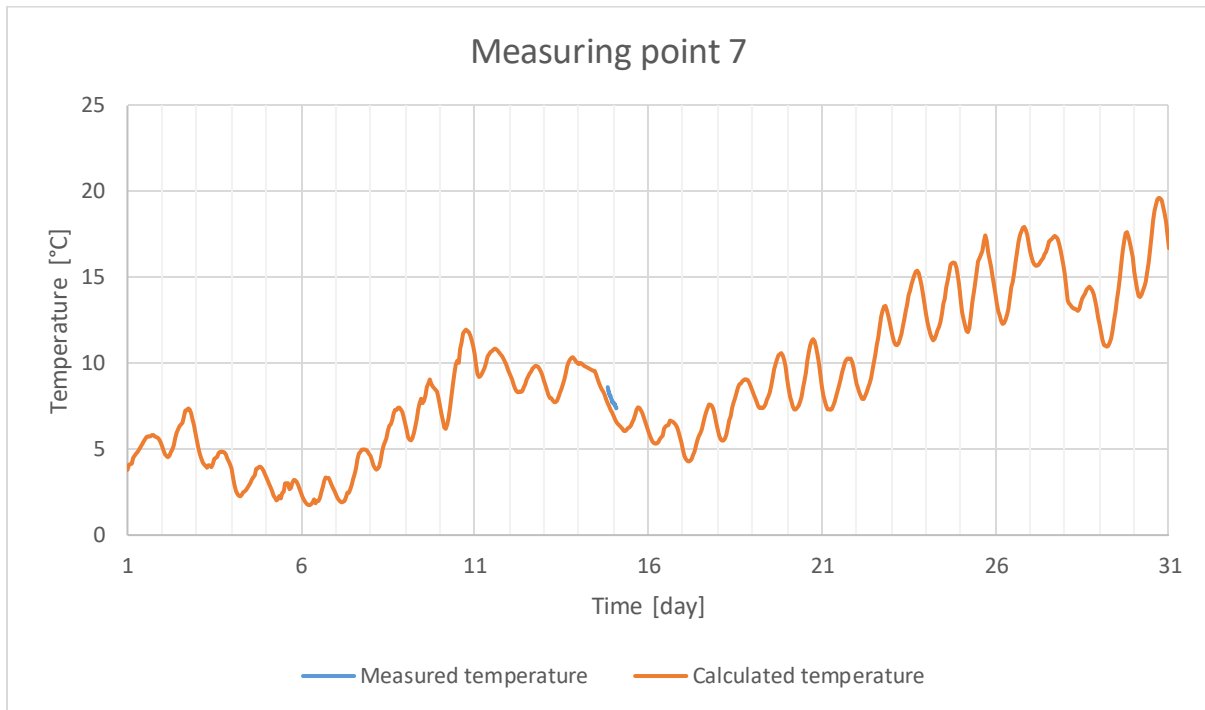


Figure 57. An overview of the temperature variation for measuring point 7 during the month of June. The observed data appears during June, 14th and June 15th.

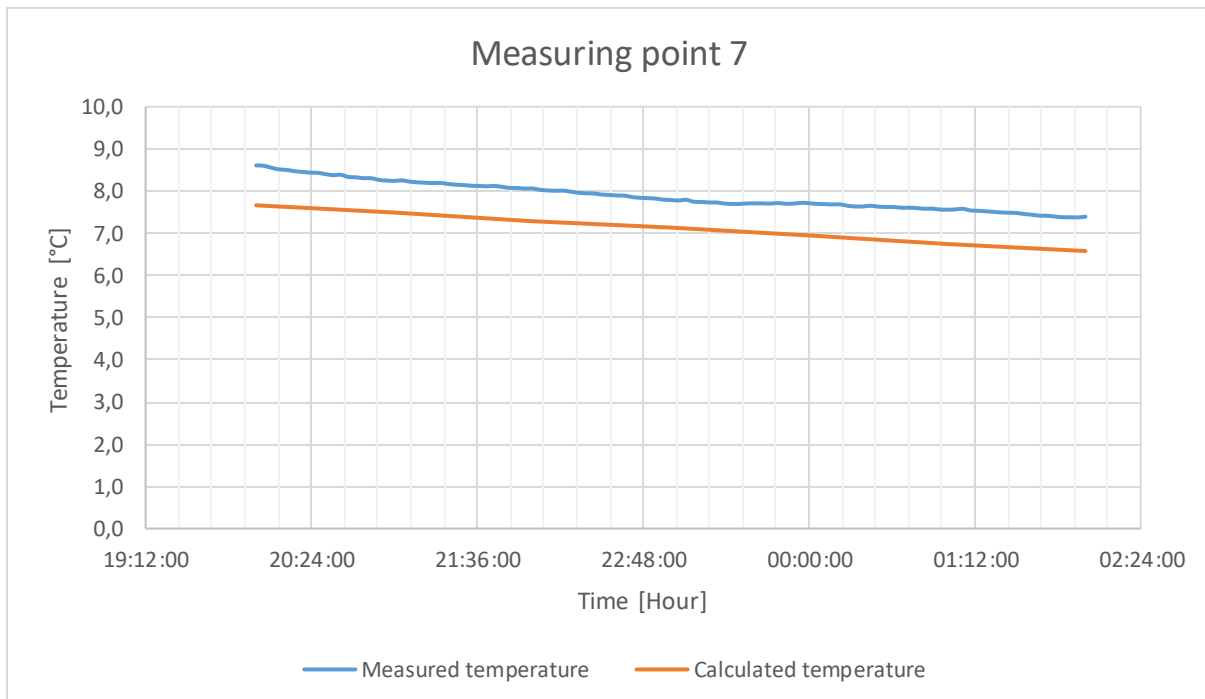


Figure 58. A comparison of the observed temperature and the calculated temperature for measuring point 7. There are only six values to be compared as seen.

10.2 Temperature variation in relation to depth

10.2.1 Temperature variation for June, 2009

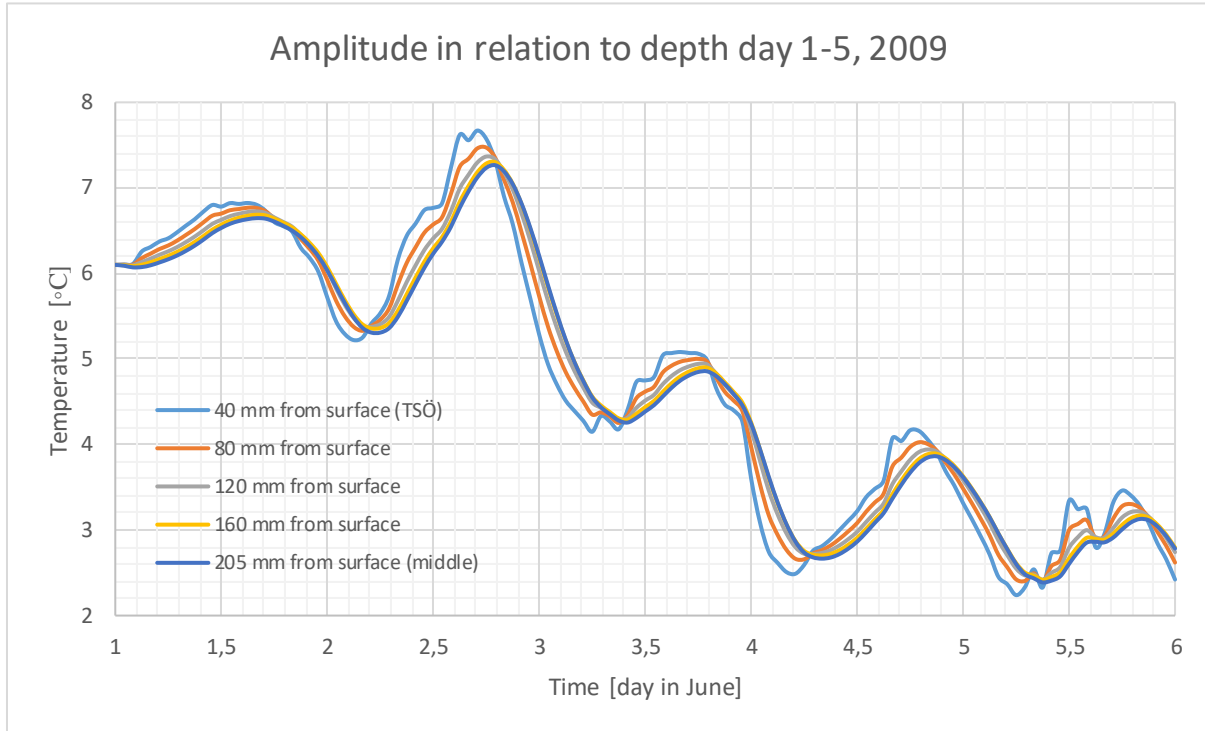


Figure 59. Temperature variation for the five different points calculated with the help of Abaqus. Time period is between the 1st of June to the 5th of June, 2009. The analysis is made on the southern girder, at the same height as the real measuring point TSÖ.

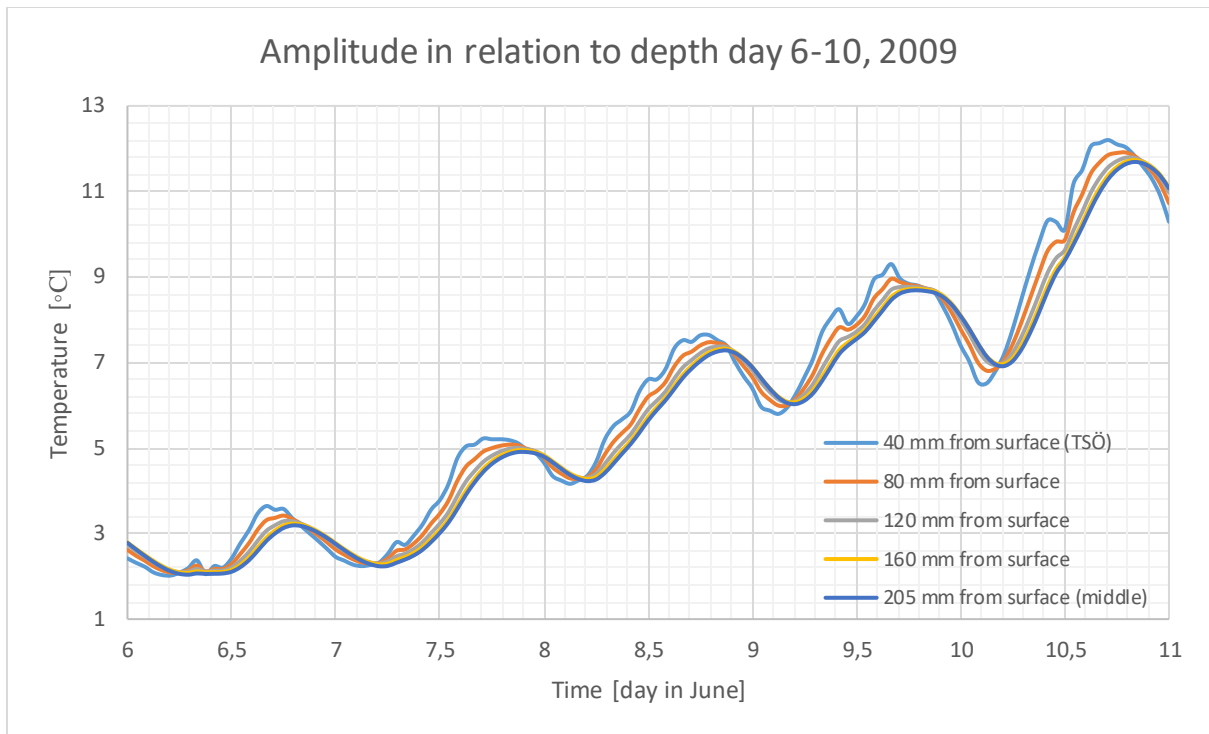


Figure 60. Temperature variation for the five different points calculated with the help of Abaqus. Time period is between the 6th of June to the 10th of June, 2009. The analysis is made on the southern girder, at the same height as the real measuring point TSÖ.

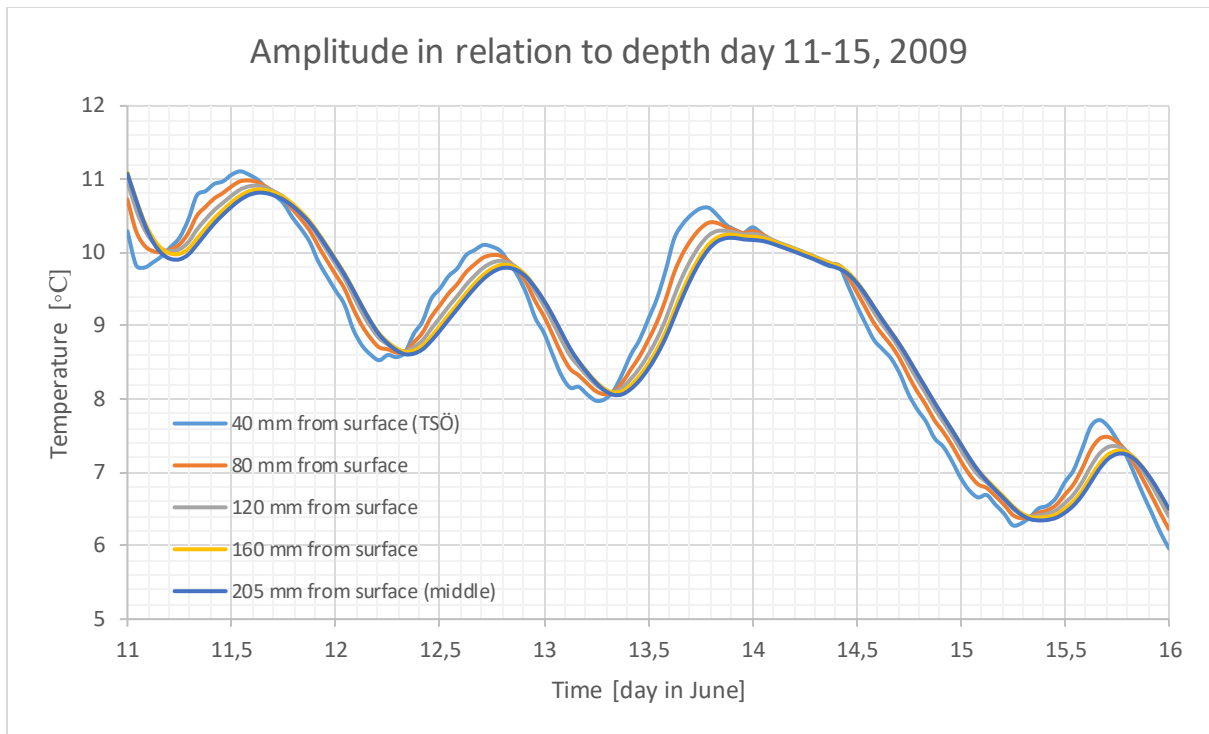


Figure 61. Temperature variation for the five different points calculated with the help of Abaqus. Time period is between the 11th of June to the 15th of June, 2009. The analysis is made on the southern girder, at the same height as the real measuring point TSÖ.

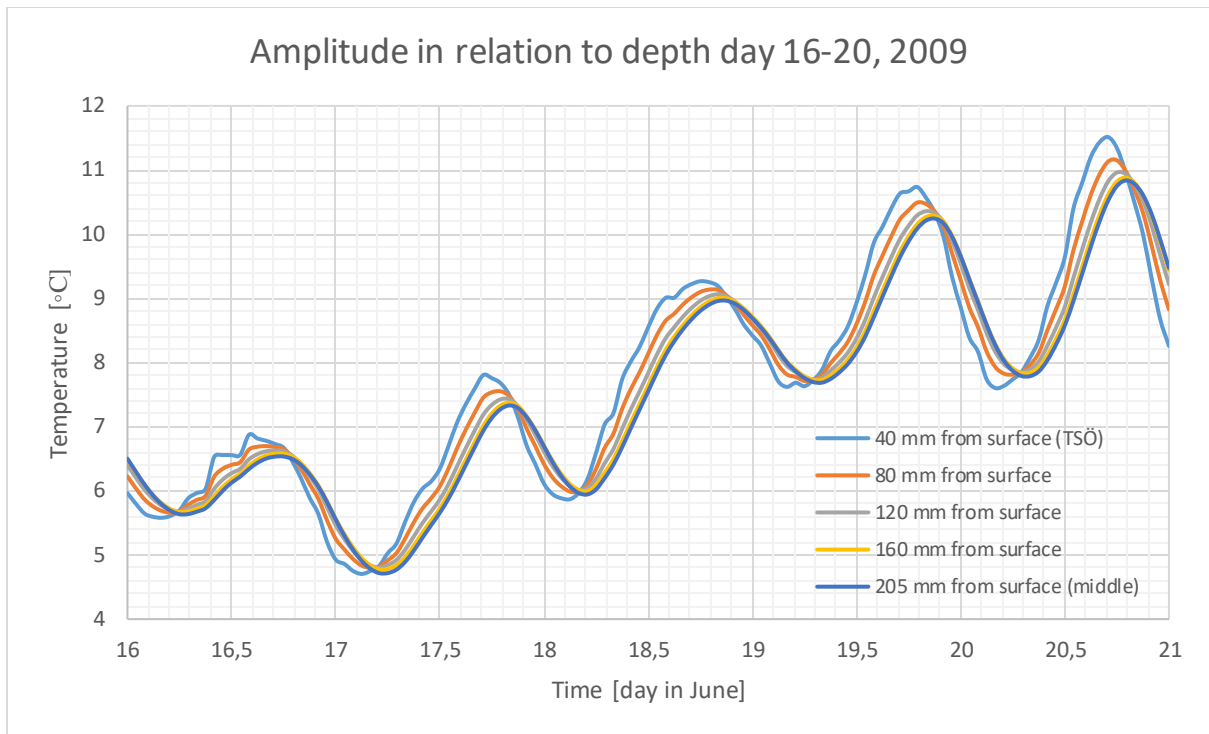


Figure 62. Temperature variation for the five different points calculated with the help of Abaqus. Time period is between the 16th of June to the 20th of June, 2009. The analysis is made on the southern girder, at the same height as the real measuring point TSÖ.

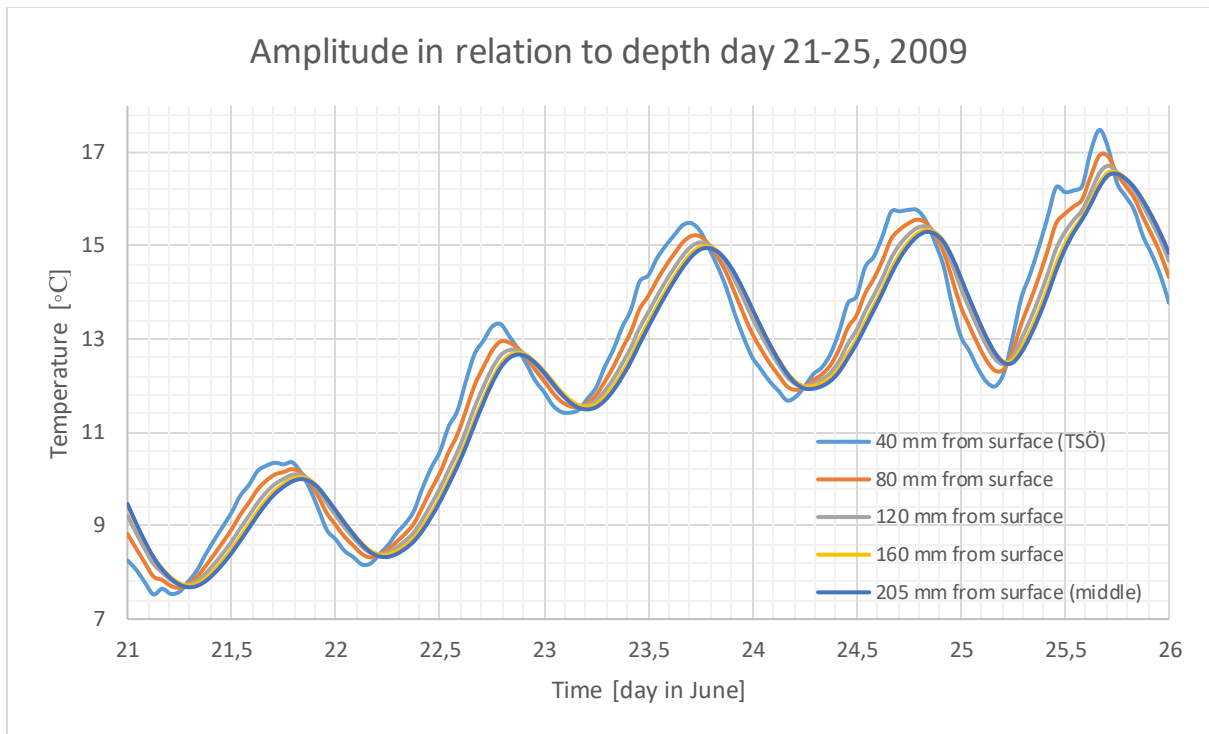


Figure 63. Temperature variation for the five different points calculated with the help of Abaqus. Time period is between the 21th of June to the 25th of June, 2009. The analysis is made on the southern girder, at the same height as the real measuring point TSÖ.

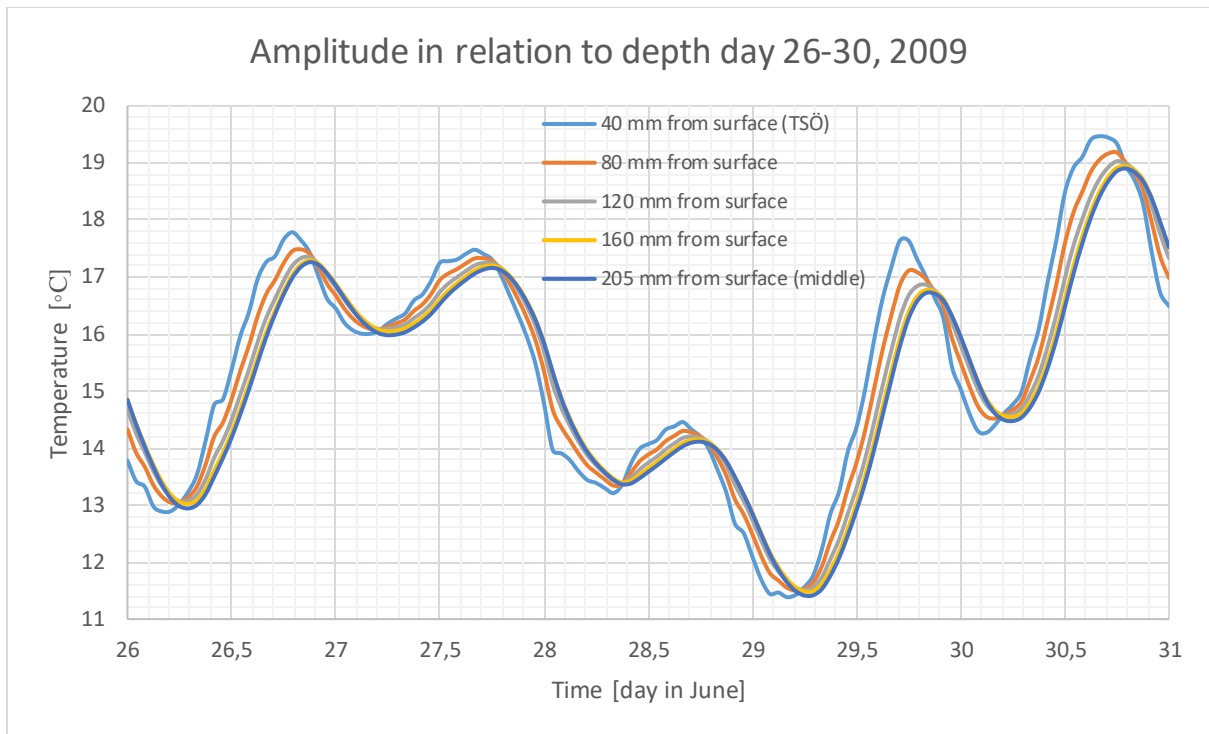


Figure 64. Temperature variation for the five different points calculated with the help of Abaqus. Time period is between the 26th of June to the 30th of June, 2009. The analysis is made on the southern girder, at the same height as the real measuring point TSÖ.

10.2.2 Temperature variation for August, 2010

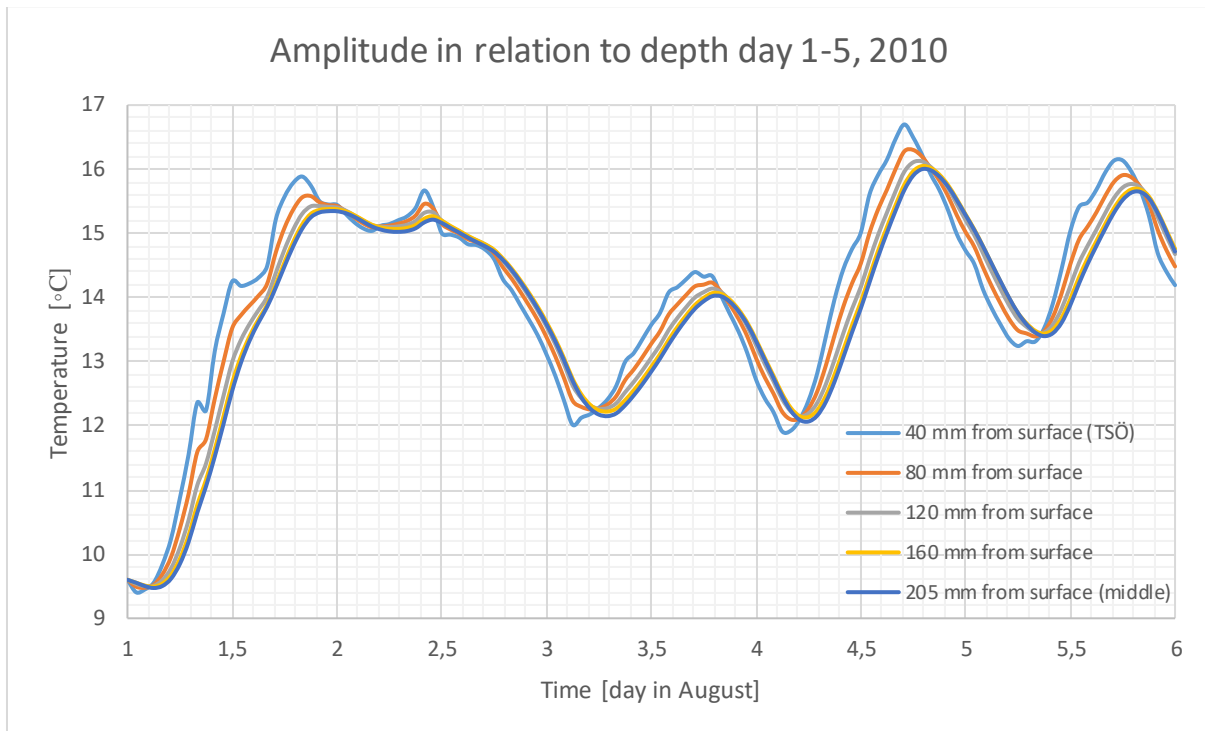


Figure 65. Temperature variation for the five different points calculated with the help of Abaqus. Time period is between the 1st of August to the 5th of August, 2010. The analysis is made on the southern girder, at the same height as the real measuring point TSÖ.

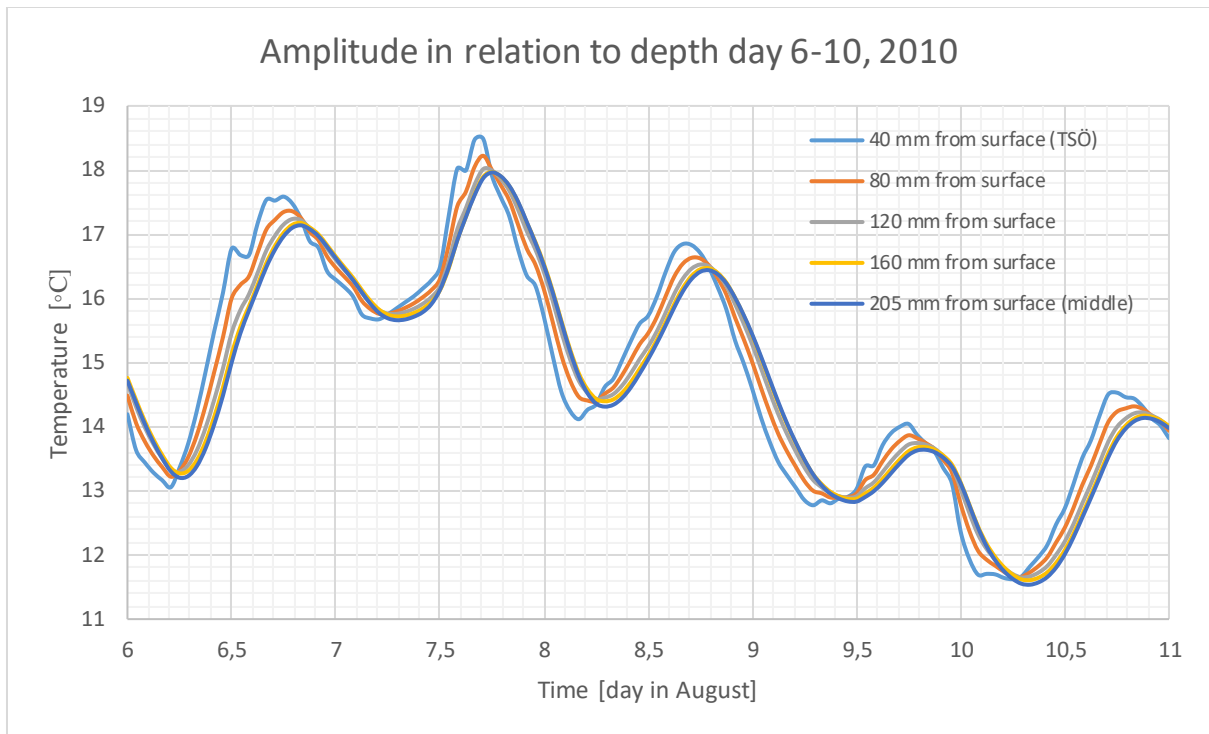


Figure 66. Temperature variation for the five different points calculated with the help of Abaqus. Time period is between the 6th of August to the 10th of August, 2010. The analysis is made on the southern girder, at the same height as the real measuring point TSÖ.

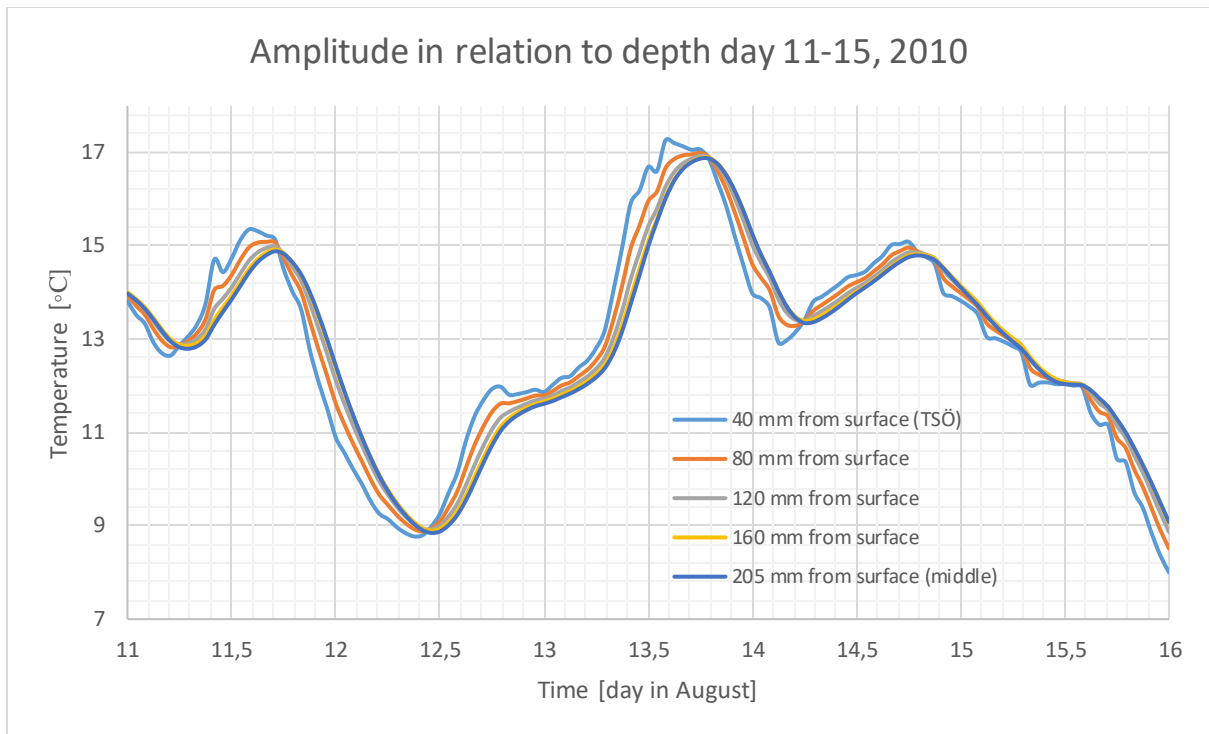


Figure 67. Temperature variation for the five different points calculated with the help of Abaqus. Time period is between the 11th of August to the 15th of August, 2010. The analysis is made on the southern girder, at the same height as the real measuring point TSÖ.

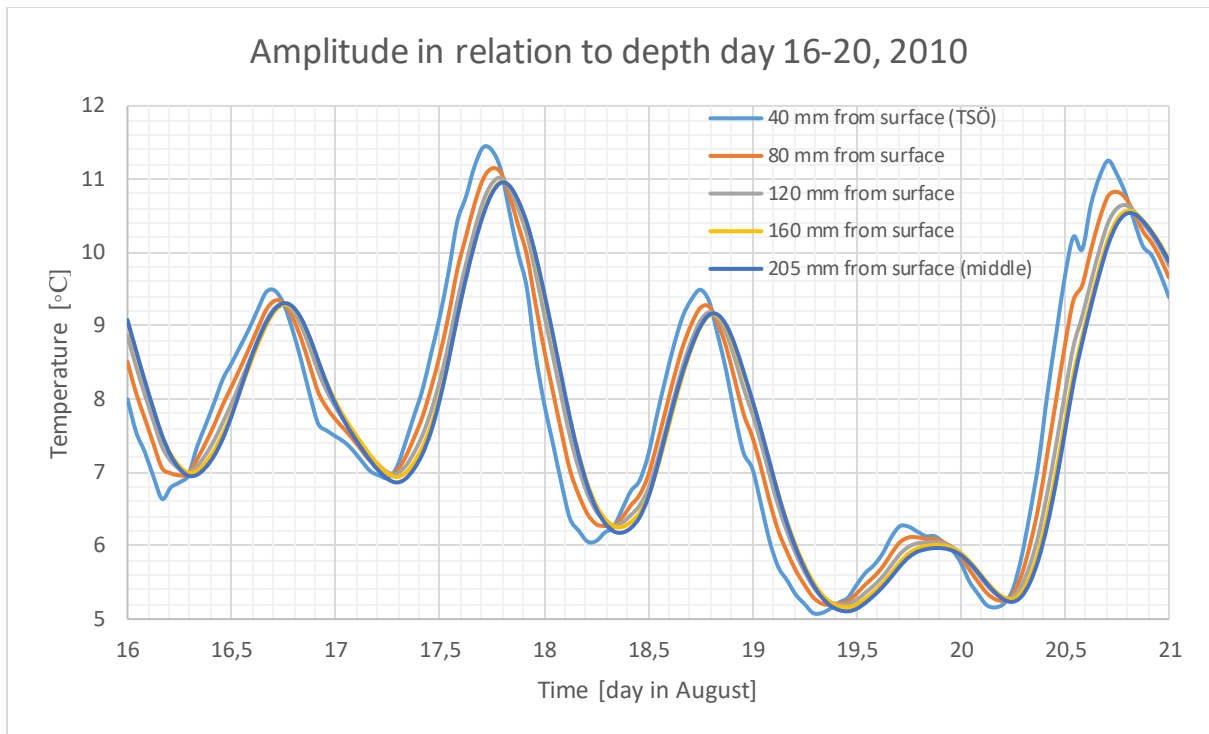


Figure 68. Temperature variation for the five different points calculated with the help of Abaqus. Time period is between the 16th of August to the 20th of August, 2010. The analysis is made on the southern girder, at the same height as the real measuring point TSÖ.

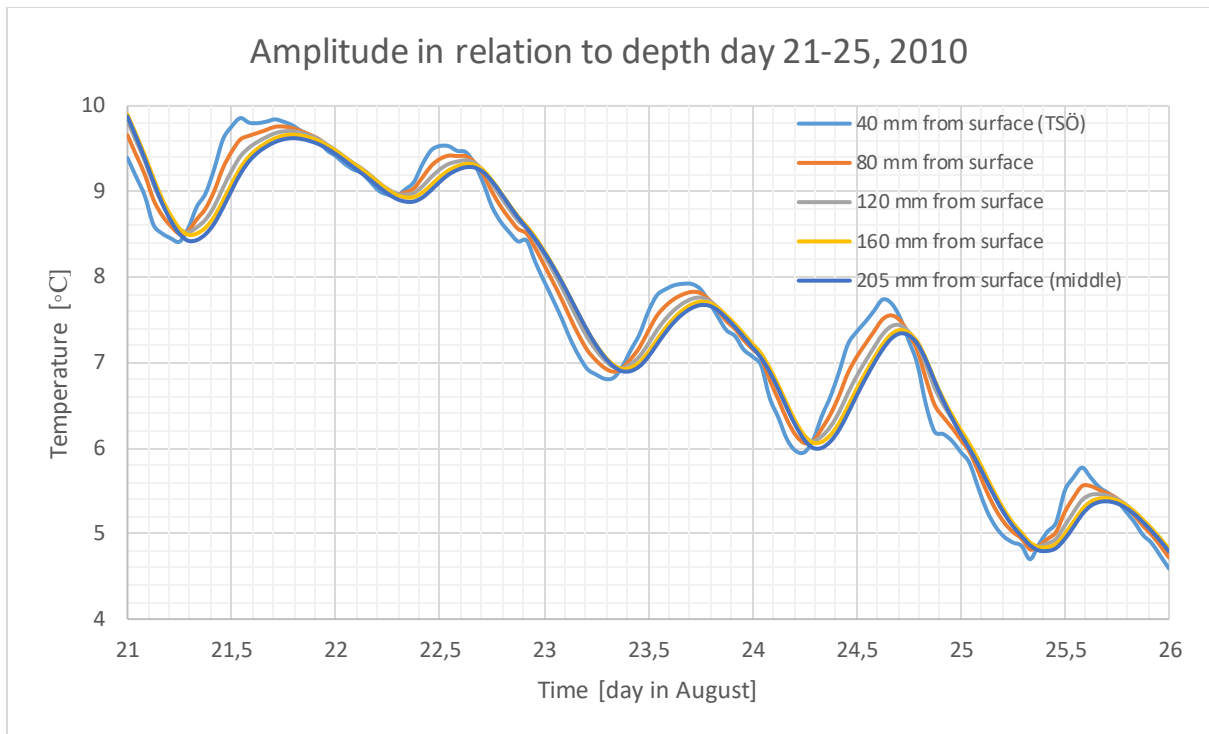


Figure 69. Temperature variation for the five different points calculated with the help of Abaqus. Time period is between the 21th of August to the 25th of August, 2010. The analysis is made on the southern girder, at the same height as the real measuring point TSÖ.

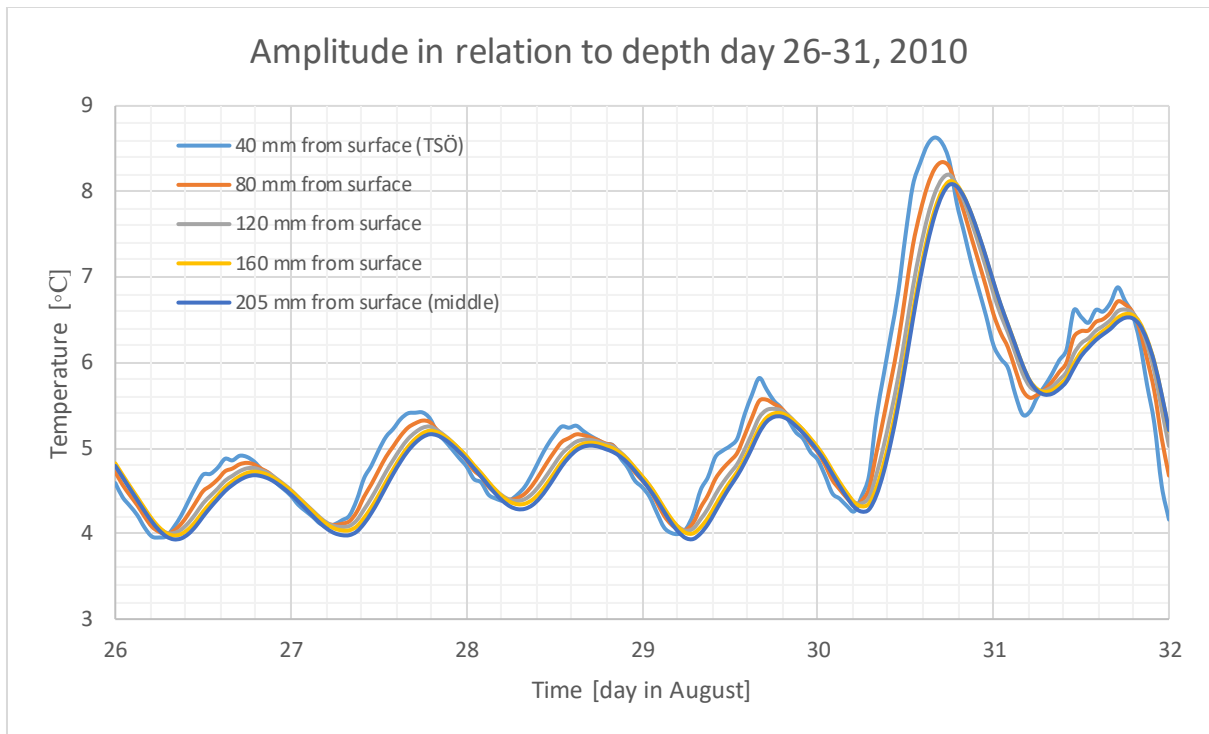


Figure 70. Temperature variation for the five different points calculated with the help of Abaqus. Time period is between the 26th of August to the 31th of August, 2010. The analysis is made on the southern girder, at the same height as the real measuring point TSÖ.

10.3 Temperature distribution in 2D model

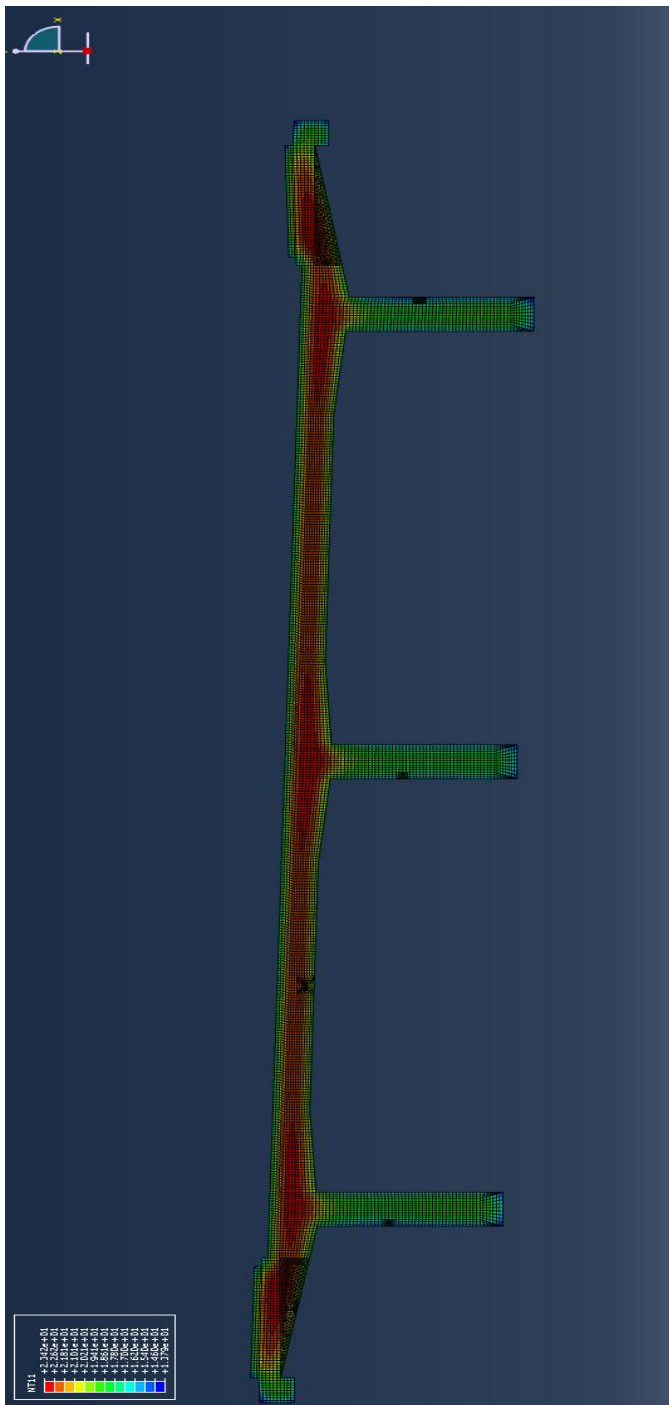
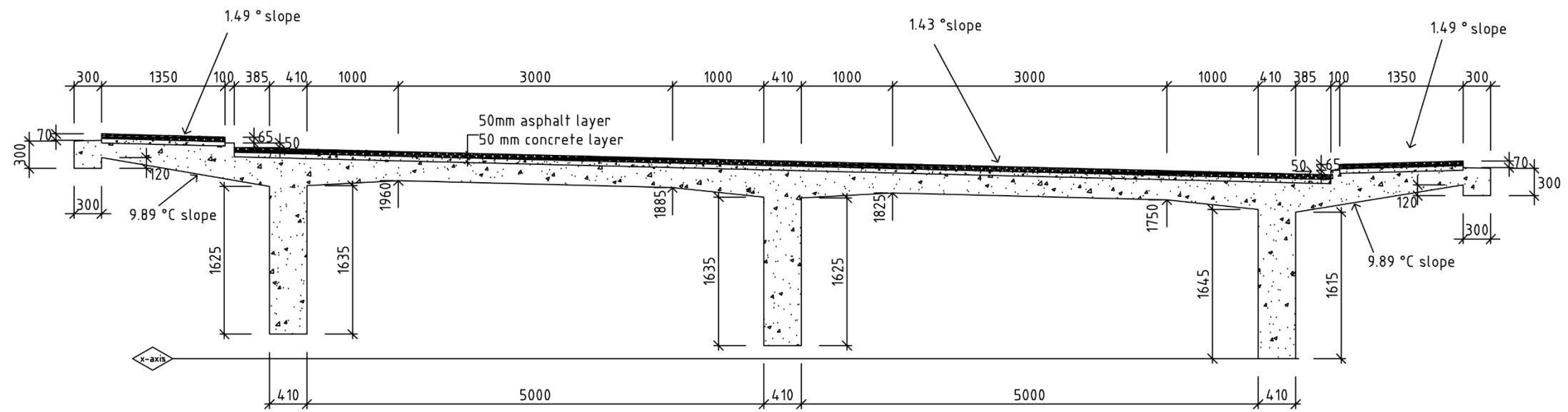


Figure 71. The figure illustrates a cross section of the bridge. The picture shows the temperature distribution at the end of June. The red color on top of the scale corresponds to the warmest parts of the bridge. The blue color on the bottom of the scale corresponds to the coldest parts of the bridge.



DIMENSIONS OF BRIDGE CROSS SECTION

REF.	ART.	BESKRIVNING AV FÖRÄNDRING	DATUM	AV
Cross section				
BH				
A				
K				
V				
E				
L				
UPPGIFTER	REDAKERAT AV	HANDLAGARE		
DATUM	ANSVARIG			
2016-05-03	HE			
SCALE	FORMAT	NET		
1:50	(A3)			

REF.1

LAGER: SB11

PLO: 2016-05-24 16:58 \\FS-N-NET.LTH.SEVHOME\FYS09HEK\KIRUNABRON EXAMENSARBETE\ALLA-ABAQUS-FILER\ABAQUS-FILER-SEKTIONER-MMA\WHOLE-BRIDGE-OMG_RECOVER.DWG